

**SINGLE PROTEIN DYNAMICS AT STEADY STATE
QUANTIFIED FROM FRET TIME TRACES**

Biochemical & Physical Manipulation of Hsp90

SONJA SCHMID



Technische Universität München

Physik Departement

Lehrstuhl für Biophysik, E22

**SINGLE PROTEIN DYNAMICS AT STEADY STATE
QUANTIFIED FROM FRET TIME TRACES**

Biochemical & Physical Manipulation of Hsp90

SONJA SCHMID

Vollständiger Abdruck der von der Fakultät für Physik der Technischen Universität München
zur Erlangung des akademischen Grades eines
Doktors der Naturwissenschaften (Dr. rer. nat.)
genehmigten Dissertation.

Vorsitzender: Univ.-Prof. Dr. Martin Zacharias

Prüfer der Dissertation: 1. Univ.-Prof. Dr. Thorsten Hugel

2. Univ.-Prof. Dr. Matthias Rief

Die Dissertation wurde am 21.12.2016 bei der Technischen Universität München eingereicht
und durch die Fakultät für Physik am 20.01.2017 angenommen.

ABSTRACT

Within this thesis, the progression of the heat-shock protein Hsp90 through distinct conformational states was recorded by single molecule Förster resonance energy transfer (FRET) and investigated under multiple controlled conditions.

Eukaryotic Hsp90 is an essential, homo-dimeric chaperone protein with ATPase activity that undergoes large conformational opening and closing transitions. In stark contrast to the dynamics of many motor proteins, Hsp90's global dynamics occur similarly in the presence and absence of ATP, i.e. even in thermal equilibrium. Hence, it was a common hypothesis that helper proteins (cochaperones) would link a conformational transition to energy consumption and thus induce directional kinetics.

Single molecule time traces are predestined to solve such thermodynamic questions because they reveal the time evolution of unsynchronized kinetic systems at steady-state (explicitly including the non-equilibrium steady-state). To exploit this unique feature, a single molecule analysis for complex kinetic sequences (SMACKS) was developed, and specifically fine-tuned to get a quantitative and testable description of Hsp90's conformational dynamics. Based on a set of time traces, SMACKS infers one kinetic state model including all relevant transition rates and also their uncertainties. Thereby, it eliminates previous artifacts, in particular the dwell-time related, systematic and non-linear overestimation of transition rates. Notably, this versatile maximum-likelihood approach is applicable to all kinds of single molecule time traces.

Applied to Hsp90, SMACKS resolved the expected kinetic heterogeneity. Specifically, two distinct open and two distinct closed states could now be distinguished explicitly. On top of that, it allowed Hsp90 to be tested for ATP hydrolysis driven, directional kinetics. Yet, even under severalfold stimulation of Hsp90's ATPase activity by the cochaperone Aha1, no directional kinetics were found.

In addition, this work presents many more examples of the dynamic structure-function relationship in Hsp90, among them the effect of anti-cancer drug candidates, a point mutation in Hsp90's hinge region, the differential effects of viscosity and macromolecular crowding, as well as the influence of monovalent salts.

Altogether, the results draw a picture of a very flexible Hsp90. Although this conformational flexibility is largely independent of the ATPase activity, the *inverse* is not true. In fact, both specific and non-specific manipulation of Hsp90's conformational energy landscape were found to modulate its ATPase activity. Remarkably, non-specific conformational confinement induced a nearly 5-fold *increase* in ATPase activity. This highlights a new aspect of Hsp90's controversially discussed ATPase function, namely its sensitivity to conformational flexibility.

ZUSAMMENFASSUNG

In dieser Doktorarbeit wurde mittels Einzel-Molekül-Förster-Resonanz-Energie-Transfer (FRET) das Fortschreiten des Hitzeschockproteins Hsp90 durch einzelne Konformationszustände verfolgt und unter verschiedenen kontrollierten Bedingungen untersucht.

Eukaryotisches Hsp90 ist ein essentielles homo-dimerisches Chaperon-Protein. Es besitzt ATPase-Aktivität und macht grosse Zustandsänderungen zwischen N-terminal offenen und geschlossenen Konformationen. Im dezidierten Gegensatz zu den Dynamiken vieler Motorproteine, passieren diese allerdings in Anwesenheit wie auch Abwesenheit von ATP, d.h. sogar im thermischen Gleichgewicht. Eine gängige Hypothese lautete, dass erst im Zusammenspiel mit Helferproteinen (Cochaperonen) Konformationsänderungen an die ATP-Hydrolyse koppeln und daher gerichtete Dynamik induziert würde.

Einzel-Molekül-Zeitreihen sind prädestiniert für solche thermodynamischen Fragestellungen, da sie den (unsynchronisierten) Zeitverlauf kinetischer Systeme im Fließgleichgewicht detektieren können. Um dieses Alleinstellungsmerkmal ausnützen zu können, wurde eine Analyse für komplexe kinetische Abläufe entwickelt (SMACKS). Sie wurde so optimiert, dass eine quantitative und überprüfbare Beschreibung der Konformationsdynamik von Hsp90 möglich wurde. SMACKS bestimmt auf Basis eines Zeitreihen-Sets ein kinetisches Zustandsmodell mit allen relevanten Übergangsraten und deren Unsicherheiten. Damit konnten frühere Artefakte ausgeräumt werden, insbesondere die systematische, nicht-lineare Überschätzung von Verweildauerbasierten Übergangsraten. Dieser Maximum-Likelihood-Ansatz ist im Übrigen auf vielerlei Einzelmolekül Zeitreihen anwendbar.

Bezüglich Hsp90 hat SMACKS die erwartete kinetische Heterogenität aufgelöst. Konkret konnten nun zwei unterschiedliche offene und zwei unterschiedliche geschlossene Zustände explizit unterschieden werden. Darüber hinaus konnte mit SMACKS die Konformationsdynamik auf ATP-Hydrolyse getriebene, gerichtete Prozesse geprüft werden, d.h. Prozesse im Nicht-Gleichgewicht. Allerdings wurde sogar unter vielfacher ATPase-Stimulation durch das Cochaperon Aha1 keine gerichtete Kinetik beobachtet.

Zusätzlich präsentiert diese Arbeit viele weitere Beispiele der dynamischen Struktur-Funktions-Beziehung in Hsp90, darunter der Effekt von Anti-Krebs Wirkstoff-Kandidaten, eine Punktmutation in der Gelenkregion von Hsp90, die unterschiedlichen Effekte von Viskosität und makromolekularem Crowding, sowie der Einfluss einwertiger Salze.

Zusammenfassend zeigen die Resultate ein sehr dynamisches und flexibles Hsp90. Obwohl diese Flexibilität weitestgehend unabhängig von der ATPase-Aktivität ist, gilt der Umkehrschluss nicht. Tatsächlich wurde die ATPase-Aktivität sowohl durch spezifische, wie auch unspezifische Manipulation der Konformations-abhängigen Energielandschaft von Hsp90 beeinflusst. Bemerkenswert ist hier, dass gänzlich unspezifisches Einschränken des Konformationsraums zu einer fast 5-fach erhöhten ATPase-Aktivität führte. Dieser Aspekt könnte wesentlich zum Verständnis der kontrovers diskutierten ATPase-Funktion beitragen.

PUBLICATIONS

Some ideas have appeared in:

- [A] Schmid S, & Hugel T. Regulatory Posttranslational Modifications in Hsp90 Can Be Compensated by Cochaperone Aha1. *Molecular Cell* 41, 6 (2011), 619–620. [Link](#).
- [B] Schmid S, Götz M, & Hugel T. Single-Molecule Analysis beyond Dwell Times: Demonstration and Assessment in and out of Equilibrium. *Biophysical Journal* 111, 7 (2016), 1375–1384. [Link](#).
- [C] Götz M, Wortmann P, Schmid S, & Hugel T. Chapter Sixteen - A Multicolor Single-Molecule FRET Approach to Study Protein Dynamics and Interactions Simultaneously. *Methods in Enzymology*. Ed. by Spies M, & Chemla YR. Vol. 581. Academic Press, 2016, 487–516. [Link](#).
- [D] Hellenkamp B, Schmid S, et al. *FRET as a Molecular Ruler – a Comparative Study*. (under preparation).

ACKNOWLEDGMENTS

As an economic refugee from Switzerland, I would like to start by thanking the German tax payer who earned most of the cash I splashed during my doctorate.

For the opportunity to do so, I am grateful to my advisor Thorsten Hugel who introduced me to the academic world and gave me the freedom to acquire knowledge in very diverse fields. This was of course in close connection with my colleagues. In particular, I learned a lot during numberless discussions with Björn and Markus. I thank you for this ping-pong of ideas, which was both, very inspiring and fun. My thanks go also to Christina (from her I inherited the setup), Markus J., Philipp and the entire Hugel group, as well as the students who contributed to this work: Matthias, Franziska & Sabine.

At TUM's biophysics section E22/E27 I could experience a very open, creative, inter-disciplinary and thus scientifically fruitful atmosphere, which relied greatly on the good understanding between the chairs of Matthias Rief (my second advisor) and Andreas Bausch, along with the Dietz, Oekten & Woehlke groups.

It was an honor to share the mighty Green Office with Gabriel and Fabi, to have Jo & Lorenz, alias J-Lo, next door, and to hear Uli and Alex both, laughing & swearing opposite the aisle. Also personally, you guys have been very important to me, and I am grateful for the time we shared in Munich. In addition, my thanks go to many more people with whom I shared not only the lab, but also numerous memorable moments, including Carina, Felix, Thomas, Anja, Ziad, Dani, Soumit, Uli the U, Heinrich, Beni, Joana, Schuppi, Leo, Marco, and the Dietz crew. The various X-mas parties, OF-seminaries, Starkbier-Fests or just spontaneous gatherings with all of you were legendary.

Also I would like to thank the lab assistants Gabi, Karin, Dani, Moni, as well as Rudi from the workshop. Your work can not be overrated. I know what I am talking about. . .

Also Elke & Nicole were never tired of explaining surreal administrative routines. E.g.: I will never forget how I swore (not so solemnly) to be faithful to the Bavarian (not German!) constitution.

With the help of this large biophysics family, I survived Garchosibirsk and managed to "take the next step" to Freiburg, together with Markus, Philipp, Asia, Sofia, Johann, and later Björn, Bizan, Jola and Lesley, the walking dictionary. Particularly, I would like to thank them for accepting my eremitic attitude at the time.

Last but not at least, I owe my family a debt of gratitude for supporting me in so many decisions throughout my life. Gertrud & Bernd, Ju & Kamal & Younès, Caro & Nello and the M&M's, you all were very patient with me. I also thank Thomas Post for standing by me during the toughest years of my doctorate.

CONTENTS

	I INTRODUCTION & THEORY
3	1 INTRODUCTION
5	2 HEAT-SHOCK PROTEIN HSP90
5	2.1 Structure & Functional Elements
6	2.2 Chaperone Function & Regulation
9	3 FLUORESCENCE & FRET
9	3.1 Jablonski Diagram
11	3.2 Properties of Fluorescence
12	3.3 Förster Resonance Energy Transfer
15	4 DETECTION OF SINGLE FLUOROPHORES
15	4.1 Experimental Strategies
16	4.2 The Physics of Total Internal Reflection
19	4.3 The TIR Fluorescence Microscope
21	5 SINGLE MOLECULE PATTERN RECOGNITION
21	5.1 The Parametrization of Hidden Markov Models
22	5.2 The Canonical Algorithms
	II EXPERIMENT
27	6 SINGLE MOLECULE FRET TIME TRACES
27	6.1 Design of the TIRF Microscope
29	6.2 Single Molecule TIRF Measurements
30	6.3 Low Auto-Fluorescence Flow Chambers
31	6.4 smFRET Data Preparation
35	7 AN IDEAL PROTEIN CONSTRUCT FOR SMTIRF
35	7.1 Site-Specific Fluorescent Labeling
36	7.2 Immobilization
37	7.3 High Affinity Complexes
	III RESULTS & DISCUSSION
41	8 EXPERIMENTAL POTENTIALS AND LIMITS
41	8.1 The Fundamental Triangle
43	8.2 The Distance Resolution of smFRET
52	8.3 Kinetic Accuracy
57	8.4 Summary 1
59	9 QUANTITATIVE SINGLE MOLECULE KINETICS
59	9.1 Inferring One Global Kinetic Model
65	9.2 Dealing with Kinetic Heterogeneity
68	9.3 Evaluation
70	9.4 Thermodynamics
73	9.5 Summary 2

CONTENTS

75	10 HSP90'S CONFORMATIONAL KINETICS
75	10.1 Nucleotide Dependence of Hsp90's Conformations
76	10.2 Nucleotide-Dependent Conformational Kinetics
79	10.3 Thermodynamic Consequences
80	10.4 Discussion
83	10.5 Summary 3
85	11 BIOCHEMICAL MANIPULATION OF HSP90
85	11.1 ATPase Stimulation by Cochaperone Aha1
87	11.2 The Effect of Drug Candidates
90	11.3 Interfering with Hsp90's Hinge
93	11.4 Summary 4
95	12 PHYSICAL MANIPULATION OF HSP90
95	12.1 Macromolecular Crowding & Viscosity
101	12.2 Dependence on Monovalent Cations
104	12.3 Summary 5
105	13 OUTLOOK: VARIOUS TIMESCALES
107	14 CONCLUSION
	APPENDIX
111	A SUPPORTING INFORMATION
121	B MATERIALS & METHODS
127	C α -SYNUCLEIN
131	D SMACKS MANUAL
137	BIBLIOGRAPHY

ACRONYMS

ADC	analog-to-digital converter
ADP	adenosine diphosphate
ALEX	alternating laser excitation
AMP-PNP	5'-adenylyl- β - γ -imidodiphosphate
APD	avalanche photodiode
ATP	adenosine triphosphate
BIC	Bayesian information criterion
bp	base pair
dsDNA	double-stranded DNA
EMCCD	electron multiplying charge-coupled device
FPS	FRET-restrained positioning and screening
FRET	Förster resonance energy transfer
GFP	green fluorescent protein
GHKL	GyrB, Hsp90, histidine kinase, MutL
HMM	hidden Markov model
HOMO	highest occupied molecular orbital
$h\nu$	Planck constant times frequency, i.e. photon energy
kT	Boltzmann constant times temperature, i.e. thermal energy
LUMO	lowest unoccupied molecular orbital
MD	molecular dynamics simulation
NHS	N-Hydroxysuccinimide
PDA	probability density analysis
PDF	probability density function
PEG	polyethylene glycol
RMSD	root-mean-square deviation
s-CMOS	scientific complementary metal-oxide-semiconductor
SMACKS	single molecule analysis for complex kinetic sequences
smFET	single molecule field effect transistor
smFluo	single molecule fluorescence
smFRET	single molecule FRET
SNR	signal-to-noise ratio
SUMO	small ubiquitin-related modifier
TCEP	Tris-(2-carboxyethyl)-phosphin
TIR	total internal reflection
TIRF	total internal reflection fluorescence
TIF	tagged image file
TPR	tetratricopeptide repeat
TRIS	tris(hydroxymethyl)aminomethane

Part I

INTRODUCTION & THEORY

INTRODUCTION

Proteins are the most fascinating polymers on earth! Although they consist of dead material, they keep us alive by maintaining a steady state away from thermodynamic equilibrium. For that purpose, many proteins consume external (i.e. non thermal) energy, which in the cell is frequently provided by nucleosid tri-phosphates, e.g. ATP. This energy powers their functional cycle, that is to say, the directed progression through states with distinct characteristics, such as specific conformations and/or nucleotide, substrate or ligand association. The connection between energy consumption and function is well understood in many cases, including diverse motor proteins [54, 165, 41, 152], the ribosome [162], polymerases [114], proteases [56], as well as kinases, which use ATP to phosphorylate their substrates.

This is different for the eukaryotic heat-shock protein Hsp90 studied herein. Similar to motor proteins, it undergoes large conformational changes and it hydrolyses ATP. However, no connection between the two has been found so far. In fact, the purpose of energy consumption (i.e. ATP hydrolysis) by Hsp90 is entirely unknown, and so is the molecular mechanism of its chaperone function. Nevertheless, it affects over 200 so-called client proteins [82]. To this end, Hsp90 relies on over 20 co-chaperones [148].

So, a vast number of interactions and Hsp90-dependent metabolic pathways have been described. But on the molecular and thermodynamic level, there are many open questions including:

- Do cochaperones couple conformational changes to energy consumption?
- Are the conformational dynamics affected by the inhibition of Hsp90's ATPase function?
- Are there specific switch-points in Hsp90's structure where we can interfere with these dynamics and/or function?
- Are the large conformational changes affected by increased viscosity and macromolecular crowding, similar to the cell interior?
- Is there a global interrelation between ATPase function and conformational dynamics - in the one or the other direction?

These key questions are addressed herein in single molecule detail by Förster resonance energy transfer (FRET). Single molecule time traces are particularly suited to investigate thermodynamic and kinetic questions. In fact, it is their unique feature to reveal the time evolution of one protein through individual kinetic states, notably in real time and at steady-state, without the need for external synchronization. This allows to explore the energy landscape, providing unparalleled insights into molecular driving forces.

Next to these great potentials, there are experimental limits of single molecule FRET, rendering quantitative, kinetic interpretations non-trivial. In view of these shortcomings, a single molecule analysis for complex kinetic se-

quences (SMACKS) was developed and custom-tailored to investigate protein machines, like Hsp90.

This thesis is structured as follows: [Chapter 2](#) provides a more detailed introduction on Hsp90. Fluorescence and FRET are introduced in [Chapter 3](#). Detection strategies for single molecule fluorescence are covered in [Chapter 4](#). A technique for pattern recognition in single molecule trajectories is introduced in [Chapter 5](#).

Part II holds central experimental features that were implemented and in many cases improved in the frame of this work. Namely the single molecule TIRF experiment ([Chapter 6](#)) and the optimized Hsp90 construct ([Chapter 7](#)). All further protocols are provided in the appendix, [Appendix B](#). The results part includes a critical evaluation of potentials and limits of single molecule FRET ([Chapter 8](#)), leading to the development of SMACKS presented in [Chapter 9](#).

In [Chapter 10](#) I discuss the complex kinetics of Hsp90's large conformational changes. The effect of diverse biochemical and physical interference with Hsp90 are presented in [Chapter 11](#) and [Chapter 12](#), respectively. I close with an outlook on protein kinetics in [Chapter 13](#) and a conclusion in [Chapter 14](#).

At last, the reader is informed that the term *transition rate* is used herein as shorthand for *transition rate constant*, as opposed to *particle flux*.

HEAT-SHOCK PROTEIN HSP90

The chaperone protein Hsp90 is a metabolic hub. This is manifested by its direct or indirect involvement in the function of roughly 20% of all yeast proteins [148]. It further constitutes 1-2% of the cytosolic mass [17], even more under stress conditions.

2.1 STRUCTURE & FUNCTIONAL ELEMENTS

The functional form of Hsp90 is a 10nm tall homo-dimer. [Figure 2.1a](#) shows the crystal structure of Hsp90 in a closed conformation. The Hsp90 protomer consists of three domains as indicated: the N(-terminal) domain, the middle domain and the C(-terminal) domain. In addition, Hsp90 occurs also in *open* conformations with dissociated N-domains ([Figure 2.1b](#)). But these have never been crystallized, which is attributed to tremendous conformational flexibility.

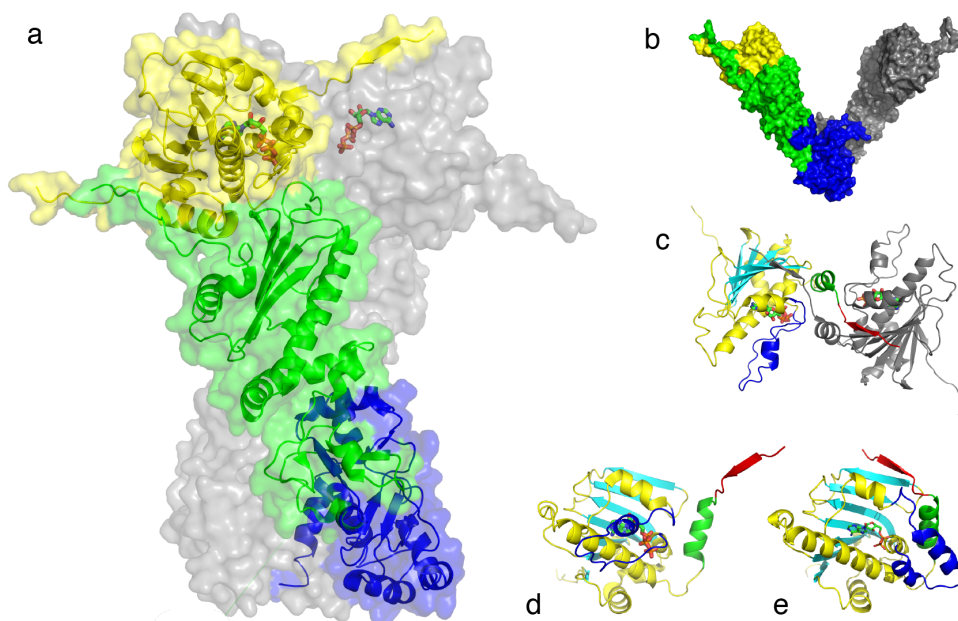


Figure 2.1: The structure of Hsp90. (a) Crystal structure (pdb:2cg9 [2]) in a closed conformation: N-domain, yellow; middle domain, green; C-domain, blue. The second protomer is displayed in gray, bound nucleotides as colored sticks. (b) Average open conformation determined by smFRET and MD [61]. (c) Top view of the N-domains with exchanged $\beta 1$ (red), $\alpha 1$ (green), closed ATP lid (blue) and β -sheet (cyan). (d,e) Side views of the N domains highlighting the closed (d) and open (e) ATP lid conformations and distinct $\beta 1$ association (pdb:1am1 [124]), color code as in (c).

Hsp90's N-terminal domain contains a nucleotide binding site with a very slow ATPase function. Interestingly, the ATP binding pocket is formed by a rare Bergerat fold, which is shared among GyrB, Hsp90, histidine kinase and MutL, hence called the GHKL ATPases. ATP is bound in a bent conformation representing a drugable motive (see below). Opposing N-domains form transient cross-protomer contacts including a strand swap of the very N-terminal β -sheet, subsequently referred to as β 1 (Figure 2.1c).

The N-domain is covalently linked to the middle domain by a charged linker, which is mostly unresolved in the crystal structure. Nevertheless, it has sequence-specific, functional relevance and interacts with the N domain [74]. Additionally, there are many more non-covalent interactions between both domains. Among the most important ones is the interaction of the catalytic loop (including the conserved arginine 380) with the nucleotide and neighboring residues, which is critical for ATP hydrolysis [106, 34]. Furthermore, the middle domain interacts with diverse cochaperones and clients (see below). The interface between the middle and C domain is involved in the global opening and closing. The C domain holds the main dimerization interface. The very C-terminal MEEVD motif further binds a specific class of cochaperones, the tetratricopeptide repeat (TPR)-domain proteins [117].

Many local conformational changes rely on each other. For instance, the β -strand swap is further stabilized by the closed ATP lid, uncovering additional attachment sites for the N-terminal β 1- α 1-segment (Figure 2.1d); whereas the open lid configuration favors intra-attachment of β 1 to the N-terminal β -sheet (Figure 2.1e) [122]. Also, the *active* conformation of the catalytic loop, which interacts with bound nucleotides, is only accessible if the ATP lid is closed. These three functional elements are sometimes called the *catalytic unit*. A cooperative behavior of the three was recently suggested [140].

2.2 CHAPERONE FUNCTION & REGULATION

Over 200 distinct proteins rely on maturation by Hsp90. Among these so-called *client* proteins, are many kinases involved in signal transduction, hormone receptors, *the guardian of the genome* p53 [87], but also cytoskeletal proteins, e.g. actin, tubulin, and many more [82, 117].

Nevertheless, eukaryotic Hsp90 is believed to treat its clients specifically, with the help of diverse cochaperones, such as the ATPase stimulating Aha1 (investigated herein, see Section 11.1), decelerating Sba1/p23, TPR-domain proteins like Sti1/Hop and Cpr6, kinase-specific Cdc37, prolyl-isomerases just to name a few [90, 91, 16, 154].

Hsp90's function is further regulated on various levels, from transcription down to the post-translational level. For example the central transcription factor Hsf1, which is part of the multifarious heat-shock response, is itself a client of Hsp90. Further downstream, many post-translational modifications have been characterized, including specific phosphorylation, Acetylation, SUMO-ylation and S-nitrosylation [110, 97, 132, 123].

In addition, the eukaryotic cell holds individual Hsp90 versions in the cytosol, the nucleus, the chloroplasts and the mitochondria. This work focuses on

the heat-inducible, cytosolic paralog of *Saccharomyces cerevisiae*, Hsp82 (uniprot entry: P02829).

Despite the enormous number of about 725 experimentally determined interactions with Hsp90 [123], only little is known about the molecular basis of Hsp90's function. In particular, the role of the ATPase activity in the chaperone function has remained elusive up to now [116]. Even the long-standing concept that ATPase activity is essential *in vivo* was severely questioned, just recently [168].

2.2.1 The role in cancer

Hsp90 is involved in all *Six Hallmarks of Cancer* [14]:

- Self-sufficient growth signals
- Insensitivity to antigrowth signals
- Evasion of apoptosis
- Limitless replicative potential
- Sustained angiogenesis
- Tissue invasion and metastasis

Due to this exceptional role, Hsp90 has become a major drug target in anti-cancer therapy. Cancer cells are virtually *addicted* to Hsp90, because of their uncontrolled and fast growth.

A classical therapeutic strategy exploits the unusual ATP conformation in Hsp90. It allows to target Hsp90 with great specificity. First candidates were natural products, such as geldanamycin produced by *Streptomyces hygroscopicus* [37] and radicicol originally isolated from *Monosporium bonorden* [38, 82]. Later, purine derived drug candidates were developed based on theoretical predictions [26, 72].

Apart from competitively blocking the nucleotide binding site, there are further strategies to inhibit Hsp90's chaperone function. Mainly there is a Novobiocin derived class of C-terminal inhibitors [95, 99, 7, 52].

All 4 classes of current drug candidates were investigated herein (see [Section 11.2](#)), to elucidate the effect of inhibition on the Hsp90 molecule.

FLUORESCENCE & FRET

Fluorescence is observed in nature in marine animals - such as the jellyfish depicted in [Figure 3.1](#) - but also in insects, plants and dead material like minerals.

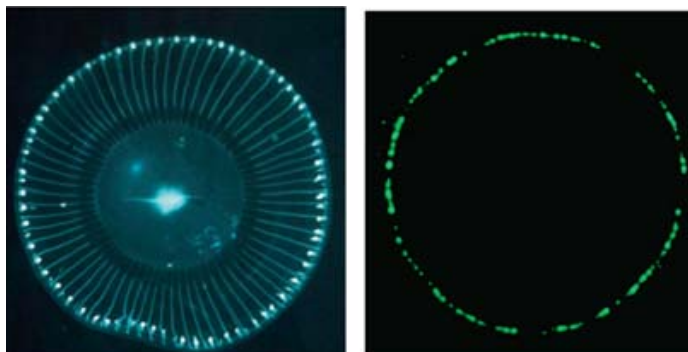


Figure 3.1: The jellyfish *Aequorea victoria* (left) and its fluorescent ring (right), originating from the green fluorescent protein (GFP). The characterization of GFP earned Osamu Shimomura the Nobel Prize in chemistry in 2008. Photographs are taken from the Nobel Lecture [142].

Physically, fluorescence is a byproduct of a molecule's relaxation from an electronically excited *high energy* state to a *low energy* ground state. This is detailed in the Jablonski diagram.

3.1 JABLONSKI DIAGRAM

Molecules exist in energetically distinct states that differ regarding electronic, vibrational and rotational properties [39] (see [Figure 3.2](#)). In a typical fluorophore, the energy difference between electronic states matches the energy of photons ($h\nu$) in the visible spectral range. In contrast, vibrational and rotational states are much closer in energy. For the latter, the energy difference is even less than thermal energy at room temperature (kT). Therefore, rotational transitions occur permanently without the need of further external energy. Singlet states S have antiparallel spin orientation, whereas triplet states T have parallel spin orientation.

The interaction of a photon with a molecule can lead to the *absorption* of the photon energy by the molecule. That is to say, the energy is converted into the excitation of an electron from the highest occupied molecular orbital (HOMO) to the lowest unoccupied molecular orbital (LUMO) - or a higher orbital, depending on the absorbed photon energy $h\nu$. The molecule is said to be excited from its electronic ground state S_0 to its electronically excited

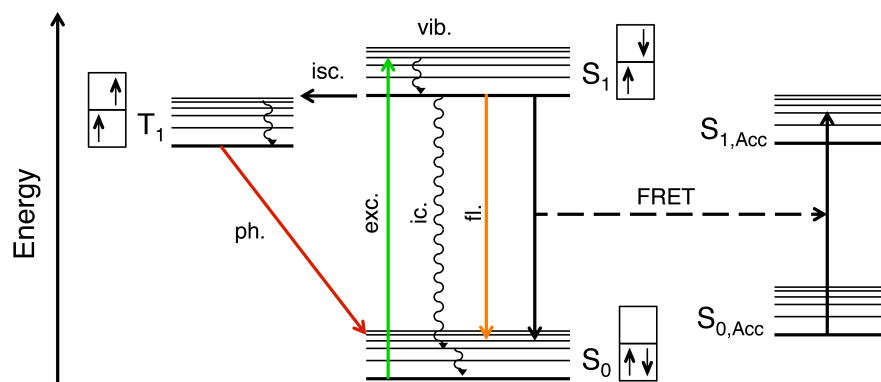


Figure 3.2: Jablonski diagram including electronic (bold) and vibrational (light) energy levels. Radiation related transitions are colored: excitation, exc.; fluorescence, fl.; phosphorescence, ph. Radiation-less transitions are depicted in black: vibrational relaxation, vib.; inter-system crossing, isc.; internal conversion, ic.; Förster resonance energy transfer, FRET, to an acceptor molecule, Acc. Thermal deactivation processes are indicated as curved arrows. The distinct electronic configuration of the triplet (T) and singlet (S) state is indicated by small boxes (HOMO, LUMO) and small arrows (spin state). Dexter transfer and photo-chemical reactions are not sketched.

state S_1 or $S_{>1}$. At room temperature, the transition occurs mainly from the vibrational ground state to a higher vibrational level of $S_{>0}$ (see below). It is followed by rapid vibrational relaxation, and if so, solvent relaxation.

Further relaxation can occur through various, *competing* processes [86]:

- Collisional quenching and solvent interaction causes thermal, radiation-less de-excitation (also termed *internal conversion*).
- Although *spin-forbidden*, due to spin-orbit coupling, there is a small but finite probability for a spin flip, i.e. *inter-system crossing* to the triplet state. The rate of such inter-system crossing depends on the overlap of ro-vibrational energy levels of the singlet and triplet system. Relaxation from T_1 to S_0 is very inefficient (i.e. unlikely), which leads to the long lasting phenomenon of phosphorescence.
- *Dexter electron transfer* through overlapping orbitals or further *photo-chemical reactions*.
- Energy transfer by FRET introduced in [Section 3.3](#).
- Alternatively, the energy can be released by the emission of a *fluorescence* photon.

Photon absorption - i.e. the electronic excitation of a molecule - occurs much faster ($< 10^{-15}$ s) than the motions of the molecule's nuclei, which is exploited by the *Born-Oppenheimer approximation*. Also vibrational ($\approx 10^{-12}$ s) and solvent relaxation ($\approx 10^{-10}$ s) occur comparatively fast. In contrast, the de-population of the excited state is the less efficient, which leads to a considerable dwell ($\approx 10^{-9} - 10^{-5}$ s) in that state. But the relaxation process itself occurs on similar, fast timescales as absorption.

3.2 PROPERTIES OF FLUORESCENCE

Due to the mentioned fast vibrational relaxation, fluorescence photons have less energy (longer wavelength) than the originally absorbed light. Hence, fluorescence spectra are said to be *red-shifted* with respect to the absorption spectra. This feature is also called *Stokes shift*.

In solution, it is further overlaid by *solvent relaxation*. During the dwell time in the excited state, the solvent molecules reorient to adapt to the altered charge density in the excited state, thus further decreasing the emitted photon energy.

At room temperature, the vibrational ground states are predominantly populated. As vibrational relaxation is comparatively fast, this holds also for the excited state. Consequently, the fluorescence spectrum is largely independent of the excitation wavelength (*Kasha rule*).

A further consequence of the diverse timescales involved, is the mirror symmetry between absorption and emission spectra (Figure 3.3). Specific electronic states often favor distinctive nuclear arrangements. As electronic transitions are much faster than the slow nuclear rearrangements, electronic transitions occur most efficiently between molecular arrangements with equal nuclear positions and momenta (i.e. overlapping vibrational wave functions) [39]. According to the *Franck-Condon principle*, the transitions are said to occur *vertically* in Figure 3.3. Because the vibrational energy levels are very similarly spaced in the electronic ground and excited state, this results in a mirror symmetry between the probability of diverse excitation and relaxation processes, and thus between the absorption and emission spectra.

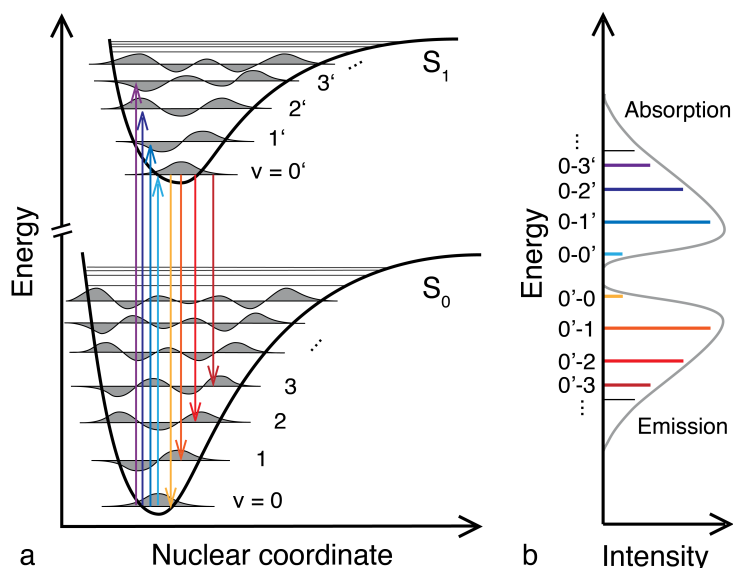


Figure 3.3: The Franck-Condon principle exemplified using a diatomic molecule. (a) Potential wells of the electronic ground state (S_0) and first excited state (S_1) as a function of the nuclear separation. Vibrational wave functions are depicted in gray. (b) Cartoon of corresponding absorption and emission spectra. The individual vibronic lines, colored as in (a), are smeared out in solution at room temperature (gray envelope). Image created based on [51].

The lifetime of the excited state - commonly referred to as *fluorescence lifetime* - is determined by the sum of all off-rates (see above):

$$\tau = \frac{1}{k_{fl} + k_{nr} + k_{ph}} \quad (3.1)$$

with k_{fl} , k_{nr} , k_{ph} , the rates of fluorescent, all non-radiative and phosphorescent relaxation, respectively. Many bright fluorophores have relatively long fluorescence lifetimes (e.g. 6 ns), owing to comparatively small non-radiative rates.

The fluorescence *quantum yield* specifies the fraction of fluorescent de-excitation among all excitation cycles. In the absence of significant phosphorescence, it is the fraction of emitted over absorbed photons.

$$\Phi = \frac{k_{fl}}{k_{fl} + k_{nr} + k_{ph}} = \frac{N_{em}}{N_{abs}}$$

3.3 FÖRSTER RESONANCE ENERGY TRANSFER

Named after Theodor Förster (1910-74), Förster resonance energy transfer (FRET) describes a radiation-less *Energiewanderung* (i.e. energy transfer) from a donor to an acceptor fluorophore [49]. Because the phenomenon is distance dependent in the nanometer range, it has become an important tool to reveal molecular processes in diverse research areas from biochemistry to material science. Yet, FRET occurs also as a natural process. In fact, in the mentioned jellyfish (Figure 3.1), GFP is excited through FRET by a bioluminescent aequorin complex [111, 81].

FRET occurs as a radiation-less dipole-dipole interaction between fluorophores [30]. As such the process depends strongly on the separation r of donor (D) and acceptor (A) dye, as well as, their relative orientation and spectral overlap (see Figure 3.4).

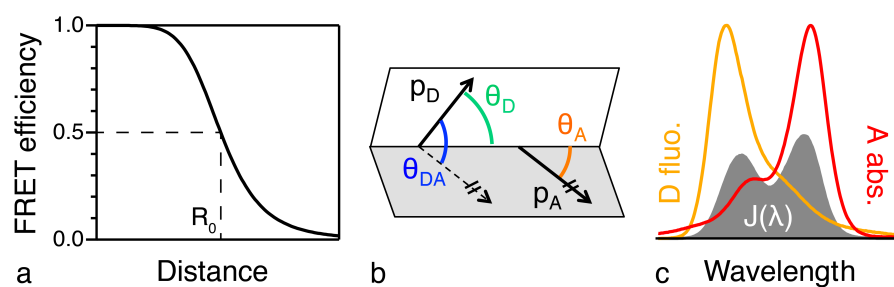


Figure 3.4: The dependence of FRET on (a) the inter-dye distance, (b) the dyes' relative orientation and (c) the overlap integral $J(\lambda)$ between the donor fluorescence (D fluo.) and acceptor absorption (A abs.) spectra.

The transfer rate is given by:

$$k_T = \frac{1}{\tau_D} \left(\frac{R_0}{r} \right)^6 \quad (3.2)$$

including the distance dependence expected for a dipole-dipole interaction and the sum of all competing off-rates, cf. Equation (3.1). All other dependencies are found in the Förster radius R_0 :

$$R_0 = \sqrt[6]{\frac{9000 \ln(10)}{128 \pi^5} \left(\frac{\Phi_D \kappa^2}{N_{Av} n^4} \right) J(\lambda)} \quad (3.3)$$

$$\kappa^2 = (\cos \theta_{DA} - 3 \cos \theta_D \cos \theta_A)^2 \quad (3.4)$$

$$J(\lambda) = \int_0^\infty F_D(\lambda) \epsilon_A(\lambda) \lambda^4 d\lambda \quad (3.5)$$

Here N_{Av} is the Avogadro constant and n the refractive index.

The orientational factor κ^2 is defined by Equation (3.4) with the angles $\theta_A, \theta_D, \theta_{DA}$ as shown in Figure 3.4b. If the dye's transition dipoles lie orthogonal to each other no transfer occurs and $\kappa^2 = 0$. In turn, a stacked, parallel orientation is optimal for transfer. In this case $\kappa^2 = 4$. Nevertheless, most studies exploit the fact that the dyes orientational correlation time is much smaller than the nanosecond dwell in the excited state. Accordingly, all possible orientations are usually sampled prior to eventual energy transfer. Thus the application of the average value $\langle \kappa^2 \rangle = 2/3$ is valid in most cases. Exceptions occur when the dyes are hindered in their rotational and translational diffusion, e.g. by sticking to a neighboring surface or through confinement at the attachment site. Even in the worst case, the distance errors are below 35% [86], because of the power of 6 dependence.

The overlap integral $J(\lambda)$ (in units of $\text{m}^3/\text{M} \propto \text{m}^6/\text{mol}$) is calculated from the donor's emission spectrum $F(\lambda)$ (normalized to unity) and the acceptor's spectral absorption coefficient $\epsilon_A(\lambda)$, see Equation (3.5).

As the transfer rate is not directly accessible by intensity-based experiments, the FRET efficiency E is usually considered. It is defined as the fraction of FRET among all de-excitation processes:

$$\begin{aligned} E &= \frac{k_T}{k_{fl} + k_{nr} + k_{ph} + k_T} = \frac{N_A/\Phi_A}{N_D/\Phi_D + N_A/\Phi_A} \quad (3.6) \\ &= \frac{N_A}{\Gamma \cdot N_D + N_A} \quad \text{with} \quad \Gamma = \frac{\Phi_A}{\Phi_D} \end{aligned}$$

As shown by the second and third identity, this can be expressed in terms of experimentally accessible (fluorescent) photon counts N_i together with the quantum yields Φ_i .

Finally, the distance dependence of the FRET efficiency follows by inserting Equation (3.2) into (3.6) and exploiting Equation (3.1):

$$E = \frac{1/\tau_D \left(\frac{R_0}{r} \right)^6}{1/\tau_D \left(1 + \left(\frac{R_0}{r} \right)^6 \right)} = \frac{1}{1 + \left(\frac{r}{R_0} \right)^6} \quad (3.7)$$

DETECTION OF SINGLE FLUOROPHORES

4.1 EXPERIMENTAL STRATEGIES

Tracking conformational changes of individual proteins by smFRET comes with two primary requirements.

First, it requires to detect the fluorescence of individual molecules, and moreover, to resolve varying intensity levels thereof. This asks for very low background fluorescence. To this end, there are two fundamentally different optical strategies:

- Minimizing the irradiated sample volume, e.g. using total internal reflection as discussed below.
- Minimizing the detection volume using a confocal geometry, which only detects rays originating from a narrow focal volume.

In addition, both concepts can be combined to generate minimal *overlap* between the excitation and detection volumes, e.g. using light sheet excitation in combination with confocal detection [104].

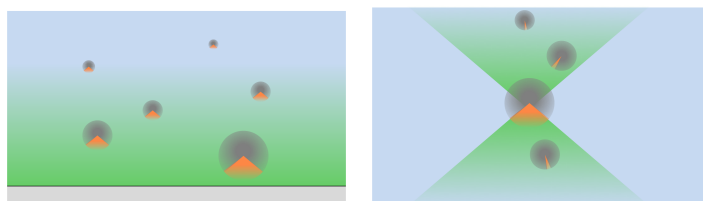


Figure 4.1: The 2 primary strategies to resolve single fluorophores: (left) minimal irradiated volume (e.g. TIRF); (right) minimal detected volume (confocal detection). Individual fluorophores are depicted as gray spots. Their size corresponds to the incident excitation intensity. The collected cone of light is highlighted in orange for each fluorophore individually. Excitation light is shown in green, buffer blue and the coverslip in gray.

Second, monitoring conformational changes requires to track the fluorescence of an individual molecule *over time*. This can be achieved by:

- surface immobilization [138, 22]
- geometric confinement: nano-dimples or ultra-thin flow chambers [10].
- tethering to immobile objects, such as magnetic [80] or optical [88] tweezers, and under hydrodynamic flow, cf. DNA curtains [155], etc.
- electrokinetical trapping [31, 160] (tether-free)
- 3D fluorophore tracking in solution [118] (tether-free)

Among these approaches, surface immobilization is the most straight-forward and therefore the most widely used technique, whereas the other techniques represent special solutions to specific questions; e.g. to study biomolecular

interactions at low concentrations, to study proteins that can not be immobilized, to combine fluorescence with further analytical tools. The later named techniques are less frequently used for mere fluorescence spectroscopy due to sophisticated instrumentation, low through-put and data yield, and/or decreased compatibility with high-sensitivity fluorescence detection.

Within this work, a new conjugation technique was established that allows to attach Hsp90 specifically to a functionalized surface (see [Chapter 7](#)). Consequently, it is convenient to exploit this surface to confine the excitation volume in TIRF geometry.

4.2 THE PHYSICS OF TOTAL INTERNAL REFLECTION

Appart from being useful in science, total internal reflection (TIR) creates stunning phenomena at the sea air interface as shown in [Figure 4.2](#).



Figure 4.2: TIR of a sea turtle at the sea/air interface [73].

[Figure 4.3](#) depicts the situation at such an interface between media with distinct refractive indices $n_1 > n_2$ from optical perspectives. A light beam coming from an optically dense medium to a less dense medium is split at the interface in a reflected and a transmitted beam [40]. For a plane wave with the electric field $E_1(\vec{r}, t)$ encountering such a change in refractive index

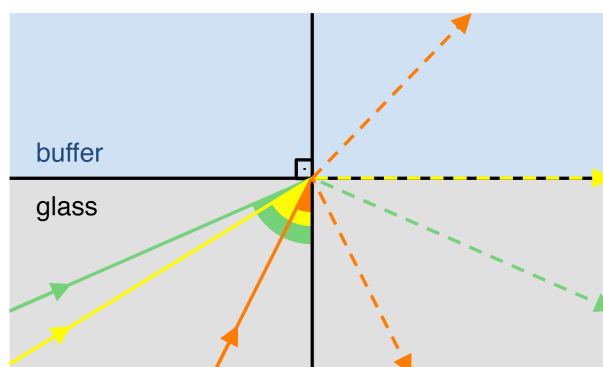


Figure 4.3: Refraction at a glass/buffer interface. Beams with 3 different incident angles θ_1 are shown: sub-critical (orange), critical (yellow) and super-critical (green), as introduced in the text.

in the xy -plane, this results in a reflected wave $E_1'(\vec{r}, t)$ in medium 1 and a transmitted wave $E_2(\vec{r}, t)$ in medium 2:

$$\begin{aligned} E_1(\vec{r}, t) &= A \cdot e^{i(\vec{k}_1 \vec{r} - \omega t)} = A \cdot e^{ik_1(\sin \theta_1 \cdot x + \cos \theta_1 \cdot z)} \cdot e^{-i\omega t} \\ E_1'(\vec{r}, t) &= B \cdot e^{ik_1(\sin \theta_1 \cdot x - \cos \theta_1 \cdot z)} \cdot e^{-i\omega t} \\ E_2(\vec{r}, t) &= C \cdot e^{i(\vec{k}_2 \vec{r} - \omega t)} = C \cdot e^{ik_2(\sin \theta_2 \cdot x + \cos \theta_2 \cdot z)} \cdot e^{-i\omega t} \end{aligned} \quad (4.1)$$

with the amplitudes, A, B, C , the position vector $\vec{r} = x \cdot \vec{e}_x + z \cdot \vec{e}_z$, the respective wave vector \vec{k}_i , its norm $k_i = |\vec{k}_i|$ and the angular frequency $\omega = 2\pi\nu$. For small angles of incidence θ_1 most of the incident intensity is transmitted into the less dense medium, where - according to Snell's law, Equation (4.2) - it propagates at a larger angle θ_2 .

$$\frac{n_1}{n_2} \cdot \sin(\theta_1) = \sin(\theta_2) \quad (4.2)$$

$$\theta_{\text{crit}} = \arcsin\left(\frac{n_2}{n_1}\right) \quad (4.3)$$

For increasing angles θ_1 the portion of reflected intensity increases until the *critical angle* defined by Equation (4.3), where no propagation through medium 2 is observed anymore. Insertion into Equation (4.2) yields $\sin(\theta_2) = 1$ and θ_2 equals 90° . For a conventional glass-water-interface with refractive indices $n_1 = 1.52$ and $n_2 = 1.33$, a critical angle of 61° is found.

All beams with super-critical angles $\theta_1 > \theta_{\text{crit}}$, show total internal reflection. For these beams, the left hand side of Equation (4.2) becomes >1 . This requires an imaginary $\cos(\theta_2)$:

$$\cos^2 \theta_2 = 1 - \sin^2 \theta_2 < 0 \quad (4.4)$$

Importantly, total internal reflection occurs only if $n_1 > n_2$, which again follows directly from Equation (4.2).

4.2.1 Quantum-Mechanical Derivation of the Evanescent Wave

The evanescent wave in medium 2 is easily derived by comparing TIR to a free particle encountering a potential energy step (Heaviside step potential) [39]. As illustrated in Figure 4.4, we consider only the normal contributions of the incident wave vector $k_z = k_1 \cdot \cos(\theta_1)$. For $z < 0$ the potential energy

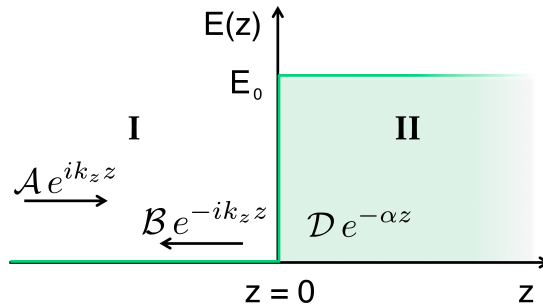


Figure 4.4: The Heaviside step potential.

is zero and the total energy is purely kinetic. At $z \geq 0$ the potential is higher than the kinetic energy of the incident particle:

$$\begin{aligned} z < 0: \quad E_{\text{pot},1} = 0 &\Rightarrow E_{\text{tot},1} = E_{\text{kin},1} = \frac{(\hbar k_z)^2}{2m} \\ z \geq 0: \quad E_{\text{pot},2} = E_0 &\Rightarrow E_{\text{tot},2} = E_{\text{kin},1} - E_0 = \Delta E < 0 \end{aligned}$$

The corresponding stationary Schrödinger equations are:

$$\begin{aligned} z < 0: \quad -\frac{\hbar^2}{2m} \frac{d^2\Psi}{dx^2} = E_{\text{kin},1} \Psi = \frac{(\hbar k_z)^2}{2m} \Psi &\Leftrightarrow \frac{d^2\Psi}{dx^2} = -k_z^2 \Psi \\ z \geq 0: \quad -\frac{\hbar^2}{2m} \frac{d^2\Psi}{dx^2} = \Delta E \Psi &\Leftrightarrow \frac{d^2\Psi}{dx^2} = \alpha^2 \Psi \\ \text{with: } \alpha = \sqrt{-2m\Delta E}/\hbar \in \mathbb{R} \end{aligned}$$

where α is real because $\Delta E < 0$.

Their general solutions are then:

$$\begin{aligned} z < 0: \Psi_1 &= \mathcal{A} \cdot e^{ik_z z} + \mathcal{B} \cdot e^{-ik_z z} \\ z \geq 0: \Psi_2 &= \mathcal{C} \cdot e^{\alpha z} + \mathcal{D} \cdot e^{-\alpha z} = \mathcal{D} \cdot e^{-\alpha z} \end{aligned}$$

Ψ_1 consists of the incident plane wave (first summand) and the reflected plane wave (second summand). Ψ_2 can only be normalized for $\mathcal{C} = 0$. All other amplitudes $\mathcal{A}, \mathcal{B}, \mathcal{D}$ are determined by requiring continuous differentiability at $z = 0$.

Importantly, with $\mathcal{D} \neq 0$, the wave *does* enter the classically forbidden zone $z \geq 0$, as an exponentially decaying *evanescent wave*. Nevertheless, energy is conserved, because the wave does not propagate in z -direction. Consequently, there is no energy transport into medium 2.

4.2.2 The Evanescent Penetration Depth

In TIRF experiments, the excitation intensity and, in particular, its extent in z -direction are crucial for maximum sensitivity, as introduced earlier. The intensity that is available for fluorophore excitation in medium 2 is given by:

$$I(z, z \geq 0) = |\Psi_2|^2 = |\mathcal{D}|^2 \cdot e^{-2\alpha z} \propto e^{-z/d} \quad (4.5)$$

It decays exponentially with the decay constant d , which is also referred to as the *penetration depth*. This is the distance where still $1/e = 37\%$ of the incident intensity is found [39].

To derive d , we exploit the correspondence to the classical wave, Equation (4.1). The intensity (z -component) of a wave in medium 2 is given by:

$$I(z, z \geq 0) = |E_{2,z}|^2 = |C|^2 \cdot e^{2(i k_2 \cos \theta_2 \cdot z)} \quad (4.6)$$

where in the case of total internal reflection $\cos \theta_2$ is imaginary (cf. above). Comparing the exponents of Equations (4.5) and (4.6) leads to:

$$-1/d = 2ik_2 \cos \theta_2 = 2ik_0 n_2 \cos \theta_2$$

where $k_0 = k_2/n_2$ is the wave vector in vacuum. Using Equations (4.2) and (4.4), we get:

$$1/d = 2k_0 n_2 \cdot \sqrt{\sin^2 \theta_2 - 1} = 2k_0 \sqrt{n_1^2 \sin^2 \theta_1 - n_2^2}$$

Finally, with $k_0 = 2\pi/\lambda_0$, the penetration depth is determined by well known quantities [86]:

$$d = \frac{\lambda_0}{4\pi\sqrt{n_1^2 \sin^2 \theta_1 - n_2^2}}$$

To conclude, let us consider a light wave that hits a glass-water-interface ($n_1 = 1.52$; $n_2 = 1.33$) at $\theta_1 = 65^\circ$. The intensity of the resulting evanescent wave has a penetration depth of $d = 125\text{nm}$ for $\lambda_0 = 532\text{nm}$ or $d = 150\text{nm}$ for $\lambda_0 = 635\text{nm}$, respectively.

4.3 THE TIR FLUORESCENCE MICROSCOPE

There are 2 common ways to implement TIR excitation in a fluorescence microscope: either using a prism as in Figure 4.5a or by means of an objective with high numerical aperture (Figure 4.5b) [86, 138]. In both configurations, the *inverted* microscope is the prevailing geometry.

In the first case, excitation and detection occur on *opposite* sides of the sample. A trapezoidal prism enables efficient coupling of the excitation light into the glass. At a super-critical angle, TIR forms at the coverslip-buffer interface. Unfavorable reflections at the prism-coverslip interface are minimized by choosing materials with comparable refractive indices and applying a corresponding immersion liquid in between. The resulting fluorescence is detected by the objective from the *opposite* side of the chamber. Thus very thin chambers are required if objectives with high numerical aperture - and therefore high detection efficiency - are to be used.

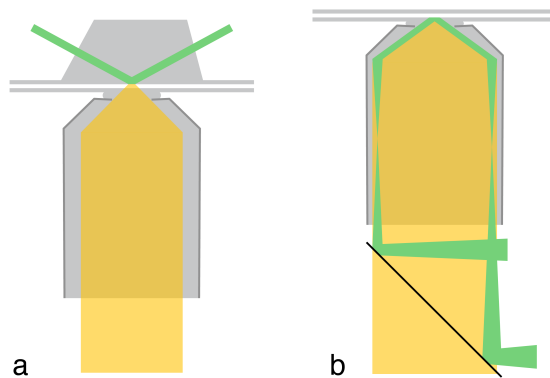


Figure 4.5: Two construction schemes for TIR microscopy (lateral cuts). Both share the inverted microscope geometry: the specimen is above the objective with an immersion liquid in between. Here the specimen consists of a thin coverslip-buffer-coverslip chamber. Materials in grey share the same refractive index. Buffer is transparent, the excitation light is green and the fluorescence yellow. (a) A trapezoidal prism is used generate TIR at the coverslip-buffer interface. The resulting fluorescence is collected by the objective from the *opposite* side of the chamber. (b) In objective-type TIRF, the same objective is used for TIR excitation and detection. The excitation beam enters the objective via an additional dichroic mirror (black).

In contrast, for objective-type TIRF, an objective with high numerical aperture is mandatory. It is used for both, excitation and detection from the same side of the chamber. TIR is obtained by shifting the beam away from the optical axis until the light reaches the coverslip-buffer interface at a super-critical angle.

As indicated in [Figure 4.5b](#), objective-type TIRF requires an extra dichroic mirror to separate the excitation and emission light. The light loss (<5%) associated with this extra component represents a disadvantage compared to the prism-type TIRF configuration. Moreover, powerful dichroic mirrors with multiple highly transmissive spectral bands are rare, which restricts the implementation of multi-color setups in this configuration.

On the other hand, the accessibility of the chamber *from top* allows for convenient combination with an additional functionality, such as force spectroscopy, bright field illumination etc. Once implemented, objective-type setups are usually easier to operate. In particular, they produce a spatially uniform excitation profile, which is stable for months.

SINGLE MOLECULE PATTERN RECOGNITION

Single molecule data is inherently noisy. After the development of techniques to detect single molecule trajectories in liquid phase at room temperature (first ion channels trajectories date from the 1970's [113]), researchers were challenged with the analysis of data with very low signal to noise ratio. Because of the broadband noise, conventional filters used in signal processing are not applicable here. Instead the field employs mathematical models that were previously used for pattern recognition in the context of speech and handwriting [9, 8]. Namely hidden Markov models (HMMs) became very popular in the pioneering ion channel field [29] and later on also among fluorescence [5, 102] and force spectroscopists [143, 20, 83].

5.1 THE PARAMETRIZATION OF HIDDEN MARKOV MODELS

The central idea behind HMMs is the explicit distinction between experimental observations (i.e. measured signals) and their subsequent interpretation, e.g. as open and closed states. Thereby, the interpretations are limited to a predefined number of states, which allows to define a mathematical relation between the observations and their interpretation as symbolic states, which is illustrated in Figure 5.1.

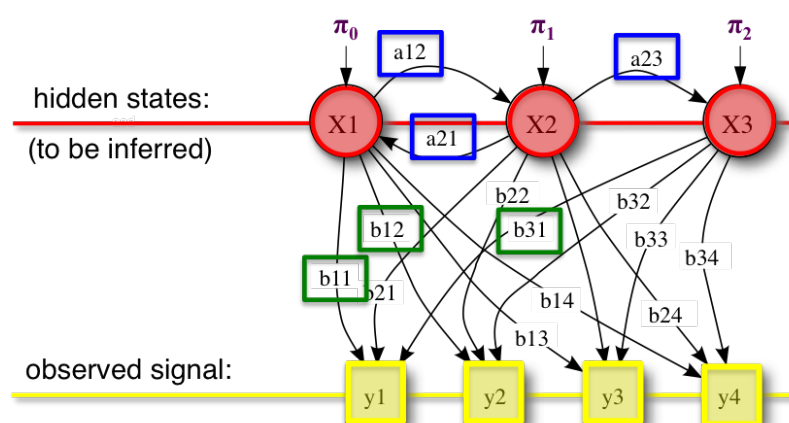


Figure 5.1: The relation between observed signals y and hidden states X is defined by the HMM parameters π , a , b introduced in the text. Image adapted from [151].

The actual observation level (yellow) and the abstract interpretation level (red) are connected by a model $\lambda(\boldsymbol{\pi}, \mathbf{A}, \mathbf{B})$ consisting of:

π_i = start probability

a_{ij} = transition probabilities

b_{ik} = emission probabilities

where the indices i, j denote individual states and k is a specific observation or signal [126, 47]. The probabilities to begin a given trajectory in a given state comprise the start probability vector. The matrix \mathbf{A} contains normalized transition probabilities between all states. The \mathbf{B} parameters describe the probabilities b_{ik} of a given state i to emit a certain observed signal k . Instead of discrete emission probabilities, continuous signals (e.g. fluorescence intensities) are better described by continuous emission probability density functions (PDFs) b_i . They assign each signal a specific emission probability b_{ik} . Herein one Gaussian PDFs is used per state, parametrized by the mean μ_i and variance V_i .

These definitions lead to 2 important consequences. First, HMMs are only applicable to memory-less kinetic systems. This is because the transition to a new state j depends only on the current state i and the corresponding transition probabilities a_{ij} . This requirement is called *Markov property*. Second, time-homogeneous behavior (or *steady-state*) is required, since the transition probabilities are constant over time,

5.2 THE CANONICAL ALGORITHMS

In order to describe the data with the model as accurately as possible, three tasks must be completed [126]:

- The ultimate goal is to *decipher* the underlying states causing the observed data.
- This requires to *optimize* model parameters that describe the data as accurately as possible,
- which, in turn, asks for a way to *rate* the model parameters.

These tasks are numerically completed by the corresponding 3 algorithms, introduced below. A frequent architecture is shown in [Figure 5.2](#).

Maximum likelihood (ML) serves here as optimality criterion for parameter estimation. The central relation within the ML formalism is Baum's auxiliary function \mathbf{Q} :

$$\mathbf{Q}(\lambda, \tilde{\lambda}) = \sum_{\mathbf{Q}} P(\mathbf{Q}|\mathbf{O}, \lambda) \cdot \log[P(\mathbf{O}, \mathbf{Q}|\tilde{\lambda})]$$

It was shown that maximization of that function with respect to all 3 parameters generates models $\tilde{\lambda}(\tilde{\boldsymbol{\pi}}, \tilde{\mathbf{A}}, \tilde{\mathbf{B}})$ of increased likelihood [12]. The update equations (see [Section 5.2.2](#)) are obtained by setting the corresponding partial derivatives to zero. The explicit formalism of each algorithm is found below. The indices i, j denote states. t are discrete time steps and T is the total time. \mathbf{O} (capital) is the set of observables and \mathbf{x}_t is a specific observable at time t in d dimensions.

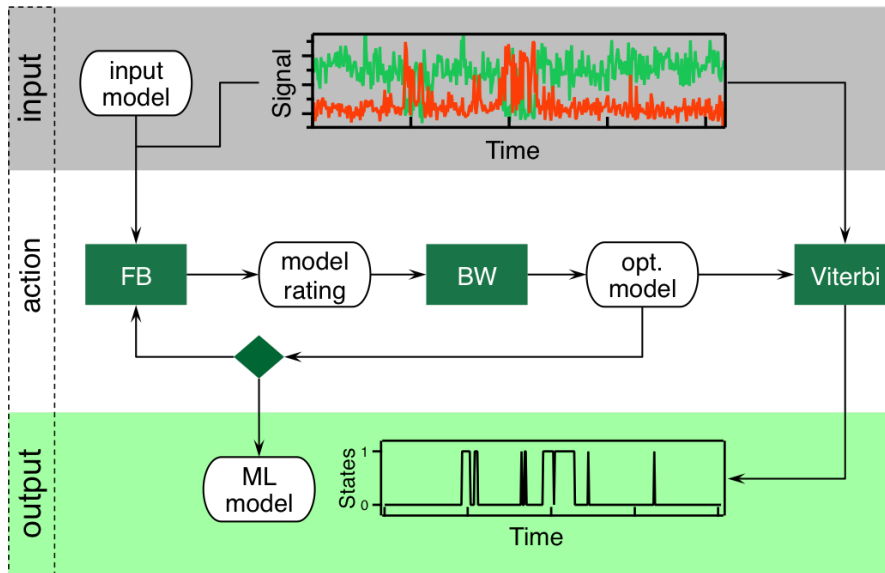


Figure 5.2: The algorithm architecture frequently used in HMM analysis. The fit of the data and the input model are rated by the Forward-Backward algorithm (FB), which is the basis for parameter optimization by the Baum-Welch algorithm (BW). The optimized (opt.) model is iteratively improved until convergence to maximum likelihood (ML). The Viterbi algorithm decodes the optimal state sequence given the data and the model.

5.2.1 The Forward-Backward Algorithm

The *Forward-Backward* algorithm (FB) rates the fit of the data and the model by recursively computing the probability of the observed data given the model, $P(O|\lambda)$. The forward and backward variables, α and β , are auxiliary probabilities required for the Baum-Welch algorithm below.

$$\begin{aligned}
 \text{initiation:} & \quad \alpha_{t=1}(i) = \pi_i b_i(\mathbf{x}_{t=1}) \\
 \text{recursion:} & \quad \alpha_{t+1}(i) = \sum_j [\alpha_t(j) a_{ji}] b_i(\mathbf{x}_{t+1}) \\
 \text{termination:} & \quad P(O|\lambda) = \sum_i \alpha_T(i) \\
 \text{initiation:} & \quad \beta_T(i) = 1 \\
 \text{recursion:} & \quad \beta_t(i) = \sum_j a_{ij} b_j(\mathbf{x}_{t+1}) \beta_{t+1}(j) \\
 \text{termination:} & \quad P(O|\lambda) = \sum_i \pi_i b_i(\mathbf{x}_1) \beta_{t=1}(i)
 \end{aligned}$$

$P(O|\lambda)$ is called the production probability of the data given the model. It is equivalent to the likelihood of the model given the data $\mathcal{L}(\lambda|O)$:

$$\mathcal{L}(\lambda|O) = \sum_S [\pi_{s_1} \cdot \prod_T (a_{s_{t-1}s_t} \cdot b_{s_t}(\mathbf{x}_t))]$$

where the sum goes over all possible state sequences S , and s_t denotes the state at time t .

5.2.2 The Baum-Welch algorithm.

Based on FB, the *Baum-Welch* algorithm (BW) optimizes the parameters by maximizing Baum's auxiliary function with respect to all three parameters. The basis for calculating the updated parameters are $\gamma_t(i)$ and $\gamma_t(i, j)$, the respective probabilities for a given state or transition at a given time point.

$$\begin{aligned}\gamma_t(i) &= \alpha_t(i) \beta_t(i) / P(O|\lambda) \\ \gamma_t(i, j) &= \alpha_t(i) a_{ij} b_j(\mathbf{x}_{t+1}) \beta_{t+1}(j) / P(O|\lambda)\end{aligned}$$

The parameter update equations are:

$$\begin{aligned}\hat{\pi}_i &= \gamma_{t=1}(i) \\ \hat{a}_{ij} &= \sum_{t=1}^{T-1} [\gamma_t(i, j)] / \sum_{t=1}^{T-1} \gamma_t(i) \\ \hat{\mu}_i &= \sum_{t=1}^T [\gamma_t(i) \mathbf{x}_t] / \sum_{t=1}^T \gamma_t(i) \\ \hat{V}_i &= \sum_{t=1}^T [\gamma_t(i) \mathbf{x}_t \mathbf{x}_t^T] / \sum_{t=1}^T \gamma_t(i) - \boldsymbol{\mu}_i \boldsymbol{\mu}_i^T\end{aligned}$$

5.2.3 The Viterbi Algorithm

The Viterbi algorithm decodes the most probable state sequence s^* given the data and the model. It is recursively deduced from the δ and ψ variables.

$$\begin{aligned}\text{initiation:} & \quad \delta_{t=1}(i) = \pi_i b_i(\mathbf{x}_{t=1}) \\ \text{recursion:} & \quad \delta_{t+1}(j) = \max_i [\delta_t(i) a_{ij}] b_j(\mathbf{x}_{t+1}) \\ \text{termination:} & \quad P^*(O|\lambda) = P(O, s^*|\lambda) = \max_i \delta_T(i) \\ & \quad s_T^* = \underset{j}{\operatorname{argmax}} [\delta_T(j)] \\ \text{initiation:} & \quad \psi_{t=1}(i) = 0 \\ \text{recursion:} & \quad \psi_{t+1}(j) = \underset{i}{\operatorname{argmax}} [\delta_t(i) a_{ij}] \\ \text{back-tracking:} & \quad s_t^* = \psi_{t+1}(s_{t+1}^*)\end{aligned}$$

Part II

EXPERIMENT

SINGLE MOLECULE FRET TIME TRACES

6.1 DESIGN OF THE TIRF MICROSCOPE

An objective-type TIRF microscope was built to detect protein conformational changes by smFRET. At the core of the setup shown in Figure 6.1 is the objective (Nikon, Apo TIRF) with high numerical aperture, $NA = 1.49$, and 100x magnification. It is used for both, TIR illumination and fluorescence signal collection.

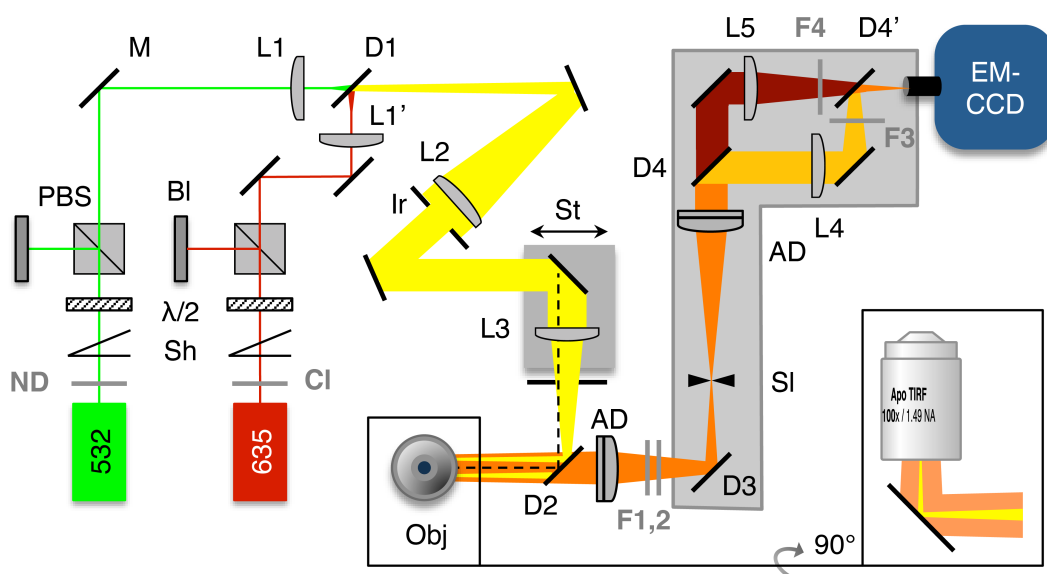


Figure 6.1: Design of the TIRF microscope. 532 and 635 denote lasers with respective wavelengths. F, filters including: ND, neutral density; CI, clean up. Sh, shutter. $\lambda/2$, half-wave plate. PBS, polarizing beam splitter. BI, beam blocker. $\lambda/4$, quarter-wave plate. M, mirror. L, lens. D, dichroic mirror. Ir, iris. St, translation stage. Obj, 100x 1.49 NA objective. AD, achromatic doublet lens. SI, tunable slit. EMCCD, electron multiplying charge-coupled device camera. The detection pathway is framed in gray. A dashed black line indicates the *on-axis* path to the objective, in contrast to the displayed *off-axis* path for TIR illumination. The inset shows a side view of the objective with the *out-of-plane* mirror below. Specifications of all components are provided in Table B.1.

Two excitation lasers (for direct excitation of the FRET donor and acceptor dye) are aligned and guided towards the objective. Their intensity is fine-tuned using a half-wave plate ($\lambda/2$) in combination with a polarizing beam splitter (PBS). Laser powers of about 10 μW were used for the measurements (see calibration plot in Figure A.3).

To avoid large differences in excitation intensity over the field of view, a very flat beam profile is key. Therefore, both excitation beams were expanded

40-fold between L1/L1' (focal length, $f = 25\text{mm}$) and L2 ($f = 1000\text{mm}$). An iris constrains the collimated beam to a diameter of 2cm. The beam is then focused onto the back focal plane of the objective by lens L3, generating collimated rays at the object plane. TIR illumination is obtained by shifting the beam off-axis using the translation stage St.

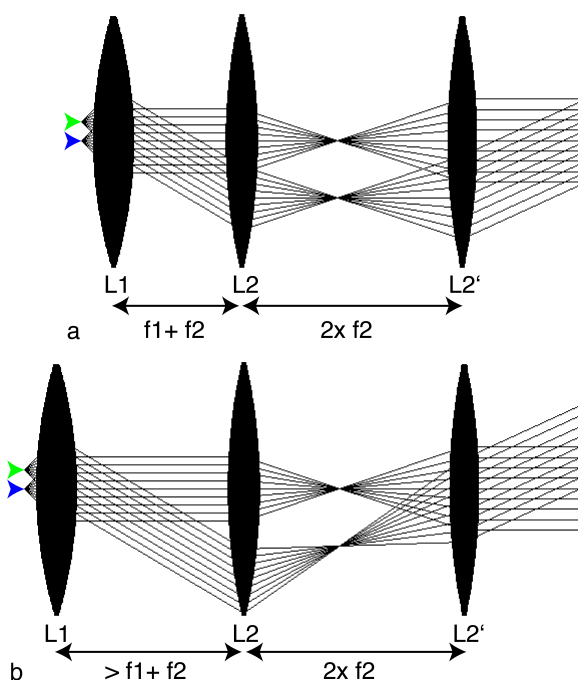


Figure 6.2: For off-center rays (green arrow) the correct lens separation is critical even in the collimated space. (a) Lenses positioned in compliance with the focal lengths f_1 , f_2 of lenses L1 and L2. (b) Increased deviation and titled foci (between L2 and L2') occur if the separation between L1 and L2 does not fit. Central beams (blue arrow) are not affected. Images created using an optics applet ².

The collected fluorescence exits the objective as infinity corrected rays. It is a common misconception that these rays would run along the optical axis until infinity, which is only true for rays originating from a point source on the optical axis. However, to image a field of view with non-zero extension in x and y (i.e. perpendicular to the optical axis), special care must be taken for the rays originating from off-center positions as illustrated in Figure 6.2. Therefore, the achromatic tube lens and all remaining lenses are positioned in accordance with their focal lengths - even in the collimated space. This ensures minimal diversion and straight foci also for off-center rays.

The fluorescence is separated from excitation light by long pass and notch filters. Off-axis beams are further removed by an optical slit together with achromatic slit lenses. Finally donor and acceptor fluorescence is split by the dichroic mirror D4, spectrally filtered again and individually focused side by side onto the EMCCD (Andor iXonUltra) by best form silica lenses. Translation stages were used to fine-tune the lens positions.

The final magnification of the setup was 100x. The specimen (see next section) is brought into focus by a piezo focusing system (PIFOC, Physik Instrumente).

² http://webphysics.davidson.edu/alumni/MiLee/java/Final_Optics/optics.htm; last accessed: 11/27/2016.

6.2 SINGLE MOLECULE TIRF MEASUREMENTS

Measurements were performed in a homemade flow chamber depicted in [Figure 6.3a](#). Coupled to a syringe pump (Harvard apparatus), this enables easy buffer exchange. It is built from two coverslips (cf. next section) and a spacer mask (Nescofilm) by compression at 70°C. Horizontal and vertical translation stages (both Thorlabs) allowed for micro-meter positioning of the flow chamber in x-, y-, and z- direction.

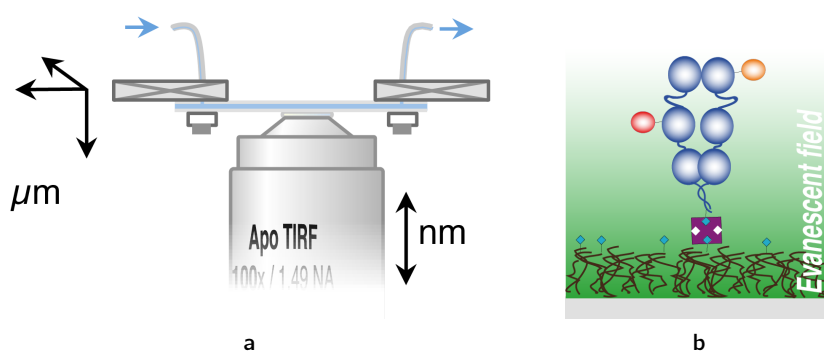


Figure 6.3: The flow chamber and a zoom view of an immobilized biomolecule. (a) The flow chamber is positioned on top of the objective with immersion oil in between. Glass is shown in light gray, buffer in blue. Buffer inlet and outlet tubings are indicated by blue arrows. Metallic parts are drawn with dark gray contours. Translational degrees of freedom are indicated by black arrows with specified step size. (b) A fluorescently labeled biomolecule (blue) is immobilized on a PEG brush (brown) within the evanescent field (green). Dyes are depicted in red and orange, biotins as turquoise diamonds, Neutraavidin in purple, coverslip in gray.

A polyethylene glycol (PEG)-passivated coverslip (for PEGylation protocol see [Section B.3](#)) is used as a substrate for the immobilization of biotinylated and fluorescently labeled biomolecules ([Figure 6.3b](#)). To this end, the flow chamber is incubated with a Neutraavidin solution (0.1 μM; Thermo Fisher), flushed with buffer and pre-bleached at maximal laser power. Only now the sample solution is applied at low pico-molar concentrations resulting in a few hundred fluorophores within the field of view.

Movies of this *starry sky* were captured with a water-cooled EMCCD (chip cooled to -90°C). A maximum frame rate of 55Hz in full frame (512x512 pixels) was achieved using *frame-transfer* mode and continuous illumination. Alternatively, for alternating laser excitation (ALEX), the camera was operated in *external exposure* mode. Image acquisition and optical shutters were synchronized by a custom-built electronic circuit and a master trigger (TTL signal) to achieve 100 ms exposure to each ALEX channel. The resulting 5Hz ALEX sampling was used throughout this work, unless specified differently.

6.3 LOW AUTO-FLUORESCENCE FLOW CHAMBERS

Conventional glass coverslips (Roth) show unfavorable red autofluorescence upon green excitation (Figure 6.4a). Therefore, the borosilicate glass was replaced by electronically fused silica (Spectrosil 2000, Heraeus). Figure 6.4b shows the minimal auto-fluorescence background observed with silica coverslips (custom-built by UQG optics, 24mm x 50mm x 150 μ m) in contrast to conventional glass coverslips.

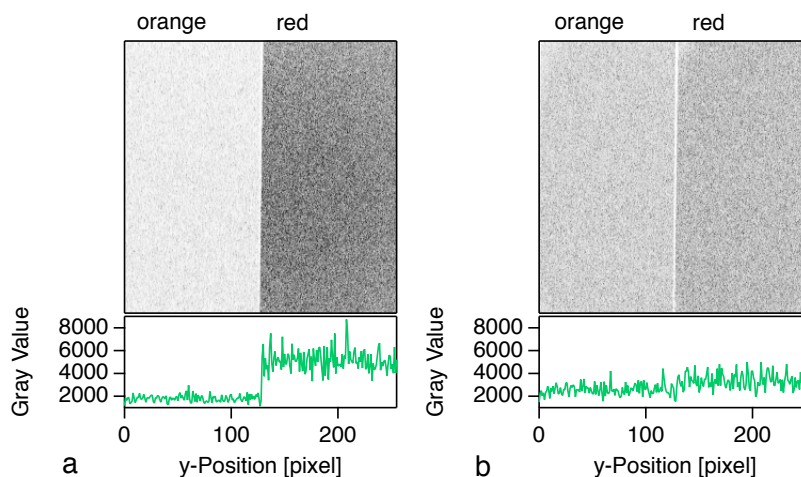


Figure 6.4: EMCCD images of orange and red fluorescence after green excitation obtained using glass (a) or silica coverslips (b). Low/high intensity is shown in white/black, respectively. A line profile through the middle is displayed below each. Conventional glass creates a bright, red auto-fluorescence background signal, whereas silica generates little background signal in both channels.

However, silica comes with a slightly different refractive index of 1.46 as compared to 1.52 for glass. This change in refractive index leads to a modified beam path (Figure 6.5), on the one hand, and partial reflections, on the other hand. The required geometric adjustments were reached by a small tilt away from the optical axis. The remaining background signal in Figure 6.4b and associated noise level originates mainly from elastically scattered light, which was further reduced by a long-pass filter. Altogether, silica coverslips led to an overall increased signal to noise ratio. A distortion of the image was not observed.

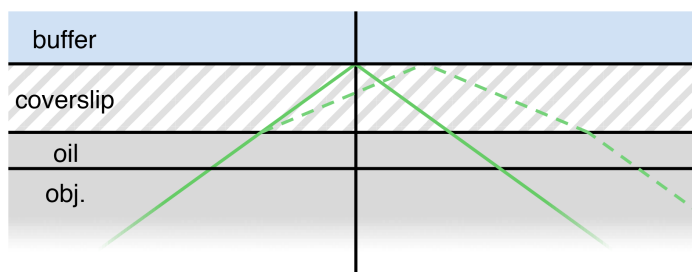


Figure 6.5: The shifted geometry introduced by silica coverslips (green, dashed) compared to the standard beam path (green). The vertical line indicates the optical axis of the objective.

6.4 SMFRET DATA PREPARATION

Figure 6.6 illustrates the data preparation steps from raw data to interpretable results. The raw data obtained from the EMCCD consists of TIF-stacks, as displayed in Figure 6.6a. Each frame holds an image of the donor next to the acceptor channel. In ALEX experiments, odd frames are excited by the green laser and even frames by the red laser.

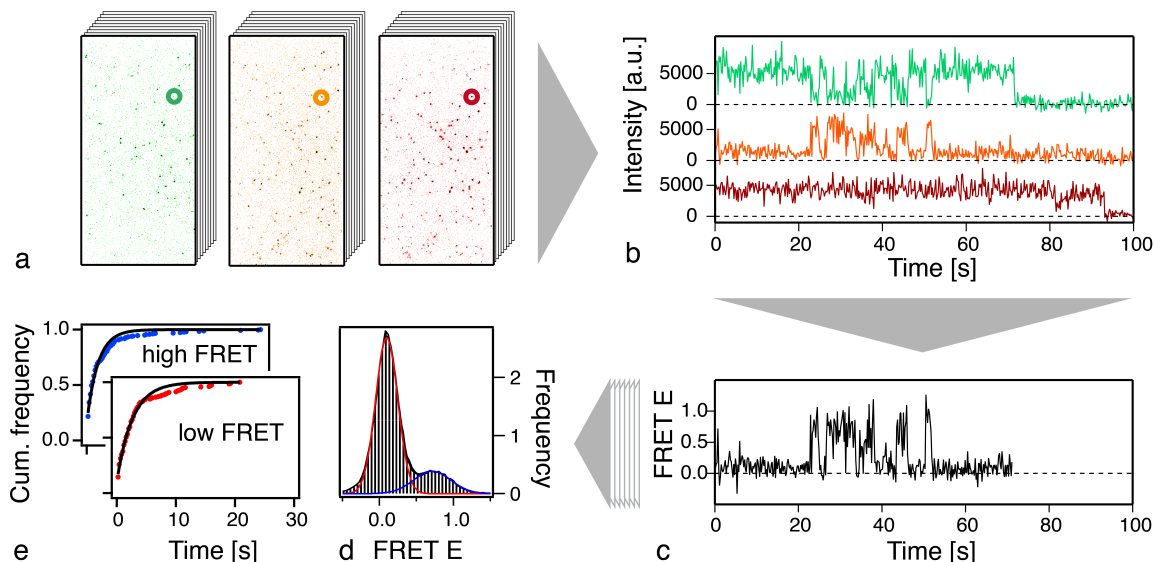


Figure 6.6: From raw data to results. (a) Raw data consists of a stack of fluorescence images for each channel: DD green, DA orange, AA red. The position of one particular molecule is indicated by circles. (b) Three fluorescence time traces are extracted for each FRET pair; colors as in (a). Discrete intensity levels and one sharp bleach step are characteristic for single fluorophores. (c) Corrections for experimental shortcomings are required to obtain accurate FRET efficiency time traces (see Section 6.4.1). (d) Multiple trajectories are accumulated in FRET efficiency histograms. Gaussian fits to the low/high FRET population are shown in red/blue, respectively. (e) Dwell times in distinct states are compiled in cumulative histograms, which provide kinetic information (see Section 6.4.2); colors as in (e), single-exponential fits in black.

Consequently, 3 time traces are obtained for every spot (Figure 6.6b): donor fluorescence after green excitation (DD), acceptor fluorescence after green excitation (DA) and acceptor fluorescence after red excitation (AA). An in-house Igor script is used to extract these. Corresponding x- and y-positions in all channels are resolved based on an image calibration obtained with bright fluorescent beads (Invitrogen). Bead positions are determined by Gaussian fits. The x- and y-offsets between both channels are fit with a third order polynomial. Based on that, positions in all channels are interconvertible.

Among such time traces, single FRET pairs are characterized by flat plateaus in all fluorescence channels and single step bleaching. Only conforming traces before bleaching are considered below.

6.4.1 Accurate FRET

The background intensity is removed from the raw fluorescence trajectories by subtracting the mean trajectory of the darkest hundred spots of a given movie.

To correct for varying ratios of green and red excitation intensities across the field of view, intensity profiles (prof) of both lasers are determined. The normalized average of a set of images of a dye-saturated surface serves as an intensity map. Most conveniently, the position-dependent correction is applied to the directly excited acceptor signal N_{AA} :

$$N_{AA}^{\text{prof}}(x, y) = N_{AA}(x, y) \cdot \frac{I_D(x', y')}{I_A(x, y)}$$

where $I_{D,A}(x, y)$ represent the respective, normalized intensities of the green or red laser at the position x, y , or the *converted* position x', y' .

Next, the data is successively corrected for 4 experimental cross-talk terms:

- leakage of donor photons into the acceptor channel
- direct excitation of the acceptor dye by the green laser
- different spectral sensitivity and different quantum yields of the fluorophores
- different laser intensities and different excitation efficiencies of the fluorophores

An elegant way to correct for all of these was developed by the Weiss lab [89]. It employs a 2D plot of the stoichiometry (S) vs. FRET efficiency (E) as shown in [Figure 6.7](#), with the *apparent* quantities:

$$S^{\text{app}} = \frac{N_{DD} + N_{DA}}{N_{DD} + N_{DA} + N_{AA}^{\text{prof}}}$$

$$E^{\text{app}} = \frac{N_{DA}}{N_{DD} + N_{DA}}$$

given by N_{ij} , the detected signals of the 3 time traces specified above. After the corrections below, this 2D plot separates the FRET population centered at $S = 0.5$ from the donor-only population ($S = 1, E = 0$) and the acceptor-only population ($S = 0$).

Leakage and direct excitation are corrected by respective correction factors l and d :

$$N_{DA}^{\text{corr}} = N_{DA} - N_{DD} \cdot l - N_{AA}^{\text{prof}} \cdot d$$

l is determined from a donor-only sample, such that the donor-only population is located at $E' = 0$. Analogously, d is determined from an acceptor-only sample, such that the stretched acceptor-only population is centered around $S' = 0$.

The last two points in the list are corrected by γ and β , respectively:

$$N_{DD}^{\text{corr}} = N_{DD} \cdot \gamma$$

$$N_{AA}^{\text{corr}} = N_{AA}^{\text{prof}} / \beta$$

These factors are obtained from a linear fit (slope α , y-intercept b) to the average values of $1/\langle S \rangle$ vs. $\langle E \rangle$ of different FRET populations:

$$\frac{1}{\langle S \rangle} = \alpha \cdot \langle E \rangle + b$$

$$\beta = \alpha + b - 1$$

$$\gamma = \frac{\alpha - 1}{\alpha + b - 1}$$

This is only feasible if at least two FRET populations exist that are well separated in E .

Finally, the corrected stoichiometry and FRET efficiency are:

$$S = \frac{N_{DD}^{\text{corr}} + N_{DA}^{\text{corr}}}{N_{DD}^{\text{corr}} + N_{DA}^{\text{corr}} + N_{AA}^{\text{corr}}}$$

$$E = \frac{N_{DA}^{\text{corr}}}{N_{DA}^{\text{corr}} + N_{DD}^{\text{corr}}}$$

1D FRET efficiency histograms are then obtained as the corresponding additive projection of data with $0.3 < S < 0.7$.

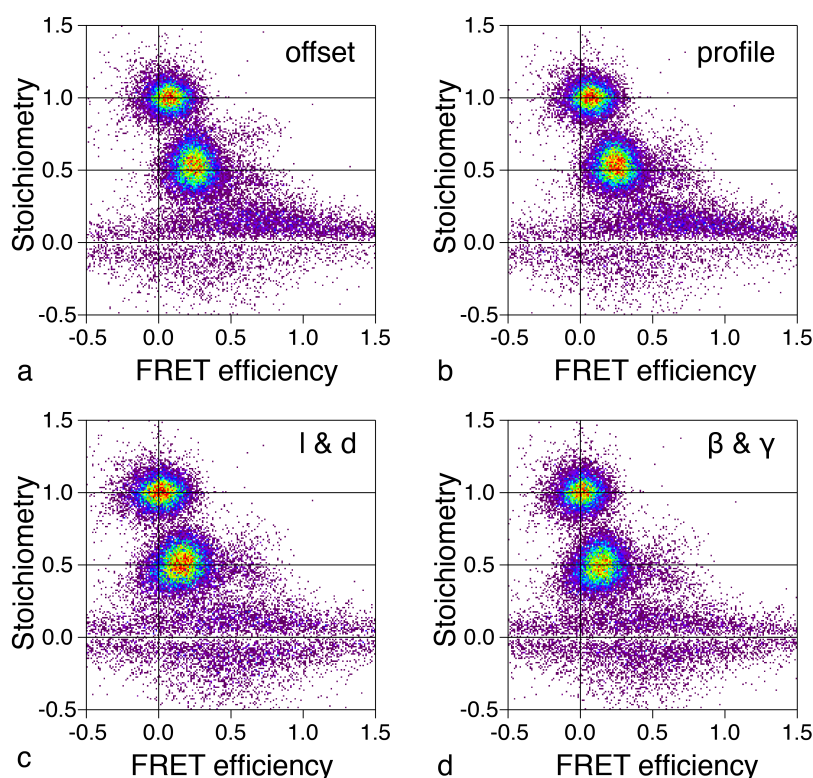


Figure 6.7: SE plots of stepwise smFRET correction. Example data obtained using a dsDNA sample with an inter-dye distance of 23 bps. (a) Apparent stoichiometry vs. FRET efficiency of 186 offset-corrected trajectories. (b) The effect of excitation intensity profile correction. (c) Subtraction of leakage $l = 0.066$ and direct excitation $d = 0.065$ shifts the donor-only population to $E = 0$ and the acceptor-only population to $S = 0$, respectively. (d) Finally the corrected FRET efficiency $E = 0.14$ is obtained by applying $\beta = 0.85$ and $\gamma = 1.14$.

Instead of this *global* γ -correction, some labs prefer a trace-wise, *local* γ -correction [139]. This approach is only applicable to time traces, which show acceptor bleaching *before* donor bleaching. Each individual γ is then calculated from the acceptor and donor signals before (pre) and after (post) acceptor bleaching:

$$\gamma_{\text{local}} = \frac{N_{DA}^{\text{pre}} - N_{DA}^{\text{post}}}{N_{DD}^{\text{post}} - N_{DD}^{\text{pre}}}$$

FRET efficiency histograms, as shown in [Figure 6.6d](#), reveal the relative population of distinct conformations within the data set. Such steady-state distributions can not be obtained from ensemble experiments. In addition, specific inter-dye distances can be calculated. Using Equation (3.7), the peak positions in [Figure 6.6d](#) convert into 92Å and 53Å.

The correction procedure is evaluated in [Section 8.2](#) together with the distance resolution.

6.4.2 The Classical Kinetic Analysis

Traditionally, kinetic information is gained from frequency analysis of dwell times in distinct conformations. As introduced in [Chapter 5](#), mathematical models (such as HMMs together with the Viterbi algorithm) are usually utilized to extract dwell times from smFRET trajectories.

Dwell times are then compiled into cumulative histograms as shown in [Figure 6.6e](#). In contrast to conventional histograms, these represent *integrated* transition probability densities, which are less susceptible to bias introduced by discrete time binning. In the ideal case, where every kinetic state can be resolved experimentally, a single-exponential fit provides the total off-rate out of a given state:

$$P(t) = 1 - A \cdot e^{-k_{\text{off}}t}$$

Correct contributions are achieved by weighting each data point with the square-root of its frequency count.

[Figure 6.6e](#) shows a clear deviation from a single-exponential function. Thus, the above stated assumption is not generally applicable, which is further discussed in [Section 8.3](#).

AN IDEAL PROTEIN CONSTRUCT FOR SMTIRF

To track protein conformational changes using smFRET over seconds to minutes, there are three main requirements: immobilization, site-specific fluorescent labeling, and - if a complex is to be studied - high affinity. At the same time, the optimal protein construct is as close as possible to the native protein. An Hsp90 construct that complies with all of these requirements is shown in Figure 7.1.

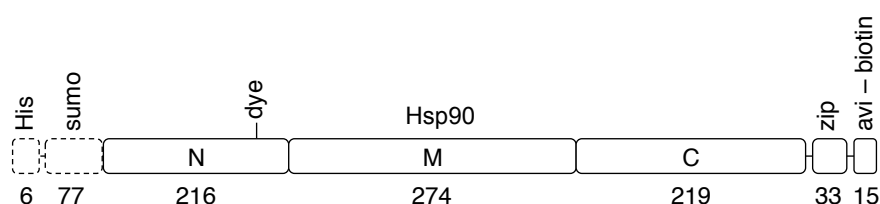


Figure 7.1: Hsp90 construct for smTIRF measurements. The N-terminal His-tag and SUMO-domain (dashed) are cleaved away during purification. The final, tag-free construct consists of the 3 Hsp90 domains, N-terminal (N), middle (M) and C-terminal (C), together with a C-terminal zipper region (zip) for high dimerization affinity and an AviTag (avi) enabling site-specific *in vivo* biotinylation. It is site-specifically labeled with a fluorescent dye. The number of amino acids per segment are stated below.

7.1 SITE-SPECIFIC FLUORESCENT LABELING

A widely used strategy for the attachment of FRET donor and acceptor dyes is thiol-reactive maleimide coupling. This technique is only site-specific if the protein under study is deficient of additional, solvent accessible, native cysteins. For Hsp90 this is the case. Ergo, a non-native cystein is readily introduced by site-specific mutagenesis (QuickChange Lightning Mutagenesis, Agilent). Otherwise, artificial amino acids can be used to achieve site-specificity [153, 159].

In general, flexible loops are the preferred dye attachment sites, because there is a good chance that the cystein point mutation and the coupled organic dye molecule do not interfere with protein function. These positions are also preferred from photo-physical perspectives, because they allow the fluorophore to rotate freely and sample all possible orientations, which leads to cleanest signals due to sufficient orientational averaging, on the one hand, and minimal collisional quenching, on the other hand. In contrast, dye sticking to hydrophobic patches can introduce distinct intensity levels, which complicates data interpretation.

Finally, conformational changes are best resolved by FRET if they change the inter-dye distance from 2 to 8 nm, which matches the most distance-sensitive FRET range. Atto550 and Atto647N are the preferred fluorophores in this work because of their brightness and comparatively favorable photostability even in the absence of additional photo-stabilizers. Thiol-reactive coupling was performed according to Atto-tec's protocol.

7.2 IMMOBILIZATION

The most common surface immobilization technique makes use of biotin streptavidin binding, which is the natural complex with highest affinity known today ($K_D = 10^{-15} \text{M}$ [21]). Since, in this work, thiol-reactive coupling is reserved for site-specific fluorescent labeling, a different attachment mechanism is needed for biotin conjugation. Three biotin-related immobilization strategies were examined: unspecific N-Hydroxysuccinimide (NHS)-coupling, vesicle encapsulation and site-specific *in vivo* biotinylation. In either case, Neutraavidin-coated surfaces were used (cf. Section 6.2).

Unspecific amine-reactive NHS-coupling led to very low yields. Thus comparatively high concentrations were needed in TIRF measurements causing considerable unspecific binding. It is further unfavorable, because of the 86 lysins contained in yeast Hsp90 (see Figure 7.2). Also arginines (e.g. Arg380, which is essential for ATP hydrolysis) are potentially attacked by NHS. Consequently, amine-reactive coupling has a wide-ranging and unpredictable impact on Hsp90.

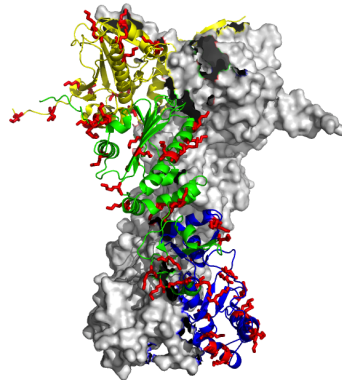


Figure 7.2: Hsp90 crystal structure [2] with highlighted lysins (red). Each protomer contains 86 lysins. One protomer is shown in cartoon representation (yellow, green, blue for N, middle, C domain), the other as gray Van der Waals surface.

In contrast, vesicle encapsulation works without modification of the protein. Unfortunately, organic fluorophores are inherently hydrophobic and especially the rhodamine derivatives Atto550 and Atto647N were found to interact significantly with lipid bilayers [70]. In agreement with these findings, smTIRF experiments using (15:0)-PC vesicles including 1% 16:0 Biotinyl Cap PE (both Avanti Lipids) for surface attachment resulted in unusable, messy FRET traces.

The optimum between minimal interference and maximum specificity was achieved by enzymatic *in vivo* biotinylation at the very C-terminus of the construct. In this way, the zipper serves as a linker towards the PEG brush, which provides Hsp90 with additional degrees of freedom and maximum solvent exposure - even in the immobilized state.

7.2.1 Site-Specific *in vivo* Biotinylation

For this purpose, we exploited *Escherichia coli*'s biotin ligase BirA, which efficiently biotinylates a specific lysin residue in a 15 amino acid sequence known as AviTag [13]. This tag was genetically inserted at the C-terminus of the construct using Agilent's QuickChange Lightning Mutagenesis kit.

In vivo biotinylation is performed in one step during target protein expression: BirA was co-expressed using Avidity's low copy-number plasmid, pBirAcm. To this end, pBirAcm (with chloramphenicol resistance) was purified from the CVB101 strain (Avidity) and transformed into BL21 star (Invitrogen). This was necessary because the CVB strain lacks a T7 polymerase, which is required for Hsp90 expression using the pET-28b vector. See [Section B.1.2](#) for the detailed protocol.

The efficiency of *in vivo* biotinylation and the resulting high affinity of the Hsp90 conjugate for Neutravidin is visible in smTIRF experiments: the sample concentration required for sufficient surface coverage was significantly lower than with any other procedure. In fact, it matched the one observed for synthesized biotinylated DNA constructs.

7.3 HIGH AFFINITY COMPLEXES

Detection of sm fluorescence requires low, i.e. pico-molar sample concentrations. At such low concentrations dissociation dominates and protein complexes fall apart. To overcome this problem, we exploit the intrinsically high affinity of a foreign coiled coil motif of the kinesin neck linker of *Drosophila melanogaster*. Introduced at the C-terminus of Hsp90 [128], this zipper region keeps both Hsp90 protomers in close proximity [109]. In a previous study, this zipper did not interfere with Hsp90's *in vivo* function [161].

Part III

RESULTS & DISCUSSION

EXPERIMENTAL POTENTIALS AND LIMITS

8.1 THE FUNDAMENTAL TRIANGLE IN SINGLE MOLECULE FLUORESCENCE

The experimental detection of single molecule fluorescence (smFluo) time traces is complicated by the antagonistic relation between three key figures, as illustrated in [Figure 8.1](#). At the core of this "vicious circle" lies the finite number of photons an individual fluorophore can emit - typically a few million photons [130, 167] - before it undergoes irreversible photo-bleaching.

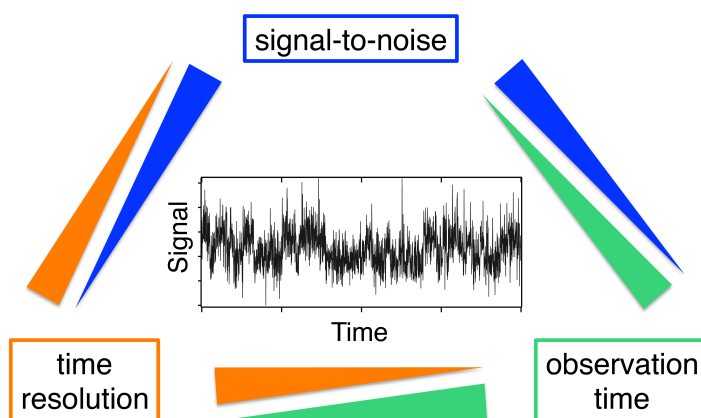


Figure 8.1: The triangle of fundamental limits of smFluo time traces. Signal-to-noise ratio, time resolution and observation time are interrelated in an antagonistic manner.

An excellent signal-to-noise ratio (SNR) - although itself desirable - requires a comparatively high excitation power. This comes with faster photo-bleaching and, thus, a reduced observation time for a given fluorophore. Likewise, high time resolution - i.e. a fast sampling rate - needs even higher excitation powers to reach an equivalent SNR at shorter exposure times.

The illustrative derivation in [Section A.1](#) suggests how to best spend the costly photons in TIRF experiments. Within the regime of realistic experiments, a simple relation between observation time τ_{bl} and SNR is found:

$$\tau_{bl} = \frac{\text{const.}}{\text{SNR}^2}$$

It holds regardless of the specific time resolution, i.e. sampling rate, of the experiment. A useful SNR of ~ 3 comes with $\tau_{bl} = 150$ frames in an ALEX experiment as detailed in [Chapter 6](#). This yields $\text{const.} = 1350$, which is plotted in [Figure 8.2](#).

In contrast to distance determination experiments (see [Section 8.2](#)), where a high signal to noise ratio is the only goal, *kinetic* analysis also requires a large

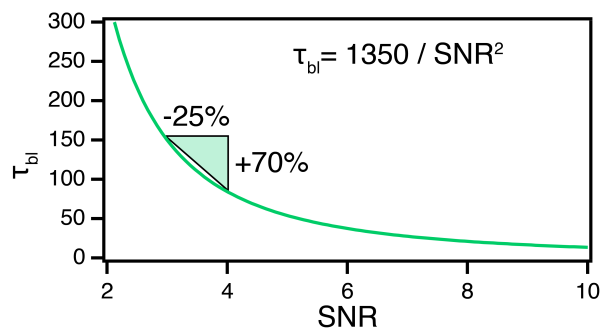


Figure 8.2: The fundamental relation of observation time (τ_{b1}) and signal-to-noise ratio derived from the experiment. A reduction of 25% in SNR results in 70% longer observation time.

enough τ_{b1} for the detection of possibly complex dynamics (e.g. kinetically heterogeneous behavior). [Figure 8.2](#) shows that sacrificing SNR to a certain extent yields a disproportionately high observation time, τ_{b1} , thus increasing the gain in kinetic information.

In general, the maximum detection bandwidth achieved in smFluo time traces is still remarkably low - even among single molecule techniques. Typically, for all-protein systems, the detection bandwidth spans less than a factor of 200 at a reasonable signal to noise ratio.

While enzymatic anti-bleaching agents largely increase the observation time of DNA-based samples [156, 1, 127, 33], their effect on the protein-coupled rhodamine derivatives used herein (Atto550, Atto647N) is negligible. Moreover, it is *a priori* unclear how the investigated protein function is affected by such additional protein components.

Therefore, alternative - *theoretical* - ways were developed to deal with these experimental limits and to acquire maximal information from the experiment (see [Chapter 9](#)).

8.2 THE DISTANCE RESOLUTION OF SMFRET

smFRET is frequently nicknamed *molecular ruler*. But how accurate is it really in determining nanometer distances? This question was addressed in a blind study using six test samples including two different FRET pairs and three dye separations.

dsDNA oligos (38 bps, purchased from IBA GmbH) served as a stiff scaffold for fluorophore attachment at tunable, yet well-defined separations: samples 1a,b,c contained Atto550 as FRET donor and Atto647N as acceptor at opposite strands, separated by 23, 15 or 11 bases, respectively. Samples 2a,b,c contained Atto550 and Alexa647 at the identical positions. A biotin was attached to the 5'-end of the acceptor strand. The inter-dye distances were quantified by TIRF experiments using ALEX¹ in TRIS buffer².

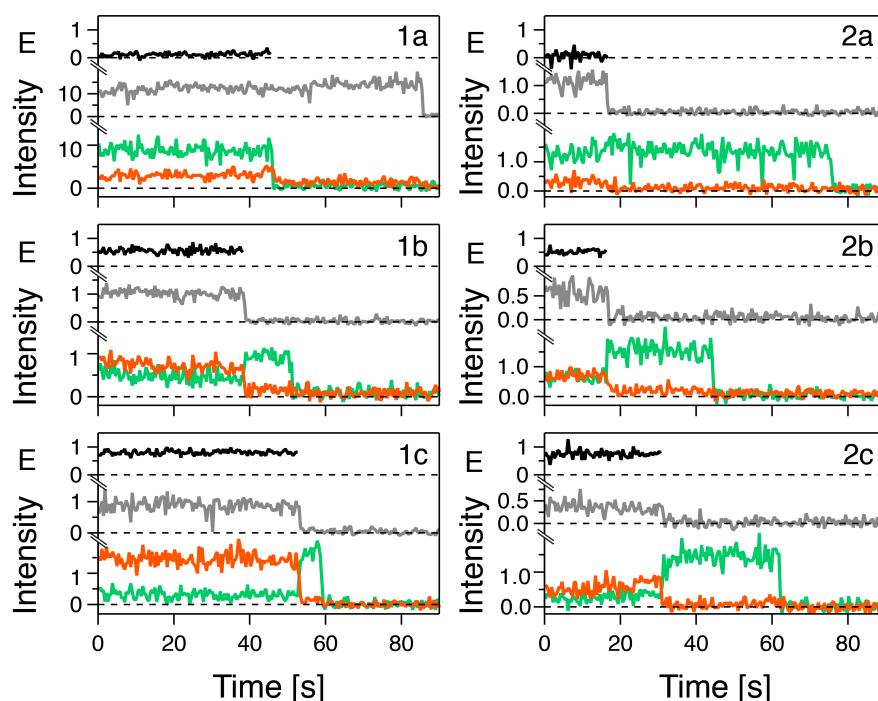


Figure 8.3: Representative time traces of the dsDNA samples, 1a,b,c and 2a,b,c, as indicated. FRET efficiency (E) is shown in black. The fluorescence intensity of the directly excited acceptor is shown in gray, the directly excited donor in green and the FRET sensitized acceptor in orange (in 10^4 EMCCD greyscale units).

Representative time traces for all samples are displayed in [Figure 8.3](#). They exhibit flat plateaus and instantaneous bleaching. Low, medium and higher FRET efficiencies are observed for samples a,b,c, respectively. The >10-fold increased bleach rate of Alexa647 compared to Atto647N led to severely decreased observation times for samples 2a,b,c. In contrast, for samples 1a,b,c, Atto550 bleaching is generally limiting. Specifically, the mean fluorophore lifetimes (for the lowest FRET efficiencies) were $\tau_{1a} = 47$ frames (9.4s), as compared to $\tau_{2a} = 15$ frames (3s).

¹ 200ms exposure time in each channel.

² 5mM TRIS, 5mM NaCl, 20mM MgCl₂ at pH7.5, degassed.

The FRET efficiency distributions (obtained according to [Section 6.4.1](#)) of around hundred molecules for each sample are shown in [Figure 8.4a,b](#) together with calculated distances. The latter were obtained by 3D model calculations accounting for the dye's restricted rotational and translational degrees of freedom (its reduced *accessible volume*) due to DNA coupling [42, 76]. Naturally, this procedure requires prior knowledge about the dye's attachment site.

Respective Förster radii were previously determined to $R_0(1) = (64 \pm 2) \text{Å}$ and $R_0(2) = (71 \pm 2) \text{Å}$ [62].

[Figure 8.4c,d](#) show the distance distributions of all samples. Importantly, their widths reflect the distance resolution of the measurement, rather than the much smaller distance fluctuations of the dsDNA. Theoretically both, efficiency and distance, are not exactly normally distributed - even in the absence of distance fluctuations. In the presence of un-correlated noise, such as shot-noise or auto-fluorescence noise, efficiencies are skewed towards the extremes (0 and 1). Whereas distances are always skewed towards the Förster radius (see [Section A.3](#)).

Nevertheless, experimental FRET efficiency histograms are well fit by Gaussian distributions. Therefore, concerning TIRF data, distances are most ac-

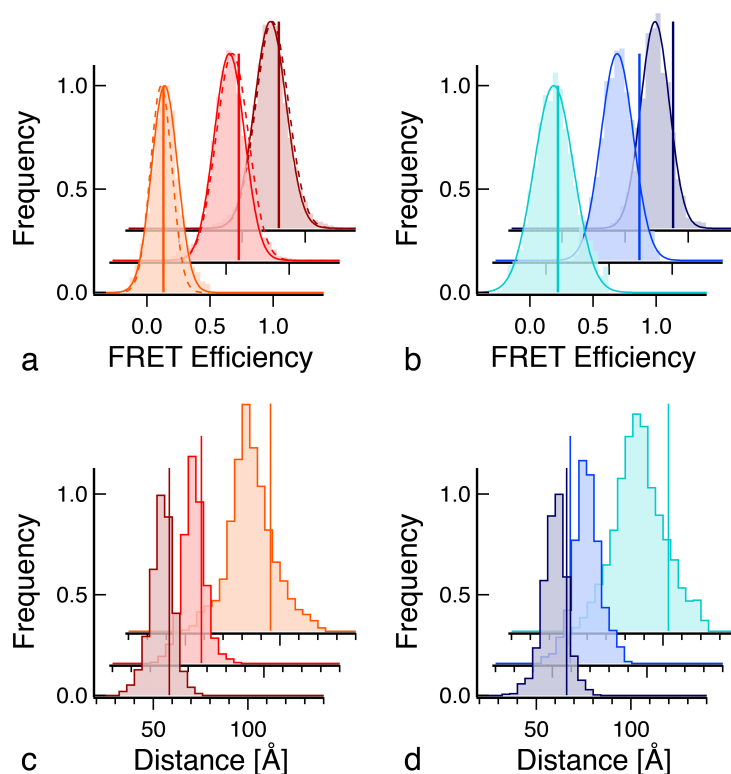


Figure 8.4: FRET efficiency (a, b) and distance distributions (c, d) measured for samples 1a,b,c (orange, red, dark red) and 2a,b,c (cyan, blue, dark blue). The result of global γ -correction is shown together with Gaussian fits thereof. Dashed lines in (a) show the corresponding fits after *local* γ -correction. The calculated values are displayed as vertical lines. Characteristic numbers are provided in [Table 8.1](#).

curately calculated as the center of a Gaussian fit to the FRET efficiency distributions. Deduced characteristic numbers are provided in [Table 8.1](#).

The FRET efficiencies resolved for samples 1a,b,c fit well with the calculated values - independent of global or local γ -correction (introduced in [Section 6.4.1](#)). The observed distance deviations, provided in [Table 8.1](#), range from 1 to 4Å. For samples 2a,b,c the deviations from the model distances are larger: 2 to 9Å (see below).

Table 8.1: smFRET results for 6 samples measured by TIRF with ALEX using global or local γ -correction, as specified. N: number of molecules; E: FRET efficiency; d: distance in Å. Calculated (calc) values were deduced from a 3D DNA model [42] by FPS [76]. Measured (meas) efficiencies E_{meas} are reported as Gauss positions. Corresponding distances were calculated using Equation (3.7) with $R_0(1a,b,c)=64\text{Å}$ and $R_0(2a,b,c)=71\text{Å}$, respectively [62].

Sample	Mode	N	E_{calc}	E_{meas}	d_{calc}	d_{meas}	Δd
1a	global	186	0.13	0.14	88	87	1
	local	84		0.11		91	3
1b	global	127	0.60	0.53	60	63	3
	local	77		0.55		62	2
1c	global	236	0.79	0.72	51	55	4
	local	163		0.74		54	3
2a	global	125	0.22	0.19	88	90	2
	local	91		0.24		86	2
2b	global	100	0.74	0.56	60	68	8
	local	98		0.63		65	5
2c	global	75	0.88	0.74	51	60	9

8.2.1 Local vs. Global γ

In theory, local and global γ -corrections should have the same result as perceived in [Figure 8.4a](#). However, it is important to note that γ is only a constant if leakage and direct excitation were removed beforehand (see [Section 6.4.1](#)). Otherwise mixed local γ 's are obtained that change with varying FRET efficiencies.

It was proposed previously [139, 108] that local γ -correction would be better suited to correct for inter-fluorophore heterogeneities observed at surfaces, and thus result in sharper FRET efficiency peaks. This general statement was not confirmed. In fact, local γ 's are determined as the ratio of roughly defined numbers, which leads to broad γ -distributions as shown in [Figure 8.5](#). If this distributions were caused by dye heterogeneity, they should be independent of FRET efficiency. Instead increased broadening is observed at low efficiencies. This indicates that the distributions are dominated by insufficient statistics rather than true fluorophore heterogeneity.

In addition, local γ correction is only applicable to the fraction of time traces showing acceptor bleaching *before* donor bleaching. Consequently, much data is dismissed. Due to the FRET efficiency dependence of bleaching,

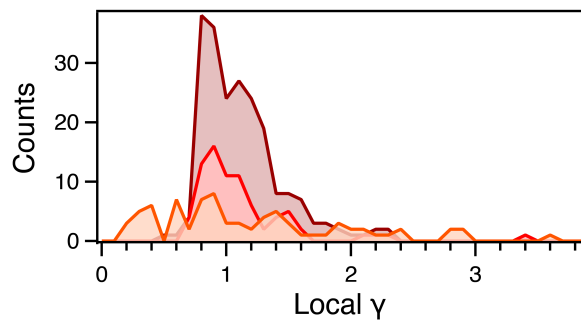


Figure 8.5: Distributions of local γ -values measured for samples 1a,b,c (orange, red, dark red). Especially at low FRET efficiency, very broad distributions result. The skewness is a result of the underlying ratio ($\Delta DA/\Delta DD$).

this effect is worst for low-FRET samples favoring donor bleaching, cf. respective trace counts in [Table 8.1](#).

In contrast, a global γ does usually not suffer from poor statistics. However, it relies on two sufficiently "similar" samples with well-separated FRET efficiencies, whereas local gammas are inherently self-sufficient.

Finally, the FRET efficiencies after local and global γ correction were similarly accurate for samples 1a,b,c. For samples showing low and high FRET efficiencies, such as proteins in an open and closed conformation, the less tedious global γ -correction is usually preferred. Whereas local γ 's are the only option in the absence of a *second* reference population.

8.2.2 Fluorophore-Specific Artifacts

The growing discrepancy of the measured vs. calculated distances of samples 2a,b,c ([Table 8.1](#)) with decreasing distances was reproducibly observed in a world-wide comparative study (see below). It has been attributed to an unfavorable photo-physical property of the acceptor dye, Alexa647; namely a significant, FRET efficiency dependent population of a dark state [62]. Consequently, the extinction coefficient of the acceptor (or similar its excitation efficiency) decreases at shorter distances, which in turn decreases the energy transfer rate. As a result, the overlap integral - and thus the Förster radius - is no longer a constant, but a function of the inter-dye distance.

This explains the growing differences between measured and calculated distances from 2a towards 2c. It further demonstrates that accurate distance determination relies on fluorophores that are well described by Förster's theory.

8.2.3 Results of a World-Wide Comparison

The results of one lab alone are clearly not enough to judge the accuracy of smFRET in general. Therefore, the above blind study was extended to more than 20 labs world-wide [D]. The resulting data collection permits unprecedented statements on the accuracy and universal reproducibility smFRET. It reveals not only the precision between labs, but also between different techniques, e.g. TIRF (surface immobilized molecules) and confocal spectroscopy (freely diffusing molecules). FRET efficiencies were derived from

fluorescence intensities in various ways, including ALEX and probability density analysis (PDA), and also from fluorescence lifetimes. In addition, 4 different FRET pairs were investigated: Atto550/Atto647N, Atto550/Alexa647, Alexa488/Atto647N, Alexa488/Alexa594, subsequently referred to as sample 1,2,3,4, respectively.

Figure 8.6 shows an overview of the results obtained for two inter-dye distances (23 and 15 base pairs (bps) at a double-stranded DNA (dsDNA) oligo, termed *a* and *b*, respectively) measured and calculated in various ways. Clusters of fluorescence intensity derived data (shown in color) are found for samples 1a,b and 2a,b, where enough statistics was acquired. In particular, the previously discussed deviation from the model for Atto550/Alexa647 (sample 2b) was reproducibly observed.

The collection of alternative approaches - splitting into PDA, lifetime and phasor data - spreads wider. But further statements are difficult based on the present data set.

Therefore, in the following, we focus on the best documented techniques (16 labs), which are conventional intensity-based smFRET using both, TIRF and confocal setups.

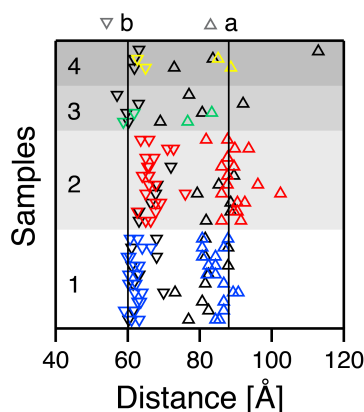


Figure 8.6: Results of a world-wide blind study on smFRET derived distances. Two distances (*a*, *b*) were measured using 4 FRET pairs (1-4). Conventional intensity-based data is colored according to the FRET pairs. Results of alternative techniques (PDA, fluorescence life-time, and phasor approach) are shown in black. The model distances are displayed as vertical black lines.

The FRET efficiencies measured by these techniques agree well with each other, as displayed in Figure 8.7. Efficiencies as low as 0.13 (sample 1a) were reproducibly resolved. This is remarkable since different correction procedures were applied.

Based on the current statistics, measurements without ALEX corrected with a global γ showed the largest deviations. Whereas local, mixed γ -correction led to the narrowest distribution, and additional ALEX information is especially useful for low FRET efficiencies.

Furthermore, TIRF experiments of samples 2a,b suffered from the aforementioned, unfavorably high bleach-rate of Alexa647. Nevertheless, nearly identical standard deviations are found using TIRF and confocal measurements. Average FRET efficiencies and standard deviations are reported in Table 8.2.

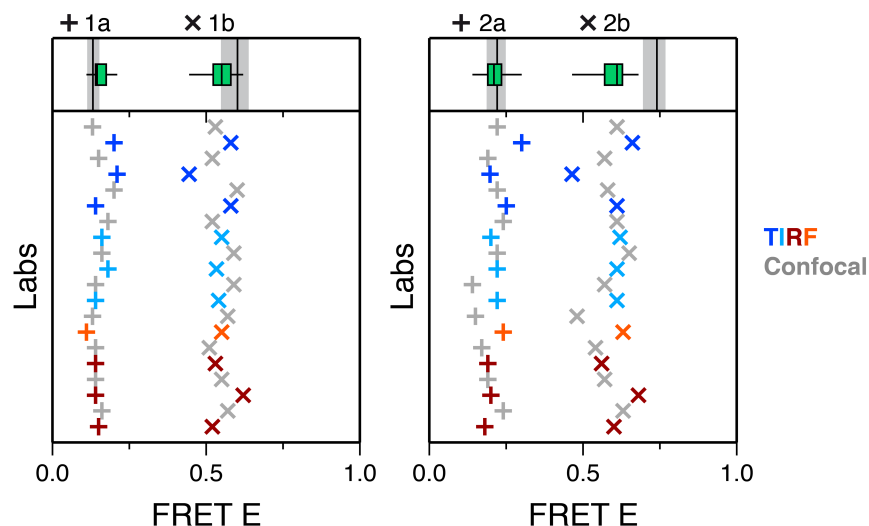


Figure 8.7: FRET efficiencies of samples 1a,b and 2a,b measured by intensity-based smFRET. Confocal data is shown in gray. TIRF data is colored according to the correction procedure: ALEX and global γ , dark red; ALEX and local γ , orange; no ALEX and local γ , light blue; no ALEX and global γ , dark blue. Box plots - including TIRF plus confocal data - are displayed for each sample (box: second and third quartiles; whiskers: minimum and maximum). Vertical black lines indicate the model efficiencies. Their uncertainty limits - due to uncertain Förster radii discussed below - are shown in gray.

For Atto550/Alexa647, a substantial deviation from the model efficiency is observed at shorter distances, i.e. sample 2b, but not 2a. As explained earlier, this was ascribed to a distance dependent dark state population. In contrast, for Atto550/Atto647N, the mean efficiencies lie closer to the expected range. Remaining deviations are discussed further in [Section 8.2.5](#).

Table 8.2: FRET efficiency results of the world-wide comparison on intensity-based smFRET. Standard deviations are rounded up.

$\mu \pm \sigma$	1a	1b	2a	2b
TIRF	0.16 ± 0.03	0.54 ± 0.05	0.22 ± 0.03	0.60 ± 0.06
Confocal	0.15 ± 0.03	0.55 ± 0.04	0.19 ± 0.05	0.57 ± 0.07
Total	0.15 ± 0.03	0.55 ± 0.05	0.20 ± 0.05	0.59 ± 0.07

8.2.4 The Current Distance Resolution Limit

Naturally, the overall accuracy of smFRET derived distances relies not only on the uncertainty of the experimental FRET efficiencies, but also on the uncertainty of the Förster radius itself. As shown in Equation (3.3), it is determined from the fluorescence quantum yield of the donor, the overlap integral, the orientational factor κ^2 and the refractive index. Although the former three quantities come with considerable experimental uncertainties, they contribute to the Förster radius with the sixth root only. Therefore, the uncertainty of the Förster radius can be estimated to 3% in the isotropic regime, i.e. assuming *sufficiently* mobile dyes that cause orientational av-

eraging (during the dwell in the excited state) such that $\langle \kappa^2 \rangle$ is close to $2/3$.

Consequently, the combined first-order distance uncertainty of smFRET results from the propagation of uncertainties (described by the standard deviations) of both, the Förster radius and the FRET efficiency:

$$\begin{aligned} \Delta r &= \sqrt{\left(\frac{\partial r(R_0, E)}{\partial R_0} \cdot \Delta R_0 \right)^2 + \left(\frac{\partial r(R_0, E)}{\partial E} \cdot \Delta E \right)^2} \\ &= \sqrt{\left(\frac{r}{R_0} \cdot \sigma(R_0) \right)^2 + \left(\frac{R_0}{6E^2} \left(\frac{1}{E} - 1 \right)^{-5/6} \cdot \sigma(E) \right)^2} \end{aligned}$$

Figure 8.8 shows the distance dependence of the first-order uncertainty for the common FRET pair Atto550/Atto647N, obtained using $\sigma(E) = 0.05$ and $\sigma(R_0) = 2\text{\AA}$. The maximal sensitivity is found in the vicinity of the Förster radius with below 5% distance uncertainty. Whereas away from R_0 , the uncertainty grows substantially. The specific distances and uncertainties are found in Table 8.3.

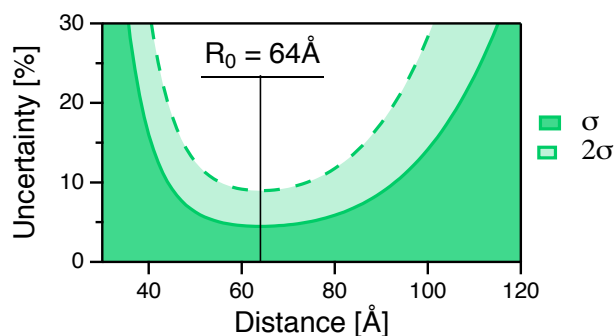


Figure 8.8: Total distance uncertainty of smFRET for the FRET pair Atto550/Atto647N. It incorporates the uncertainties of the Förster radius (R_0^{iso}) and the FRET efficiency as observed among 16 labs - either by TIRF or confocal spectroscopy. The uncertainties are displayed for 1 and 2 standard deviations (σ).

Table 8.3: smFRET derived distances and standard deviations compared to the model distances of the samples *a* and *b*.

distance [Å]	model	Atto550/Atto647N	Atto550/Alexa647
a	88	85 ± 7	90 ± 8
b	60	62 ± 3	67 ± 5

Importantly, these values are FRET pair specific, as shown in Figure 8.9a for a set of Förster radii. But in units of R_0 the whole set collapses to one *universal* benchmark. Although, individual precision may differ of course, Figure 8.9b represents a convenient estimate for the generalized accuracy of smFRET.

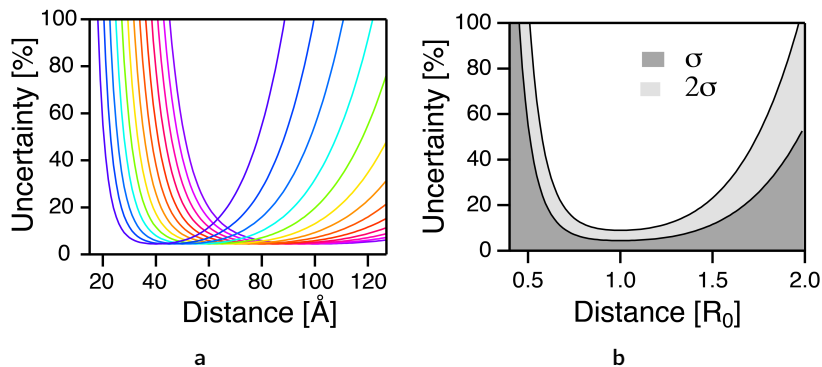


Figure 8.9: Universal distance uncertainty of smFRET. (a) Total distance uncertainty curves (1σ) for a wide range of Förster radii, $R_0 = 40$ to 100Å in blue to pink. (b) A generalized benchmark for smFRET accuracy in units of R_0 . (a, b) As in Figure 8.8, $\sigma(E) = 0.05$ and $\sigma(R_0^{\text{iso}}) = 3\%$.

8.2.5 Reproducible Model Deviations

The distances determined for samples 1a,b deviate from the model distances in *opposite* directions. A similar photo-physical effect as the one observed with Alexa647, can be excluded here, based on FCS data [62]. In contrast, a systematic bias of the correction procedure is more likely.

The significance of this trend is difficult to judge, because the accuracy of the model itself is of course unknown. But with respect to the mere distribution of determined distances, the deviation from the model values for 1a,b is statistically significant¹. Such a behavior - slight over-estimation of low efficiencies and growing under-estimation at higher efficiencies (see also sample 1c in Figure 8.4) - could be explained by biased corrections. Namely, incomplete background removal (e.g. due to superimposed exponential background bleaching), together with an over-estimated DD signal would provoke the observed trend. The latter could be caused by over-estimated γ values (cf. Figure A.6).

8.2.6 Further Discussion

To solve biological questions, one is usually not interested in inter-dye distances, but rather in the separation of bases, amino-acids or similar constituents. This information is not directly accessible by smFRET. But it can be inferred from knowledge about the local environment at the dye positions and the calculated accessible volumes of the dyes. Thereby, the accuracy depends on the previously available local structure information. Furthermore, it is considerably increased by using (self-consistent) distance networks between multiple dye positions [61].

To evaluate the accuracy of smFRET, an accurate reference model is key. Therefore, rigid dsDNA was chosen as a well characterized scaffold for fluorophore attachment. The utilized 3D modeling tool was shown to generate

¹ According to the Student t-test (two-sided, 95% confidence, neglecting non-normality) and also the non-parametric Wilcoxon Signed Rank test, which does not require normality (two-sided, 95% confidence).

accurate dsDNA structures that fit experimental x-ray diffraction results with (all atom) RMSDs below 1Å [93, 42]. In addition, the model distances were further refined by considering the accessible volumes of the dyes [76] and *not* their attachment points. All of this provides confidence in the model values. Yet, a finite inaccuracy remains in every model.

The distance resolution of smFRET was assessed in a world-wide blind study. Among 16 labs and diverse intensity-based techniques, a distance uncertainty of less than 5% was found near the Förster radius. But also very small FRET efficiencies below 0.15 were reproducibly resolved.

In addition, Alexa647 was found to deviate from classic Förster behavior, because of a superpositioned distance-dependent dark state population.

Furthermore, the study allowed to deduce a universal distance-dependent uncertainty function. It represents a convenient accuracy estimate, which is independent of specific dyes.

On the one hand, the reported uncertainty was achieved under optimal conditions using a very rigid and easily handled dsDNA structure. Whereas, general biological - protein - constructs may come with additional complication, such as dye sticking or inherent flexibility. On the other hand, very different methods were applied with potential bias in different directions. Therefore, the *precision* (or reproducibility) within one lab, one setup and one correction procedure may be considerably higher. Consequently, an even better (differential) distance resolution is expected within *one* lab.

8.3 KINETIC ACCURACY

Apart from static structural information, smFRET time traces enable one to study unsynchronized molecular dynamics experimentally. As one of very few techniques, TIRF can monitor in real-time how a single molecule progresses through states with distinct structural properties. That is why the technique has become very popular to investigate conformational changes in biomolecules.

Its potential and limits are demonstrated in the following using the example of a dynamic DNA construct, an all-protein system and simulations [B].

8.3.1 The Simple 2-State Model

Holliday-junctions [66] have become a widely used model system for conformational dynamics studied by smFRET. These DNA four-way junctions alternate constantly between two equilibrium conformations [101]. An example trace is shown in Figure 8.10a. As expected for a two-state system, the corresponding FRET efficiency histogram shows two peaks (Figure 8.10b). And the dwell-time histograms are well fit by single-exponentials (Figure 8.10c). In this case, the standard procedure for kinetic analysis, i.e. dwell-time analysis introduced in Section 6.4.2 is applicable.

The accuracy of such dwell time derived rates was confirmed by simulations of varied 2-state models with systematically growing rates (see Figure 8.11a).

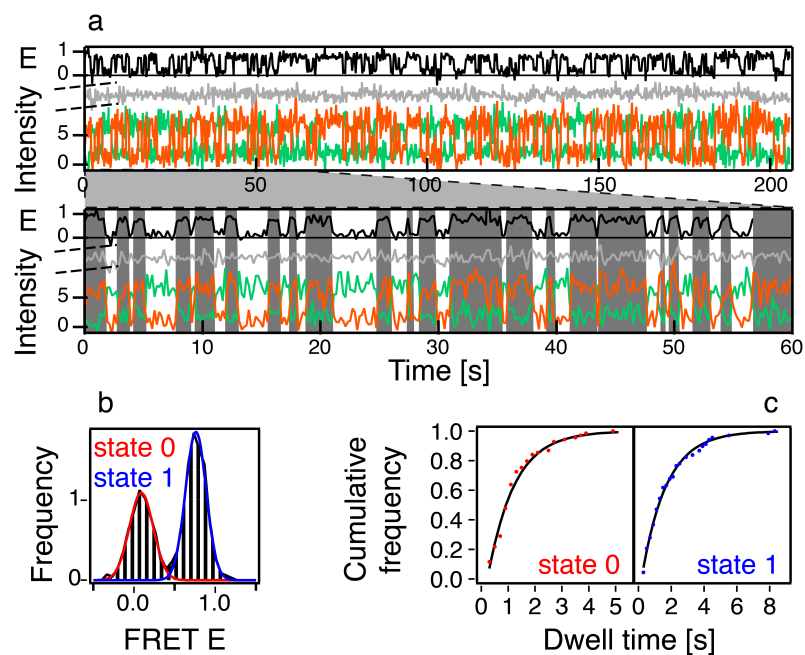


Figure 8.10: Kinetic smFRET data of a single Holliday junction revealing 70 transitions in one time trace. (a) FRET efficiency (E , black) and fluorescence trajectories (donor, green; acceptor, orange; directly excited acceptor, gray). The state allocation by HMM is shown in the zoom below (high FRET, gray; low FRET, white). (b) The FRET efficiency histogram shows two peaks. (c) The cumulative dwell-time histograms are well fit by single-exponential functions.

For a set of 200 simulated time traces, relative errors of 20% or less can be expected, as long as the rate of interest is 5 times slower than the sampling rate and at least 7 times faster than the bleach rate (see Figure 8.11b).

Notably, very similar numbers are found whether or not dwells *without* observed start and end points are considered (see Figure 8.11b,c). In the former case, even traces without an observed transition are considered as a dwell.

Even higher sampling rates - about 100 times the rate of interest - are needed to completely remove the non-zero offset of the asymptote in Figure 8.11c,d. Importantly, such high sampling rates are accessible in the experiment only at the cost of a faster bleach rate, as previously discussed in Section 8.1.

It turns out that every dwell time derived rate is systematically over-estimated, even for the simplest 2-state models.

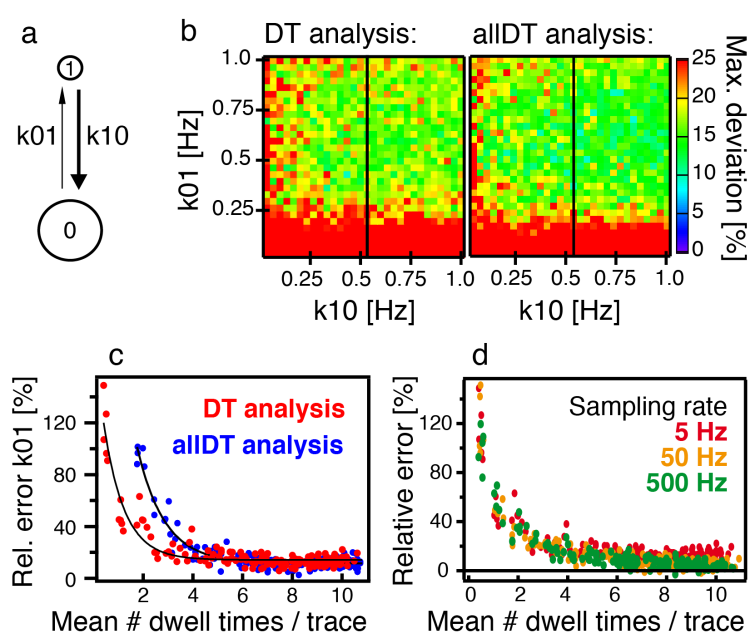


Figure 8.11: Accuracy of dwell-time analysis tested by simulations. (a) Discrete state sequences were simulated for 2-state models with different rates, k_{01} and k_{10} : 200 state sequences with 5Hz sampling rate and 0.03Hz bleach rate. (b) The deviation of the determined k_{01} from the input k_{01} as a function of both input rates (maximum relative deviation out of five simulations per data point). While "DT analysis" considers dwells with observed start and end points only, "allDT analysis" includes also dwells with one and zero observed limits (static traces). (c) Relative errors of the rates along the indicated lines are shown as a function of the mean number of dwell times per trace. Black lines serve as a guide to the eye. (d) The residual over-estimation of about 15% vanishes at higher sampling rates. These are accessible in the experiment only at the cost of not resolving the slower dwells due to photobleaching.

8.3.2 Kinetic Models for Realistic Proteins

In contrast to the simplistic 2-state system above, the situation is more complicated with realistic proteins, which usually adopt significantly more than two states [6]. As an example, Figure 8.12a shows experimental single protein time traces revealing conformational changes of Hsp90. The fluctuations between N-terminally open and closed conformations occur on a broad range of time-scales resulting in very long and short dwells, and generally fewer transitions per trace (here 3 on average). Also so-called *static traces* are found (Figure 8.12b), where zero transitions occur within the observation time.

Despite the two apparent populations in the FRET efficiency histogram (Figure 8.12c), both dwell-time distributions are multi-exponential (Figure 8.12d). Still, no systematical change in FRET efficiency from fast to slow dwells is observed (Figure 8.12e). Such behavior, hereafter referred to as *degenerate FRET efficiencies*, is indicative of *truly* hidden states that cannot be separated by FRET efficiency, but differ kinetically.

In this situation, dwell-time analysis is not applicable. The interpretation of the resulting multi-exponential dwell-time distributions may lead to erroneous conclusions. This is demonstrated using simulated, *synthetic* data (see example trace in Figure 8.13a) generated by the 4-state model in Figure 8.13b

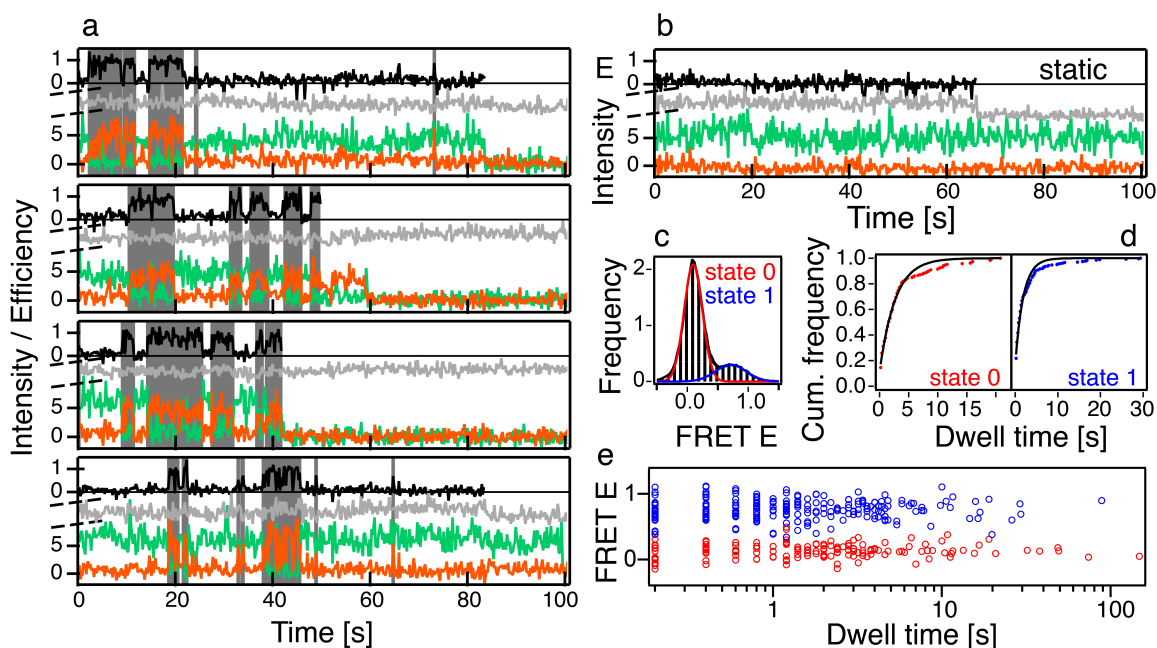


Figure 8.12: Conformational dynamics of Hsp90 resolved by smFRET. (a) Four example trajectories show dynamics on different timescales (FRET efficiency, E: black; fluorescence of the donor: green; acceptor: orange; directly excited acceptor: gray; Viterbi paths as gray and white overlays indicating high- and low-FRET states.). (b) No transition occurs within the observation time of this Hsp90 molecule, leading to "static" traces. (c) Two peaks are visible in the FRET efficiency histogram. (d) The resulting cumulative dwell-time histograms clearly deviate from respective single-exponential fits. (e) There is no trend in FRET efficiencies throughout the broad range of observed dwell times: 0.2s to >100s.

comprising two indistinguishable high-FRET and two indistinguishable low-FRET states, which are all 4 kinetically distinct. Figure 8.13c compares the results obtained from bi-exponential fits of the dwell-time distributions to the original 8 transition rates. Because the connectivity of the states is lost in such distributions, only half of the rates can be identified. Three of them differ by more than 100% (see Figure 8.13d). Moreover, the corresponding uncertainties of the fit do not reveal the true uncertainties of the rates.

In contrast, based on the *same* synthetic data, all 8 rates were accurately resolved by SMACKS, a new maximum likelihood approach introduced in Chapter 9. Notably, all rates come with meaningful error estimates (Figure 8.13c) and relative errors smaller than 50% (Figure 8.13d).

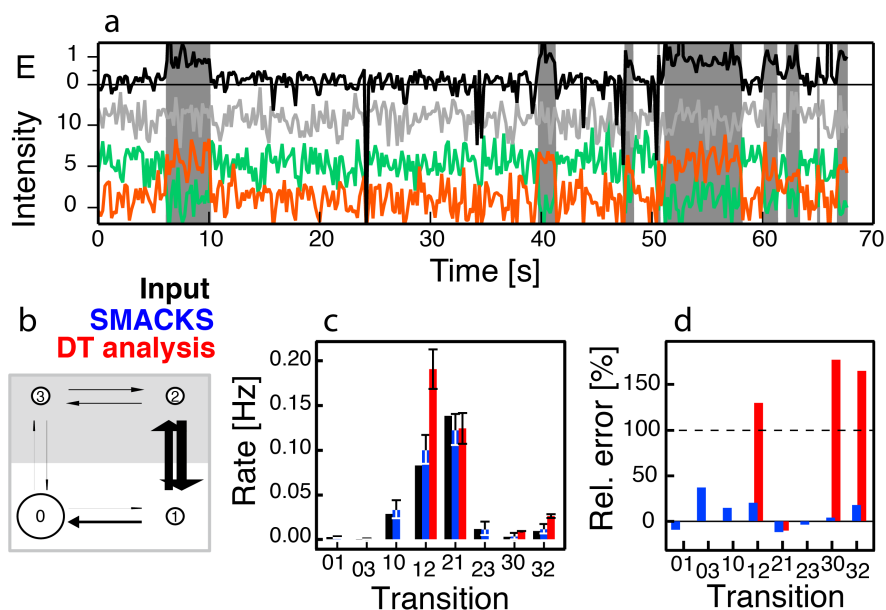


Figure 8.13: Evaluation of dwell-time analysis in the context of more realistic state models. (a) Synthetic example trace with FRET efficiency (E , in black) and fluorescence traces (donor, green; acceptor, orange; directly excited acceptor, gray). Synthetic data sets included 200 traces, generated by the 4-state model depicted in (b): states 0/1 as well as 2/3 share the same FRET efficiencies. See Section B.6.1 for details. The size of the circles in the state model is proportional to the state population. The arrow widths are proportional to the transition rates. (c,d) Comparison of dwell-time analysis (red) and SMACKS (blue, see text): (c) contrasting the resolved transition rates with the absolute input rates, or (d) contrasting the individual relative errors.

8.3.3 Further Discussion

The kinetic analysis of smFRET time traces is complicated by the exceptionally narrow detection bandwidth of the experiment. It is restricted by the exposure time, on the one side, and the mean observation time - limited by photo-bleaching - on the other side.

As a consequence, dwell-time analysis fails to resolve accurate rates - already in a two state system. These limitations have been recognized in the patch clamp field more than 20 years ago [67]. Nevertheless, it is still the standard

analysis in the smFRET field today. Therefore, taking the next step in the kinetic analysis of smFRET data is long overdue.

The solution to the challenge is presented in the next chapter. As demonstrated in [Figure 8.13](#), it provides increased accuracies and meaningful error estimates - *despite* the above experimental challenges associated with smFRET time traces.

8.4 SUMMARY 1

The photons a fluorophore can emit are *numbered* and as such very valuable to the smFRET experimenter. They can be spent *either* on signal-to-noise, time resolution *or* observation time. Thereby, it is the experimenters task to find the optimal balance between the three.

For instance, maximal distance resolution requires maximal signal-to-noise. For the first time, the distance resolution of smFRET was assessed in a world-wide blind study. An uncertainty of less than 5% was found among 16 labs for distances close to the Förster radius. A global benchmark was found for the resolution of smFRET. It allows to estimate the resolution of smFRET, independent of the specific FRET pair and over a wide range of distances.

Moreover, the precious photons can be spent on kinetic information. Classical dwell-time analysis is not only inaccurate in the simplest of cases (systematic over-estimation of 15% to >100%), in fact, it can lead to conceptually wrong conclusions. Instead, more efficient approaches are required to extract the information included in smFRET data.

QUANTITATIVE SINGLE MOLECULE KINETICS

In view of the experimental challenges detailed in the last chapter, a more suitable kinetic approach was developed and custom-tailored for smFRET. The goal was to quantify single molecule kinetics as effectively and precisely as possible. This approach, termed single molecule analysis for complex kinetic sequences (SMACKS) [B], is demonstrated below using the example of Hsp90.

9.1 INFERRING ONE GLOBAL KINETIC MODEL

The limited detection bandwidth is a major challenge for kinetic analysis of smFRET time traces. Additional complication arises from experimental signal variations between individual molecules. The approach introduced below solves these issues in two steps. In short, it combines trace-wise HMMs (subsequently referred to as *trace-by-trace HMM*) with a second *semi-ensemble HMM* optimization. While the first part is used to capture the heterogeneity between individual molecules, the second part provides one global kinetic state model for the entire data set.

9.1.1 Step 1: Trace-by-Trace HMM

An apparent state model is determined, from visual inspection of the time traces and the associated histogram. Using the example of Hsp90's N-terminal dynamics, an apparent 2-state model is expected from the time traces and the histogram in [Figure 8.12](#). This model is used in a first, conventional trace-wise HMM optimization:

As introduced in [Chapter 5](#), the model $\lambda(\pi, A, B)$ is iteratively rated by the forward-backward algorithm and optimized by the Baum-Welch algorithm until convergence to maximum likelihood. The Viterbi algorithm is used to compute the most probable state sequence for every trace given the previously trained model. These trained parameters are examined visually by comparing the resulting Viterbi path to the input data (e.g. in [Figure 9.1a](#)).

Please note that by searching for flat plateaus, HMM echoes a characteristic requirement for single-molecule fluorescence data. Therefore, traces that are not well described by the Viterbi path, are often sub-quality traces and as such sorted out. On the other hand, the apparent model must be revised if the HMMs fail repeatedly at good quality traces (with respect to signal-to-noise, signal regularity etc.).

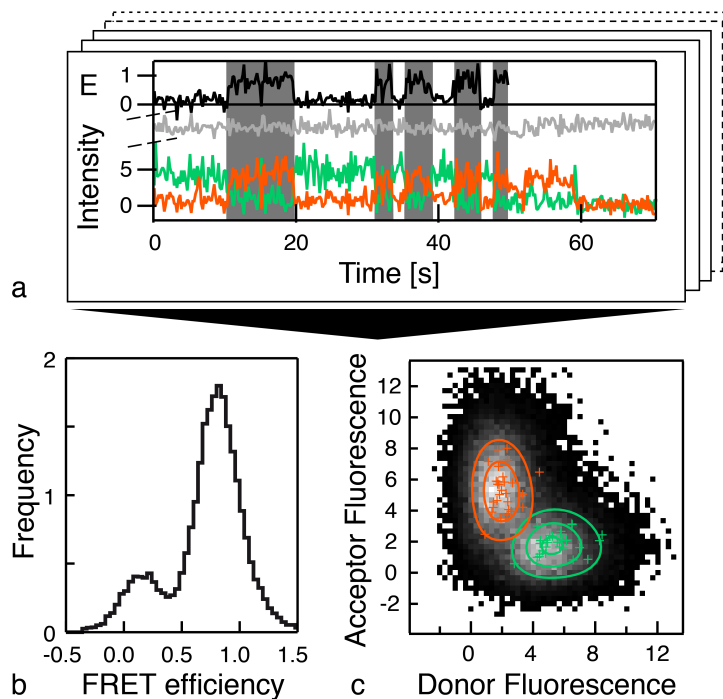


Figure 9.1: smFRET data as input for HMM. (a) Example trace with FRET efficiency, E: black; fluorescence of the donor: green; acceptor: orange; directly excited acceptor: gray; Viterbi paths as gray and white overlays indicating high- and low-FRET states, respectively. (b) The FRET efficiency histogram of multiple traces provides only 1D information, although 2D information was originally recorded. (c) 2D fluorescence histogram of smFRET data (black to light gray: minimal to maximal counts, white: no counts). The means of individual donor (green) or acceptor (orange) traces are shown by markers. Global Gaussians as derived for the entire data set are displayed as corresponding contours.

9.1.2 HMM Customization for smFRET

If applied to smFRET data, fluorescence time traces - not FRET efficiency traces - are the preferred input of semi-ensemble HMM.

By exploiting the original two observables - donor and acceptor fluorescence - instead of the FRET efficiency (only one observable), the robustness of the HMM with respect to uncorrelated noise is significantly increased (cf. [Figure 9.1b,c](#)). This is also exemplified in [Figure 9.2](#).

In addition, FRET efficiencies come with unfavorable spikes - due to occasional, noise induced division by zero - which are absent in the fluorescence traces. Therefore, no previous smoothing is required if fluorescence traces are used as HMM input.

Such fluorescence signals are appropriately described by 2D Gaussian PDFs, $b_i(\mu_i, V_i)$, per state i (see [Figure 9.1c](#)). These are parameterized by the vector of means, μ_i , and the covariance matrix, V_i , of the donor and acceptor intensities. A representative emission PDF is displayed in [Figure 9.3](#)(top, right).

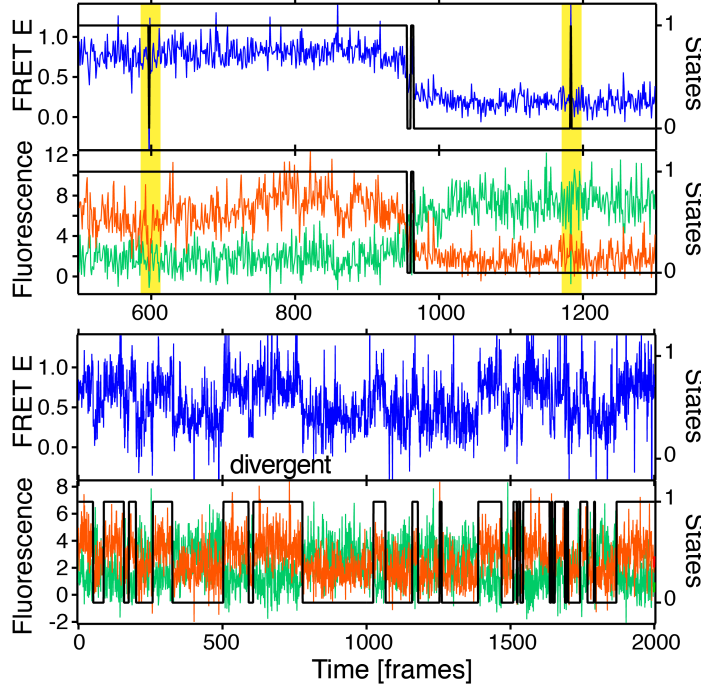


Figure 9.2: The superior robustness of 2D HMM demonstrated at two example traces. (top) Blink events (highlighted in yellow) are misinterpreted by FRET efficiency based 1D HMM. (bottom) 1D HMM diverges under high noise conditions. Ergo, the Viterbi path is not defined. In contrast, 2D HMM still derives a reasonable Viterbi path.

9.1.3 The FRET Constraint

After the standard corrections described in Section 6.4.1, the means of the donor and acceptor intensities, ${}^A\mu_i$ and ${}^D\mu_i$, must add up to the average total intensity of the respective trace:

$$\langle I_{\text{tot}} \rangle = \sum_{t=1}^T [{}^A x_t + {}^D x_t] / T = {}^A\mu_i + {}^D\mu_i = \text{const.} \quad \forall i$$

where ${}^A x_t$ and ${}^D x_t$ are the acceptor and donor intensities at time t , and T denotes the total time.

As a result, the available parameter space for the means, ${}^A\mu_i + {}^D\mu_i$, shrinks to one line. To cope with experimental variations between individual molecules, the line is determined individually for each trace. This *FRET line* is displayed in Figure 9.3(top, right).

This physical constraint is introduced into Baum's optimization formalism using Lagrange multipliers. Because the resulting update equations for Gaussian distributions are coupled in μ_i and V_i , I exploit the fact that the difference between Gaussian and Poissonian means is negligible for TIRF signals ($N \gg 10$ photons, cf. Section A.2). Therefore, the update equation for constrained Poissonian distributions [92] can be utilized to optimize μ_i :

$$\hat{\mu}_i = \langle I_{\text{tot}} \rangle \cdot \frac{\sum_{t=1}^T [\gamma_t(i) \mathbf{x}_t]}{\sum_{t=1}^T [\gamma_t(i) \cdot ({}^A x_t + {}^D x_t)]}$$

where \mathbf{x}_t is a 2D vector comprising the donor and acceptor signal at time t .

9.1.4 Step II: Semi-Ensemble HMM

To derive one kinetic model based on a set of traces, a semi-ensemble HMM run is performed. It makes use of the emission PDFs, previously trained by trace-by-trace HMM. To this end, the *global* start and transition probabilities are optimized, while the individual emission PDFs are held fixed as illustrated in Figure 9.3.

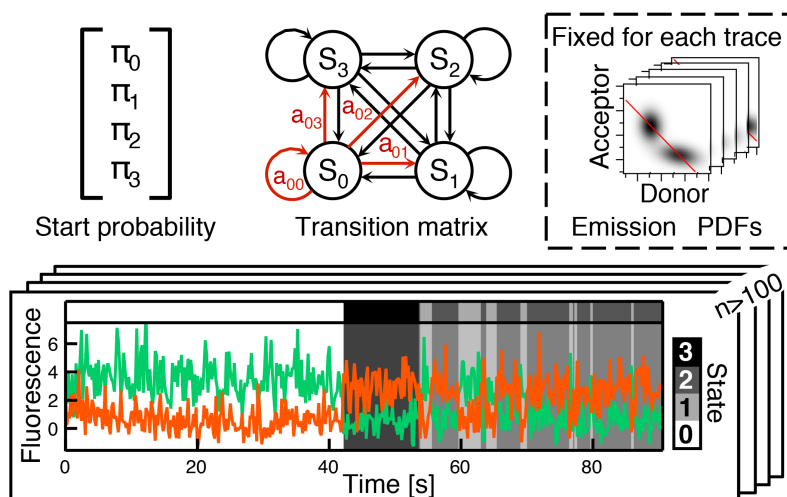


Figure 9.3: Semi-ensemble HMM optimizes a global kinetic model based on a complete data set (normally >100 traces). While the kinetic parameters - start probabilities and transition matrix - are optimized globally, the predetermined, individual emission PDFs are held fixed. This allows further to identify states not only by a characteristic signal, but also based on their kinetic behavior. See Section 9.2. For the example trace displayed, this results in a Viterbi path (overlays) with 4 kinetic states despite only 2 distinguishable FRET efficiencies.

The ensemble parameters Π_i , \mathcal{A}_{ij} (i.e. the global start and transition probabilities) are updated based on all N time-traces. Similar to their trace-wise counterparts, they are obtained using the γ -probabilities (cf. Section 5.2.2):

$$\hat{\Pi}_i = \frac{\sum_{n=1}^N [{}^n\pi_i]}{N}$$

$$\hat{\mathcal{A}}_{ij} = \frac{\sum_{n=1}^N \left[\sum_{t=1}^{T-1} [{}^n\gamma_t(i,j)] \right]}{\sum_{n=1}^N \left[\sum_{t=1}^{T-1} [{}^n\gamma_t(i)] \right]}$$

Dealing with "Static" Traces:

It is important to note that also static traces contain kinetic information. They occur in the experiment, as well as in theory, as a result of a limited observation time and disparate transition rates. Because they would not converge sensibly in a trace-by-trace run with more than one state, static traces are included using the mean emission PDFs of the remaining data set. Typical Hsp90 data sets contained about 30% static traces.

Convergence Criterion:

The likelihood function is not a convenient reporter for convergence, because it reaches very flat plateaus in between of step descents. By contrast, the

normalized changes of the diagonal entries of the transition matrix have proven useful for monitoring convergence of the HMM:

$$\text{Normalized Changes} = \sum_{i=0}^{n-1} \frac{|a_{ii} - a'_{ii}|}{a_{ii}}$$

where a'_{ii} are the diagonal matrix elements of the previous iteration and the sum goes over all states. In this work, no further changes were found, once this quantity fell below 10^{-8} .

Stationarity of the Input Data:

Any time-homogeneous Markovian analysis requires stationarity - but not thermodynamic equilibrium. This is easily confirmed by comparing the inferred start parameters to the (*left*) eigenvector of the transition matrix. Both represent alternate expressions for the steady-state populations. Alternatively, the results obtained from data reversed in time must agree with the original results to prove stationarity.

9.1.5 Further Discussion

One central problem of dwell-time based kinetic analysis was the over-estimation of rates due to the limited temporal detection bandwidth of the smFRET time traces (discussed in Section 8.1). Yet this is not inevitable. In fact, the issue is solved by normalizing the occurrence of a given transition by the total number of measured data points. Figure 9.4 shows the greatly improved accuracy of ensemble HMM derived rates in contrast to dwell time derived rates.

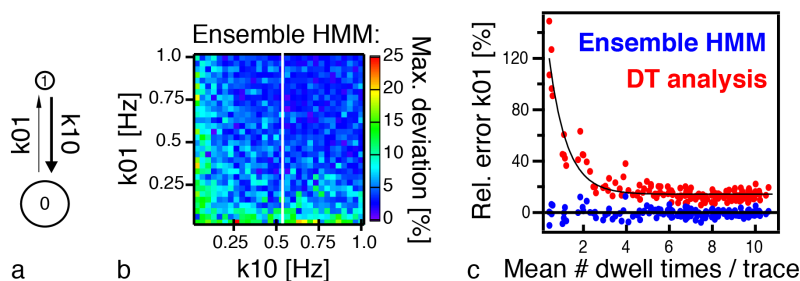


Figure 9.4: The accuracy of semi-ensemble HMM. (a) A 2-state model was simulated with varied rates, k_{01} and k_{10} (200 discrete state sequences with 5Hz sampling rate and 0.03Hz bleach rate). (b) Accuracy of the rates determined by semi-ensemble HMM presented as maximum relative deviation out of 5 data sets per specified rate input (k_{01} and k_{10}). (c) Comparison to dwell-time analysis (Figure 8.11) along the white line in (b) as a function of the mean number of (fully resolved) dwell times per trace. Black lines serve as a guide to the eye.

Surprisingly, although HMMs are nowadays routinely used by the smFRET community (for state allocation by the Viterbi algorithm), the *kinetic information* contained in the HMM - namely the transition matrix - is commonly ignored.

Indeed trace-wise HMMs would again suffer from short traces and the associated variation across the data set. In addition, those would come with a vast number of free parameters (i.e. degrees of freedom).

In contrast, the approach introduced herein integrates the flexibility against experimental variations between individual traces, on the one hand, with the ability to describe the complete data set by only one global kinetic model, on the other hand. As a consequence, the resolved rates are no longer systematically over-estimated.

In the current version (v1.3), SMACKS is entirely discrete in time. A straightforward adaption would be to consider continuous time for the derivation of transition *frequencies*. Those would follow from the matrix logarithm of the current transition matrix [145, 57].

SMACKS works without additional (hyper-) parameters or prior discretization, which contrasts with earlier published ensemble approaches [105, 24, 78, 15]. Moreover, this strategy works equally well for simulated and experimental data (see Section 9.3.1). The full procedure was tested on various synthetic data sets generated by known input models, in or out of equilibrium, with or without *degenerate FRET efficiencies* (see below). Example data can be found in Figure 8.13 and Section A.4.

Besides, apart from Section 9.1.2, the approach is applicable to all kinds of single molecule time traces. The source code of the described semi-ensemble HMM is available online as SMACKS tool¹. The manual, included in Appendix D, provides an overview of the functionalities.

¹ www.singlemolecule.uni-freiburg.de/smacks

9.2 DEALING WITH KINETIC HETEROGENEITY

Distinct kinetic states that cause experimentally indistinguishable signals represent another challenge to smFRET kinetics. Such kinetic heterogeneity is frequently observed with proteins [50, 164, 36, 63]. Using semi-ensemble HMM, kinetic heterogeneity can be investigated by comparing different state models including duplicates and triplicates of the apparent states. See [Figure 9.5](#) for illustrations of such models with increasing number of states.

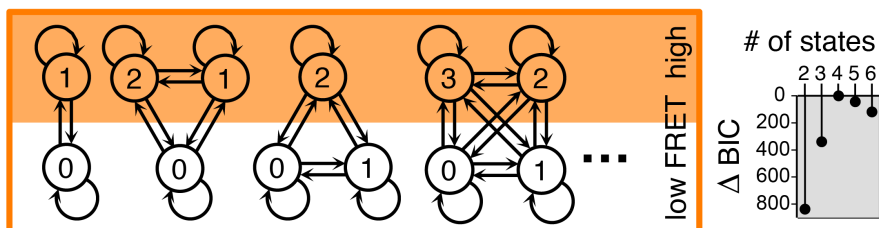


Figure 9.5: Model selection using BIC. Models including varied multipliers of the apparent states - here low FRET and high FRET - are compared based on a parsimony criterion. The model with the lowest BIC - here the 4-state model - represents the optimum between accurate description of the data and moderate complexity (i.e. degrees of freedom).

9.2.1 Model Selection

It is obvious that with an increasing number of degrees of freedom also the likelihood of the model increases. In the extreme case, a model could consist of one state per time step and thus describe the data perfectly - but without sensible meaning. Therefore, parsimony criteria are commonly used to identify the *optimal* model - that is to say, a model that describes the data well, at the same time keeping the model complexity moderate. Here the Bayesian information criterion (BIC) [141] is used for model selection, similar to earlier studies [102, 57, 92, 79]. It balances the likelihood, $\mathcal{L}(\lambda|\mathbf{O})$, against the number of free parameters, k , and n , the number of data points:

$$\text{BIC} = -2 \cdot \ln(\mathcal{L}) + k \cdot \ln(n)$$

[Figure 9.5](#) right compares models with 2 to 6 states with respect to ΔBIC , i.e. the difference to the lowest BIC value. The latter indicates the optimal model. For Hsp90's conformational dynamics, the optimal model consists of 4 states with 2 high FRET (closed) and 2 low FRET (open) states. This is consistent with the bi-exponential dwell time distributions discussed earlier in [Figure 8.12](#).

The applicability of BIC in this context could be confirmed using synthetic data (including noise and signal variations) of known input models (see examples in [Section A.4](#)).

9.2.2 Feature Selection

Once the optimal number of states is deduced, the model is further refined by inspecting the Viterbi paths.

The transition map ([Figure 9.6a](#)) relates the mean FRET values before and

after each transition. It is a common misconception that the transition map itself would report on the number of states in the model. This is clearly not the case, because it is the consequence of a *predetermined* model. Instead, it shows the quality of both, the original input data and the state allocation based on the inferred model. Conversely, the *lack* of clustering in FRET space indicates a poorly fitting model, causing inconsistent state allocation across the data set.

Kinetic heterogeneity leads to transitions *between* different FRET efficiencies, but also *within*, e.g. from low FRET to low FRET. But most transitions occur between the least populated (short-lived) states. For Hsp90 plus 2mM ATP, the two short-lived states comprise one low and one high FRET state.

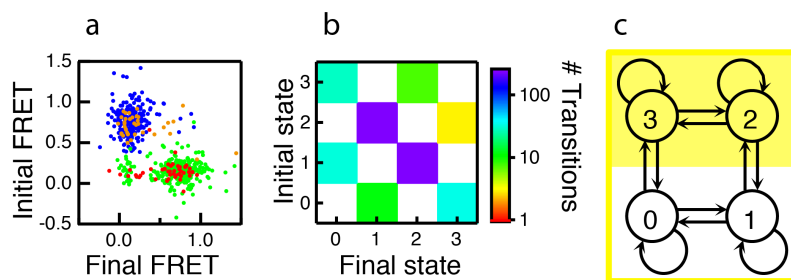


Figure 9.6: Model refinement. (a) The transition map relates the mean FRET values before and after each transition found by the Viterbi algorithm (initial states 0, 1, 2, and 3 in red, green, blue, and orange, respectively). (b) The transition histogram reveals the frequency of each transition in the data set. (c) Excluding transitions that do not occur leads to a cyclic model for Hsp90 + ATP.

This is also observed in the 2D histogram of all transitions in Figure 9.6b. Out of 12 possible transitions in a fully connected 4-state model, only 8 cyclic transitions are populated for Hsp90 with ATP. This equals the maximal number of theoretically identifiable transitions (see Section B.6.4). Despite the reduced number of free parameters, a cyclic 4-state model (Figure 9.6c) fits the data with equal likelihood as the complete 4-state model (with 6 links). Theoretically, a cyclic -o-c-o-c- model would fit the data equally well, yet the current picture of Hsp90 renders such a succession unlikely (discussed in Section 10.4.1).

For a system functioning at thermodynamic equilibrium, detailed balance requires that the transition histogram is symmetric about the main diagonal.

9.2.3 Further Discussion

In the conventional HMM framework, the model is optimized with respect to both, the observed signals *and* kinetic behavior. Inherently, the analysis of kinetic heterogeneity lacks the first criterion. Therefore lower accuracy is expected in the presence of indistinguishable signals - especially in view of the low temporal detection bandwidth of smFRET.

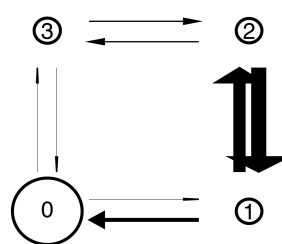
Nevertheless, SMACKS resolved accurate transition rates, in cases where neither dwell time derived rates nor uncertainty estimates were meaningful (cf. Table 9.1 as well as Figure 8.13).

Another initial concern was the *artificial* introduction of fake transition states. But this was not observed, either. The inferred states were meta-stable (i.e. the probability to remain was above 0.5) in the vast majority of cases.

Finally, the ability to separate states based on their kinetic behavior represents a significant improvement in the frequent case, where the experimental resolution or the studied reaction coordinate precludes the direct distinction of such states. As demonstrated in the next section, the inferred models reproduce experimental data remarkably well, which was impossible previously, by dwell-time analysis.

Table 9.1: SMACKS accurately detects kinetic heterogeneity. Simulated input rates are compared to output rates determined by SMACKS or dwell-time analysis based on synthetic data.

Rate [Hz]:	Input:	HMM:	DT:
0→1	0.0032	0.0029	–
1→0	0.029	0.0333	–
1→2	0.083	0.1002	0.1907
2→1	0.1385	0.1225	0.1244
2→3	0.012	0.0116	–
3→2	0.01	0.0118	–
3→0	0.0035	0.0036	0.0097
0→3	0.0007	0.001	0.0265



9.3 EVALUATION

In most previous kinetic studies on smFRET, the only reported error estimates were the uncertainties of fit coefficients from fitting dwell time distributions, disregarding systematic overestimation and variations throughout the data set. In contrast, here, three tests are proposed to assess the reliability of the results of the above procedure.

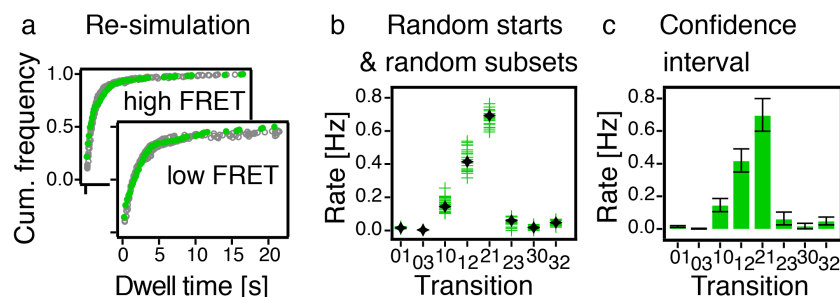


Figure 9.7: Three ways to critically evaluate the inferred model. (a) Dwell-time distributions are reproduced by re-simulating the model (experimental data, green; simulated data, gray). (b) Random start parameters uncover potential local likelihood maxima, and random subsets reveal data-set heterogeneity (subsets, green; complete set, black). (c) Confidence intervals measure the precision of the obtained rates considering the finite data set, experimental noise, and data-set heterogeneity (rates, green; confidence intervals, black).

9.3.1 Re-Simulation

The most illustrative test for the consistency of the trained model with the original data is “re-simulation” using the obtained transition matrix, the experimental bleach rate and degenerate states (here 2 low FRET, 2 high FRET). Figure 9.7a shows very good agreement between the re-simulated and the experimental dwell time distribution. Alternatively, FRET histograms could be re-simulated, too.

9.3.2 Randomization

Second, the convergence of the HMM to the global maximum is tested by using multiple random start parameters [112]. In all attempts, the parameters converged to the same maximum likelihood estimators (MLE). Additionally, random subsets of the data (here 66% of the traces) reveal the heterogeneity of the data set (Figure 9.7b). Here again all random subsets ($n > 50$) converged to the same model with normally distributed parameters (RMSD $\approx 30\%$ of the MLE).

9.3.3 Confidence Intervals

Third, the confidence interval of every trained parameter is calculated using likelihood ratio tests¹ (Figure 9.7c) [57, 55]. For each transition probability α_{ij} , the parameter space around the maximum likelihood estimator (MLE)

¹ Confidence intervals were implemented by Markus Götz.

is scanned while keeping the remaining parameters fixed at the MLE. The modified models λ' are compared to the MLE models λ_{MLE} by successive likelihood ratio (LR) tests:

$$\text{LR} = 2 \left(\ln[\mathcal{L}(\lambda_{\text{MLE}}|\mathbf{O})] - \ln[\mathcal{L}(\lambda'|\mathbf{O})] \right)$$

$$\mathbf{a}_{ij}^{\text{CB}} = \mathbf{a}'_{ij} \quad : \quad \text{LR} = \chi_{0.95, \text{df}=1}^2 = 3.841$$

The 95% confidence bound (CB) is reached where LR crosses the respective significance level for one degree of freedom (df). The confidence intervals report on the data set heterogeneity and the precision of the HMM.

9.3.4 Further Discussion

In summary, the accuracy and precision of the kinetic state model deduced by this semi-ensemble HMM approach was demonstrated by threefold evaluation: (i) direct comparison to the kinetic behavior in the experiment by re-simulation, (ii) consistency across the data set by subset comparison, and (iii) determination of confidence intervals revealing the precision of the model regarding experimental variations.

A reliable state model is necessary to take the next step and resolve kinetic and thermodynamic information from proteins in or out of equilibrium.

9.4 THERMODYNAMICS

Protein machines, such as Hsp90, use external energy (e.g. from ATP hydrolysis) and therefore operate out of equilibrium. A central question is where - in the conformational cycle - energy consumption couples into protein function.

9.4.1 Exploring energy coupling

Based on SMACKS, energy coupling can be investigated quantitatively. It boils down to determining the free energy difference over closed cycles [68, 65] (in units of thermal energy, kT):

$$\Delta G_{\text{cyc}} = - \sum_{\substack{\forall i \neq j \\ (\text{cycl.})}} \ln \left(\frac{a_{ij}}{a_{ji}} \right) \quad (9.1)$$

with a_{ij} , the transition rates between individual states i and j .

Clearly, the accuracy of the resolved ΔG_{cyc} depends on the size of the data set. Especially for systems away from equilibrium, very slow “reverse” rates can occur. Due to the finite data set, only few respective transitions are observed, resulting in large relative errors for these small rates. In this case, an alternative formulation of ΔG_{cyc} using the number of transitions N_{ij} found by the Viterbi algorithm was found to be more accurate.

$$\Delta G_{\text{cyc}} \approx - \sum_{\substack{\forall i \neq j \\ (\text{cycl.})}} \ln \left(\frac{N_{ij}}{N_{ji}} \right) \quad (9.2)$$

Equation (9.2) represents a lower bound for the Gibbs free energy, given the finite data set (zero transitions are set to one, to avoid poles). If all rates are well resolved, Equations (9.2) and (9.1) yield the same result, as demonstrated using the example of a 3-state model:

$$\begin{aligned} \Delta G_{\text{cyc}} &= - \sum_{\substack{\forall i \neq j \\ (\text{cycl.})}} \ln \left(\frac{N_{ij}}{N_{ji}} \right) \stackrel{3 \text{ states}}{=} - \ln \left(\frac{\pi_1 a_{12}}{\pi_2 a_{21}} \cdot \frac{\pi_2 a_{23}}{\pi_3 a_{32}} \cdot \frac{\pi_3 a_{31}}{\pi_1 a_{13}} \right) \\ &= - \sum_{\substack{\forall i \neq j \\ (\text{cycl.})}} \ln \left(\frac{a_{ij}}{a_{ji}} \right) \end{aligned}$$

9.4.2 Experimental limits

In the following, the ability to resolve free energy differences from single molecule time traces is discussed. To this end, two limit cases for the coupling of conformational changes to ATP hydrolysis are considered systematically. Assuming 1% ADP, 3mM Mg^{2+} , 250mM KCl and 100% efficiency, the energy released by ATP-to-ADP hydrolysis amounts to $\Delta G_{\text{cyc}} = 30kT$ [119]. In the first case (Figure 9.8a), the full 30kT are introduced within one step. Whereas in the second case (Figure 9.8b), the energy is successively released over 4 steps, as illustrated by the energy schemes. The latter is comparable to contributions by ATP binding, hydrolysis and ADP or P_i release, proposed e.g. for the human mitochondrial F_1 -ATPase [146].

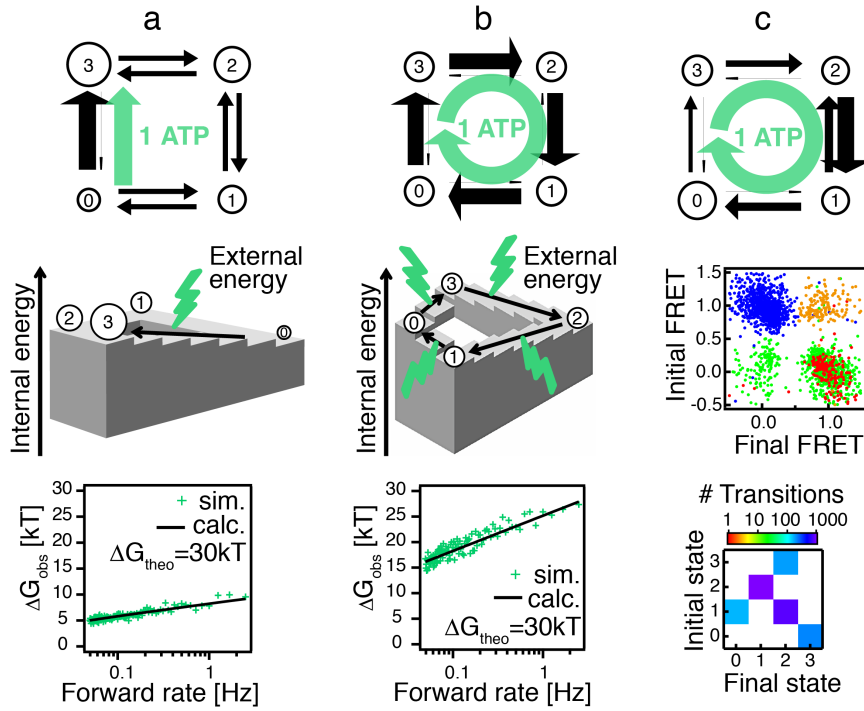


Figure 9.8: Quantifying energy coupling. (a, b) Two simulated limit cases of systems driven by the hydrolysis of 1 ATP. In (a), the external energy is absorbed between states 0 and 3. All remaining rates are set to 0.05 Hz. In (b), the external energy is introduced sequentially over 4 identical steps. The respective state models (top), energy scheme (center), and theoretical detection limit for free energies as a function of the forward rate (bottom) are shown. Simulated values (green) result from Equation (9.2) applied to 200 discrete state sequences with 5 Hz sampling rate and 0.03 Hz bleach rate. They scatter about the expectation value of ΔG_{obs} (black line). (c) A mixture model (top), transition map (center), and transition histogram (bottom) obtained from synthetic data, simulating the flow introduced by coupling to the hydrolysis of 1ATP. The slightly different look of the transition map (compared to experimental data) is the result of uncorrelated noise in the simulations.

Figure 9.8a,b bottom compare the observed free energy differences, ΔG_{obs} , as a function of the dominating forward rate. The values were obtained by Equation (9.2) in the absence of noise or kinetic heterogeneity, and thus, they represent the *upper limit* of ΔG_{obs} . However, a typical data-set size and detection bandwidth of smFRET experiments was assumed (see caption), which defines the range of detectable forward rates. Only a fraction of the original 30kT is recovered, because very unlikely transitions do not occur throughout the data set.

The corresponding expectation value of ΔG_{obs} was calculated from the expected number of observations of a given transition, $\langle N_{ij}^{\text{obs}} \rangle$, in a data set with N_{tot} data points. If $\langle N_{ij}^{\text{obs}} \rangle < 1$, the specific transition cannot be resolved. In this case, f_{ij}^{lost} denotes the factor that is actually missed in the

measurement. The expectation value of the observed free energy change $\langle \Delta G_{\text{obs}} \rangle$ in units of kT is then given by:

$$\langle \Delta G_{\text{obs}} \rangle = - \sum_{\substack{\forall i \neq j \\ (\text{cycl.})}} \ln \left[\frac{a_{ij}/f_{ij}^{\text{lost}}}{a_{ji}/f_{ji}^{\text{lost}}} \right]$$

with:

$$f_{ij}^{\text{lost}} = \begin{cases} \langle N_{ij}^{\text{obs}} \rangle = N_{\text{tot}} \cdot \pi_i \cdot a_{ij} & \forall \langle N_{ij}^{\text{obs}} \rangle < 1 \\ 1 & \forall \langle N_{ij}^{\text{obs}} \rangle \geq 1 \end{cases} \quad (9.3)$$

As expected, the one-step regime is more sensitive to the low detection bandwidth, due to the large ratio of forward to backward rate (10^{13}). Accordingly, a lower fraction of the original $30kT$ is observed, as compared to the distributed regime. This demonstrates that there is no universal limit for resolving energy coupling. Instead, it depends on the investigated system, which can exist in any combination of the two regimes.

Such a mixture model is depicted in [Figure 9.8c](#). It was analyzed in the absence and presence of noise. In the first case, $20.5 kT$ of the original $30 kT$ were resolved. The second case included noise, signal variations and also degenerate FRET efficiencies (2 low, 2 high). Because 3 of the reverse transitions do not occur in the entire data set (cf. transition histogram), SMACKS resolved only $\Delta G_{\text{cyc}} = (12 \pm 2)kT$ in this case. This is 58% of the free energy, which was actually present in the state sequences.

9.4.3 Further Discussion

Despite universal energy conservation, the *observation* of energy differences in the experiment depends on experimental limitations. As demonstrated above, there is no *general* limit for resolving free energy differences from kinetic state sequences. Instead, two limit cases were discussed in the relevant range of experimentally detectable forward rates. In the worst case (1-step energy release), below one third of the original energy difference was resolved from *discrete* state sequences, as compared to 50-95% in the optimal case, where energy release is distributed over all transitions. Including the experimental short-comings observed with Hsp90, further decreased ΔG_{cyc} . In the context of Hsp90, this means that in the worst case only about $3kT$ could be resolved, although the (forward) rates would appear to be well resolved in the experiment.

Finally, the general resolution for free energy differences grows with the size of the data set, cf. Equation (9.3). To some extent, this allows to compensate for the low detection bandwidth of the experiment.

9.5 SUMMARY 2

SMACKS is a novel HMM approach, which resolves all relevant rates that characterize the observed conformational dynamics, from a set of (short) smFRET time traces. The underlying states are identified by their FRET efficiency or kinetic behavior or both. SMACKS is a tailor-made solution for the wide family of protein machines that are clearly more challenging than DNA prime examples.

Moreover, by giving meaningful uncertainty estimates, SMACKS provides new power and confidence to the *unique feature* of single molecule time traces - namely, the analysis of kinetics and thermodynamics at the steady state (explicitly including the non-equilibrium steady-state).

This progress is achieved by the following six key features:

(i) SMACKS exploits the original fluorescence signals of the FRET donor and acceptor as 2D input. The FRET-specific anti-correlation provides significantly increased robustness with respect to uncorrelated noise. This unique information is lost in 1D FRET trajectories.

(ii) SMACKS tolerates experimental intensity variations between individual molecules, while at the same time, the transition rates are extracted from the entire data set.

(iii) SMACKS minimizes the bias of photo-bleaching, because it determines transition rates based on their occurrence in the entire data set. Thus, the range of detectable timescales grows as a function of the data set size.

(iv) SMACKS performs the entire analysis on the experimental (i.e. noisy) fluorescence data. In fact, the knowledge about a given data point's reliability is used to weight its contribution accordingly. Therefore, SMACKS is robust enough to handle realistic noise levels in protein systems.

(v) SMACKS identifies hidden states that share indistinguishable FRET efficiencies, but differ kinetically.

(vi) SMACKS quantifies the precision of extracted rates. The precision is limited by the data set size and signal quality, but it is not compromised by systematic overestimation, which contrasts with previous dwell-time analyses.

The full procedure of SMACKS is also summarized as a flowchart in [Figure 9.9](#).

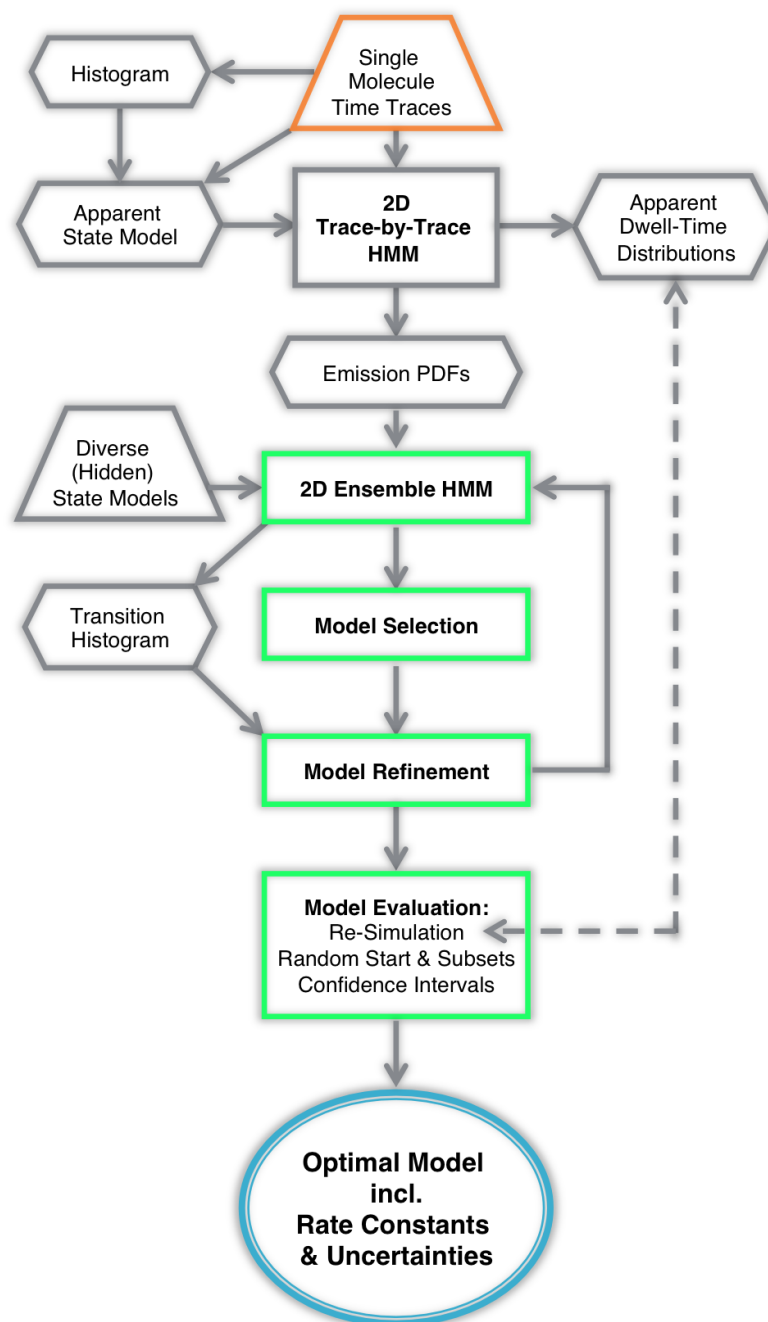


Figure 9.9: Flowchart summary of SMACKS, the *Single Molecule Analysis of Complex Kinetic Sequences*. Based on single molecule time traces (and the histogram thereof) an *apparent* model is deduced. It is used in a trace-by-trace HMM optimization. The optimized, individual emission PDFs are held fixed in a second *semi-ensemble* HMM run. It optimizes one kinetic model based on the entire data set. The BIC is used for model selection and the Viterbi paths are considered for further model refinement. Finally, the model is critically evaluated in several ways.

HSP90'S CONFORMATIONAL KINETICS

It was previously found that Hsp90's conformational changes are only weakly coupled to ATP hydrolysis [109]. Here varied nucleotide conditions were investigated systematically by means of both, the population of individual conformations and corresponding interconversion kinetics.

Unless stated differently, the well known smFRET construct was used (cf. Chapter 7).

10.1 NUCLEOTIDE DEPENDENCE OF HSP90'S CONFORMATIONS

Under most conditions, Hsp90 prevails in an open conformation. This is perceived in the FRET efficiency histogram (Figure 10.1) as a large low-FRET population (>80%). Interestingly, the population distribution is only weakly affected by the presence or absence of ATP and ADP. In contrast, the non-hydrolysable nucleotide analogue, AMP-PNP shifts the the equilibrium predominantly to the closed conformation (>80%).

For all experiments the FRET efficiencies lie within $E_{low} = 0.1 \pm 0.05$, $E_{high} = 0.75 \pm 0.05$, which amounts to inter-dye distances of 92\AA in the open and 53\AA in the closed conformation.

The nucleotide dependence was further confirmed using a protein construct with dye positions other than 61/385 (Section A.5).

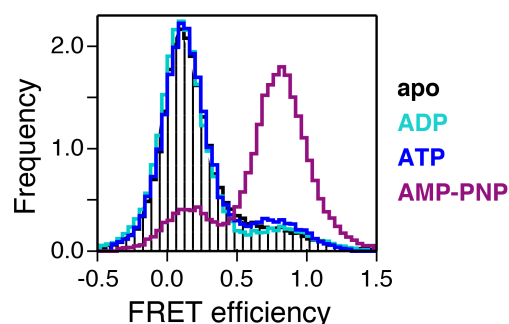


Figure 10.1: Nucleotide dependent population of Hsp90's open and closed conformations. 2mM nucleotides were used.

10.2 NUCLEOTIDE-DEPENDENT CONFORMATIONAL KINETICS

The kinetic results on Hsp90's conformational dynamics are compared in the presence of different nucleotides (2mM ADP, ATP, AMP-PNP) or without nucleotides (apo).

Although 2 peaks are observed in the FRET efficiency histogram, a kinetic 2-state model is not sufficient to describe Hsp90's broad range dynamics. This is already evident from visual comparison of simulated 2-state trajectories to the experimental data on Hsp90. The bi-exponential dwell-time distributions further support this thesis (cf. Figure 8.12d). Finally, according to SMACKS (Chapter 9), Hsp90's conformational kinetics are best described by 4 states (2 low-FRET and 2 high-FRET, Figure 10.2).

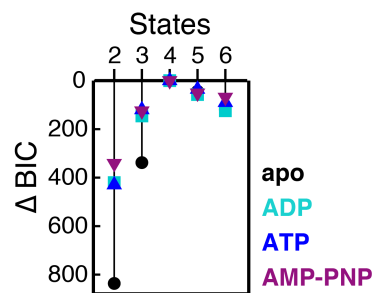


Figure 10.2: Hsp90's conformational kinetics are best described by 4 states. Model selection among differently sized models based on BIC. Black lines serve as a guide to the eye.

10.2.1 A Minimal Kinetic Model

The most plausible aggregate models were determined following the approach of Bruno *et al.*, originally developed for ion channel data [19]. Accordingly, models with varied numbers of links were compared by means of likelihood ratio tests, as detailed in Section B.6.4. These statistical tests indicate that 4 links are required to describe Hsp90's conformational dynamics in the presence of ATP, whereas, under apo, ADP and AMP-PNP conditions, models with 3 links are sufficient. Corresponding models are displayed in Figure 10.3 for all 4 conditions: states 0/1 are long-/short-lived low-FRET states representing open conformations, whereas states 2/3 are short-/long-lived high-FRET states representing closed conformations.

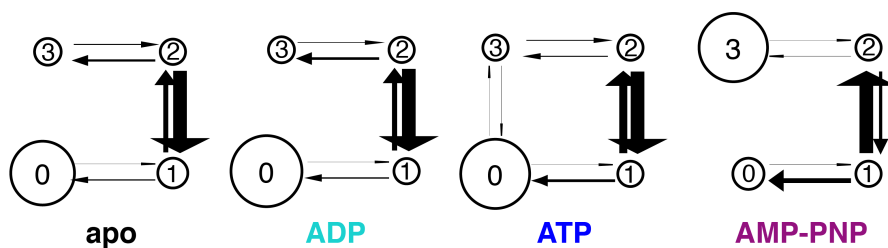


Figure 10.3: Minimal kinetic state models describing Hsp90's conformational changes under different nucleotide conditions as indicated. Circle sizes represent individual state populations. Arrow weights represent relative transition rates.

The transition map (Figure 10.4a) shows the quality of the input data and the state allocation based on the inferred model. The dwells before and after a transition cluster in agreement with the peaks of the FRET histogram, Figure 10.1. It is evident that Hsp90's conformational changes are less defined in the absence of nucleotides.

Furthermore, the resulting transition histograms (Figure 10.4b) are very symmetric about the main diagonal, indicating none of the four systems is far from thermodynamic equilibrium. The latter is a thermodynamic requirement for stationary, linear models. Nevertheless, the results were obtained without corresponding constraints for detailed balance.

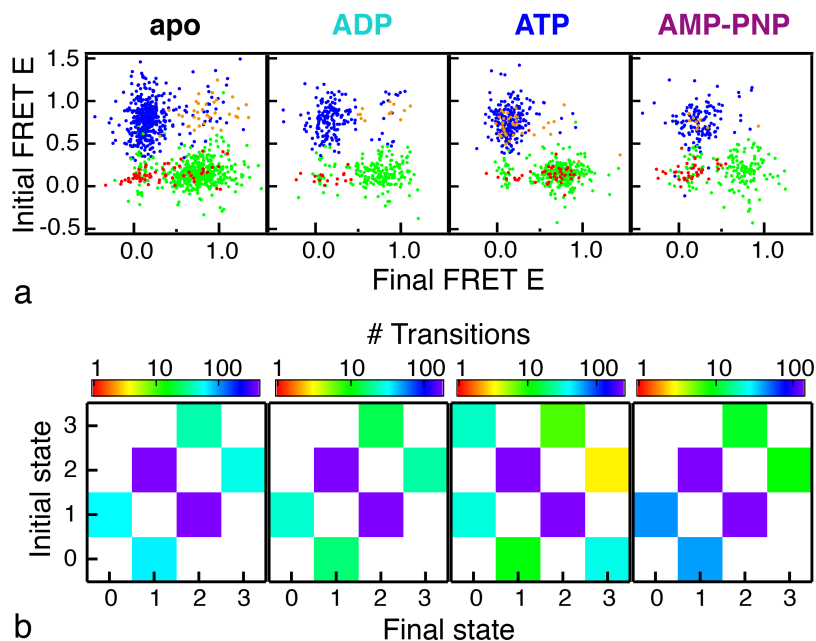


Figure 10.4: Kinetic results of Hsp90 under varied nucleotide conditions as indicated. (a) Transition maps locate transitions in FRET space (initial states 0, 1, 2, and 3 in red, green, blue, and orange, respectively). (b) The occurrence of transitions across the dataset.

10.2.2 Nucleotide Effects on the Transition Rates

The rates under apo and ADP conditions are similar to those in the presence of ATP (Figure 10.5 bottom). Only with the non-hydrolysable ATP-analogue, AMP-PNP, the rates between both short-lived states are inverted. This is consistent with the pronounced shift towards closed conformations observed in the FRET histogram, in the presence of AMP-PNP (Figure 10.1).

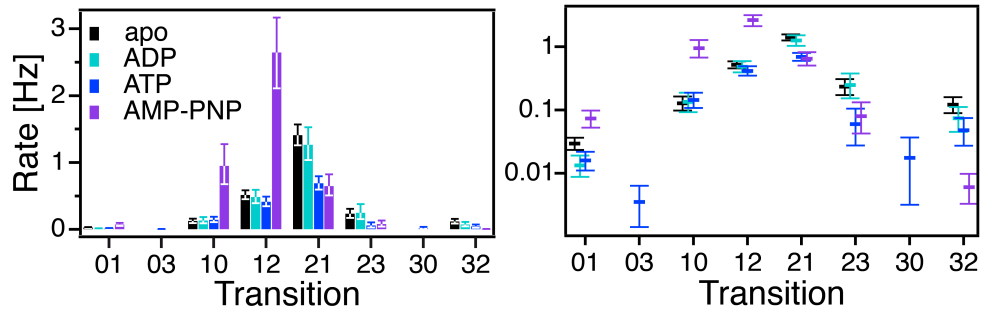


Figure 10.5: Transition rates deduced for Hsp90's nucleotide dependent conformational kinetics, displayed in linear (left) and logarithmic scale (right). Error-bars represent 95% confidence bounds.

10.3 THERMODYNAMIC CONSEQUENCES

Thermodynamic aspects of all 4 nucleotide conditions are summarized in the 1D-projection of the energy landscape, displayed in Figure 10.6a. It holds the free energy differences and barrier heights calculated from the transitions rates above. The latter were estimated assuming Arrhenius behavior and a typical attempt frequency for proteins of 10^8Hz [120, 121].

As expected and required, in the absence of an external energy source, Hsp90's conformational dynamics are in thermal equilibrium. This is recognized by the linear models and corresponding transitions in Figure 10.4b. However, for Hsp90 in the presence of ATP, no driven dynamics were found either, with $\Delta G_{\text{cyc}} = (0.9 \pm 0.9)\text{kT}$ over the closed cycle in Figure 10.3, which is far below the 30kT expected for ATP hydrolysis (specified in Section 9.4.2). In Section 9.4.3, I discussed how the temporal detection bandwidth and further short-comings of the experiment decrease the observed free energy differences. But even in view of these effects, a larger free energy difference would be expected if the conformational changes were really driven by ATP hydrolysis, given the fact that the transitions themselves are indeed temporally resolved in the experiment.

This suggests that the energy of ATP hydrolysis is not directly coupled to the observed conformational changes, which is consistent with the fact that transitions are also observed in the absence of ATP. It further supports earlier results [109].

A schematic 3D-representation of the energy landscape is shown in Figure 10.6b. It highlights the fact that two observable FRET states could be split into 4 kinetic states, based on distinct kinetic behavior.

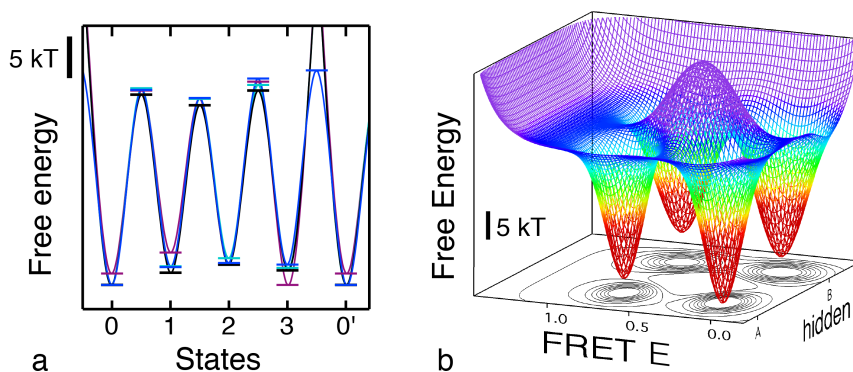


Figure 10.6: Energy landscape of Hsp90's conformations. (a) Energies deduced from the transition rates assuming an attempt frequency of 10^8Hz . (b) A 3D-representation of the energy landscape highlights the detection of *hidden* states, given their distinct kinetic behavior.

10.4 DISCUSSION

10.4.1 Interpretation of the 4 Kinetic States

Using SMACKS, 4 states were resolved based on characteristic FRET efficiencies and also distinct kinetic behavior: one long-lived and one short-lived open state (states 0 and 1) along with one short-lived and one long-lived closed state (states 2 and 3).

A possible interpretation of the latter two states involves the position of the very N-terminal β -strand, β 1, introduced in [Chapter 2](#). Coming from open conformations, β 1 is first internally attached to the 7-strand β -sheet of the N-domain [124]. Once closed, contacts with the opposite protomer can be formed (cf. crystal structure in [Figure 2.1](#)). These confer additional stabilization to the long-lasting closed state (state 3 in [Figure 10.7](#)right). Contrariwise, in the non-exchanged case, the closed state (state 2) is less stable and therefore short-lived. In agreement with the presented data, both conformations cause the same high-FRET observations.

Interestingly, an Hsp90 mutant lacking β 1 (known as Δ 8) showed a larger N-terminally closed population upon nucleotide binding, and also faster ATP hydrolysis [133, 109]. This was explained by the abolished internal attachment [133], which presumably prevents hetero-dimerization of the α 1-helices adjacent to β 1. Actually, Hsp90- Δ 8 is lethal *in vivo* despite the increased ATPase activity [168]. Nevertheless, a direct comparison to the dynamics of Δ 8 would be an important hypothesis test; also because the cited earlier results were obtained with a positively charged N-terminal His-tag, which increases the ATPase rate of full-length Hsp90, too.

Regarding the open states, the emerging notion implies an entire ensemble of conformations [61]. Within the short time window of the smFRET experiment, such a kinetic ensemble is well described by 2 states.

A broader range of timescales is discussed in [Chapter 13](#).

In addition to the kinetic models depicted in [Figure 10.3](#), further mathematically *equivalent* models can not be excluded based on the presented kinetic data alone (cf. [Section B.6.4](#)). But in view of the previous considerations together with the long-distance transition path between the observed open and closed conformations, the presented models (with the fewest open-to-closed links) appear as the most likely ones. Also the fast exchange between the two short-lived states (one open, one closed) on the one hand, and occasional transitions into more *kinetically distant*, longer-lasting open or closed states, on the other hand, fits well into the outlined overall picture.

10.4.2 The Role of ATP Hydrolysis in Hsp90's Conformational Dynamics

The role of Hsp90's slow ATPase rate is a long standing and controversial question [116, 75, 53]. Considering the presented smFRET data, the inferred *cyclic* state model appears only in the presence of ATP. Although this may seem to be a very abstract finding, it represents a clear difference to all other discussed conditions.

On that account, it is intriguing to speculate that hydrolysis may trigger a - possibly small - rearrangement in the N-terminal domain, thereby unlocking

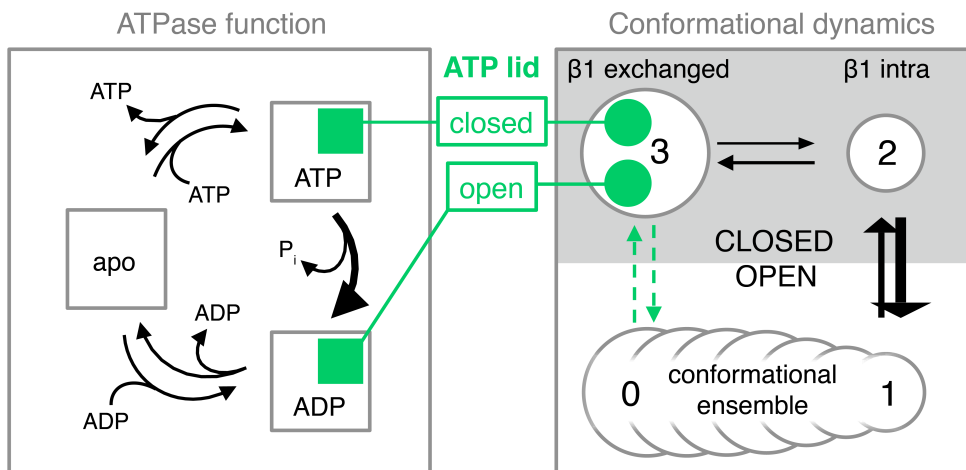


Figure 10.7: Proposed connection between ATPase function (left frame) and conformational dynamics of Hsp90 (right frame). In addition to the ATP independent conformational changes (right, black straight arrows), the ATP lid could mediate the observed ATP-dependent effect (green dashed arrows). Lid-open and lid-closed subpopulations (green discs) of the main conformational states (gray circles) are proposed to be congruent with the corresponding subpopulations (green squares) of the ATP or ADP states (gray squares) in the ATPase frame. The gray area denotes closed conformations causing high-FRET signals, in contrast to open conformations (white area in the right frame). See main text for details.

a new *kinetic path* for the large opening and closing transitions, i.e. transitions on a distinctive timescale.

There is evidence that the ATP-lid (introduced in [Chapter 2](#)) could be involved in such a small rearrangement [122, 140]. Also the cross-protomer interaction of the $\beta 1$ -strand is thought to be further stabilized by lid closure, which was found upon ATP - but not ADP - binding [123, 2, 32]. Contrariwise, lid opening after ATP hydrolysis (or dissociation), provides again intramolecular attachment sites to $\beta 1$. Thus the cross-protomer ties are loosened again. Because hydrolysis dependent loosening could occur only from *within* a particular closed state, it has the potential to introduce directionality to the system.

The model shown in [Figure 10.7](#) illustrates this rationale. N-terminal opening and closing (right) is independent of ATP hydrolysis, and occurs also in the absence of ATP. Yet, subpopulations of the conformational state 3 (lid open or closed, green) may be congruent with subpopulations of the ATP or ADP state (left). Thus it is plausible that ATP binding and/or hydrolysis have an *additive* effect on Hsp90's conformational kinetics, which could explain the observed ATP-dependent feature; namely a lower energy barrier between state 3 and state 0, unlocking "*a new kinetic path*". In summary, combining literature and new results, a possible scenario for 3-to-0 transition starts by $\beta 1$ exchange and lid closure over the bound ATP, followed by ATP hydrolysis (or dissociation) prompting lid opening and in turn $\beta 1$ loosening, which ultimately favors direct opening to state 0. This aspect was further investigated under ATPase stimulation by the cochaperone Aha1, which is covered in [Section 11.1](#).

Since lid closure is not detectable in the discussed smFRET experiment, its timescale of occurrence is unclear. It could either be rate-limiting for hydrolysis [123] and as such coincide with the ATPase rate, or occur more frequently.

In this connection, the occurrence (particle flux) of the 3-to-0 transition is worth mentioning: $\pi_3 \cdot a_{30} = 0.1/\text{min}$. According to the proposed model, this transition represents the *hydrolysis-mediated* transition from the closed conformation with exchanged $\beta 1$ -strands to the ensemble of open conformations. Remarkably, it matches precisely the timescale of hydrolysis.

Finally, as stated before, the investigation of additional reaction coordinates (i.e. dye positions) is necessary to validate the proposed concept.

10.5 SUMMARY 3

Hsp90 undergoes large conformational changes, which span about 40Å at the measured positions and considerably more at its extremes. Thereby, it occurs mainly in open conformations, regardless of apo, ADP and ATP conditions. Only the artificial AMP-PNP keeps Hsp90 mostly in its closed conformations.

Accordingly, no direct coupling was observed between conformational dynamics and ATP hydrolysis. Yet, in the presence of ATP, a subtle difference was found in the inferred kinetic state model. Generally, within the investigated timescales, the conformational dynamics are best described by a kinetic 4-state model including 2 open and 2 closed states, which were related to specific structural features.

BIOCHEMICAL MANIPULATION OF HSP90

11.1 ATPASE STIMULATION BY COCHAPERONE AHA1

In view of the results obtained in the presence of ATP, Hsp90's hydrolysis rate was stimulated >10-fold by its cochaperone Aha1¹ [115]. If we had missed out on the directionality due to the slow ATPase rate, this should ultimately allow us to resolve putative energy coupling.

For optimal interaction affinity with Aha1, measurements were performed in low salt buffer². For comparison, data without Aha1 was measured accordingly. A systematic discussion of Hsp90's salt dependence can be found in [Section 12.2](#).

Notably, significant binding was previously found for Aha1 with labeled Hsp90-385C at much lower concentration of 0.3 μ M [91], which is exactly the dissociation constant reported for unlabeled Hsp90 [115]. This implies that, although not directly detectable in the experiment, Hsp90 exists predominantly in complex with Aha1 under the used conditions.

Aha1 shifts the steady-state populations towards closed conformations ([Figure 11.1a](#)). Nevertheless, [Figure 11.1b](#) shows that the general kinetic behavior is only weakly affected. In agreement with the ATP related results of the last section, a 4-link model was inferred with ATP + Aha1, too.

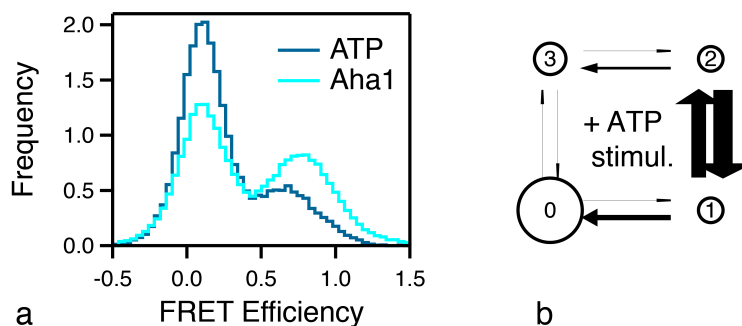


Figure 11.1: Effects of Aha1 on the conformational dynamics of Hsp90. (a) Aha1 slightly stabilizes closed conformations. (b) Hsp90's conformational state model under Aha1 stimulation summarizing the transition rates in [Figure 11.2](#). Arrow weights indicate the size of each rate constant. Circle sizes represent state populations.

And even highly stimulated hydrolysis does not induce appreciable conformational directionality in Hsp90. Specifically, $\Delta G_{\text{cyc}} = (-0.4 \pm 1.2) \text{ kT}$ was obtained from the transition rates in [Figure 11.2](#).

The shift in the FRET efficiency histogram is mainly caused by corresponding changes of the fast rates between states 1 and 2.

¹ Yeast Aha1 was a kind gift of Markus Jahn.

² 40mM Hepes, 20mM KCl, 5mM MgCl₂, pH 7.5 with 3.5 μ M Aha1 and 2mM ATP

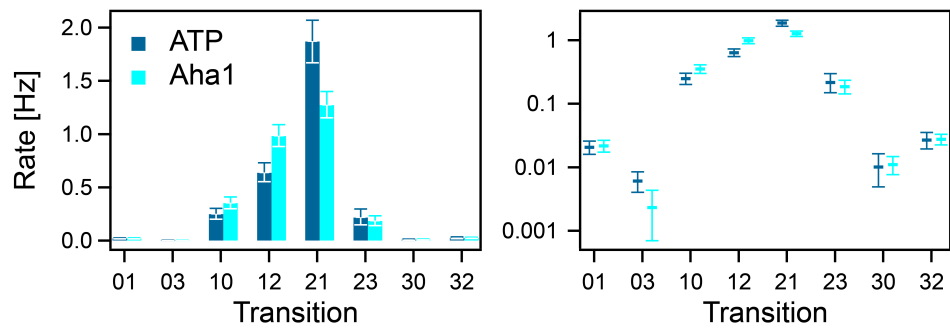


Figure 11.2: Hsp90's transition rates in the presence of Aha1 displayed in linear (left) and logarithmic scale (right).

11.1.1 Discussion

Despite the relatively drastic stimulation of Hsp90's ATPase rate by its cochaperone Aha1 [115], its effect on the conformational dynamics of Hsp90 is rather weak. The interaction with Aha1 caused a 20%-shift towards Hsp90's closed conformations, which represents a stabilization of about 0.5kT. This is in line with previous qualitative results [91, 64]. The stabilization is commonly explained by Aha1's cross-protomer contacts [131].

But how can a 20% shift provoke a >10-fold ATPase stimulation? A probable explanation thereof suggests that Aha1 increases the *collective* probability of multiple, otherwise uncorrelated features. For example Aha1 is believed to communicate with the ATP-lid supposedly through interactions with the N-terminal $\beta 1$ - $\alpha 1$ -segment [122, 140]. In addition, Aha1 is believed to stabilize the association of Hsp90's N-terminal and middle domain, thereby favoring the hydrolysis competent state of the catalytic loop [107, 131].

And how can all of these coincide with the weak changes on Hsp90's dynamics? In fact, already previous data [91] indicate that Aha1 binds also to Hsp90's open conformations, yet with lower affinity. Together with the modest stabilization of the closed conformations, this shows that Aha1 does not conserve Hsp90 in a single conformation. In fact, Hsp90's large conformational changes remain largely unaffected by Aha1 binding

Once more, these results strengthen the notion that Hsp90's large conformational changes are mainly independent of ATP hydrolysis. Nevertheless, the presented data supports an indirect connection, e.g. involving the ATP lid (detailed in [Section 10.4](#)).

11.2 THE EFFECT OF DRUG CANDIDATES

Hsp90 is a central target in anti-cancer therapy. Four classes of inhibitors are currently investigated: geldanamycin (GDA), radicicol (RDC) and purine derivatives bind to the N-terminal ATP binding site, whereas the novobiocin derived class targets Hsp90's C-terminus. For all of these compounds, the molecular consequences of inhibition on Hsp90's function are not currently known. Therefore, a representative of each class was investigated concerning its effect on Hsp90's conformational dynamics, namely GDA, RDC, PU-H71¹ [72, 135] and KU32² [7] in the above order.

As expected, Hsp90's ATPase rate was inhibited by the competitive inhibitors (GDA, RDC, PU-H71), but not by compounds binding to the C-terminus, such as KU32 (see [Section A.6](#)).

All compounds were applied at concentrations 100-fold higher than the reported dissociation constant - or the half maximal inhibitory concentration (IC₅₀) if the former was not available. The specific concentrations were 100μM GDA [136], 1μM RDC [136], 12μM PU-H71 [59], 10μM KU32[94]. None of the 4 inhibitors had a substantial effect on the equilibrium population of Hsp90's conformations ([Figure 11.3](#)).

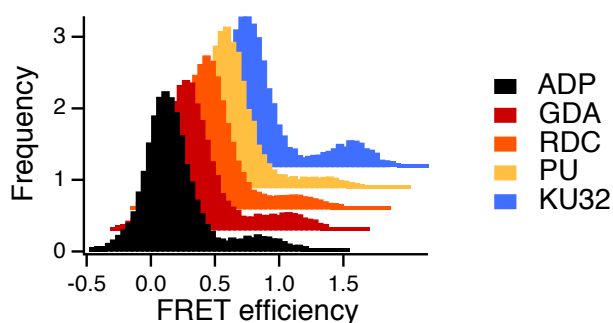


Figure 11.3: Hsp90's conformational equilibrium is not significantly affected by inhibitors.

Conformational kinetics were analyzed by smFRET using 1Hz to 55Hz sampling rate. Representative dwell time distributions are displayed in [Figure 11.4](#). The differences to the data measured in the presence of ADP is very small. Slightly faster opening is observed with radicicol and KU32. Timescale dependent shifts were found for opening and closing in the presence of PU-H71, as well as closing with KU32.

1 PU-H71 was a kind gift of Prof. Leonard M. Neckers.
2 KU32 was a kind gift of Prof. Brian S. J. Blagg.

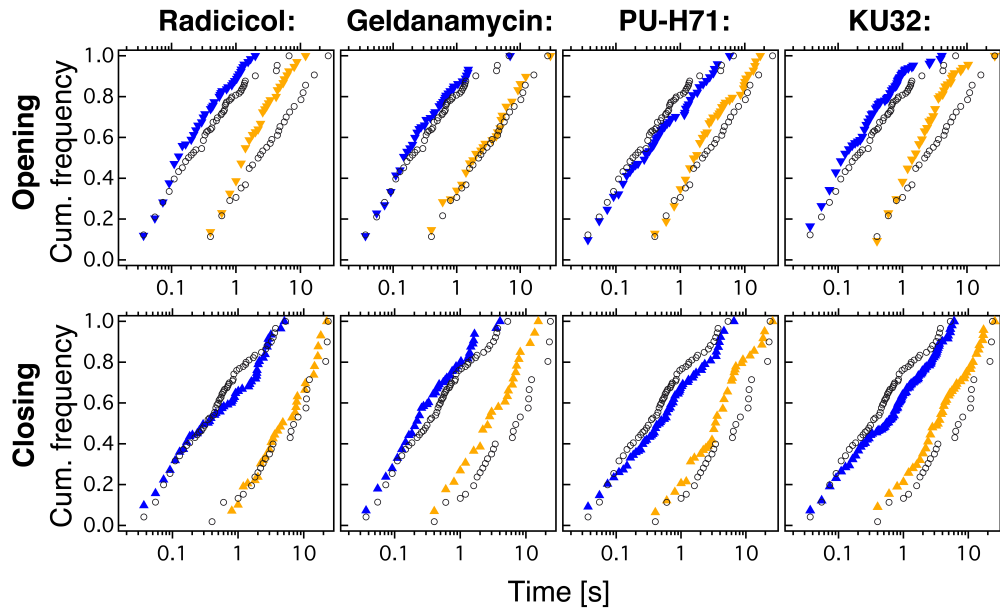


Figure 11.4: Dwell time distributions measured at 2 sampling rates: 55Hz blue, 5Hz ALEX, yellow. Corresponding data obtained in the presence of 2mM ADP is shown in black for comparison.

Because such dwell time distributions are a very coarse way of analyzing smFRET time traces, 5Hz ALEX data was further analyzed using SMACKS. As shown in [Figure 11.5](#) a 4-state model with 3 links was found in all cases, which agrees with the absence of ATP hydrolysis (cf. [Chapter 10](#)). Interestingly, N- and C-terminal inhibitors show very similar kinetics. In fact, the largest difference is observed among the competitive, N-terminal inhibitors, which differ only by non-covalent interactions with the nucleotide binding pocket.

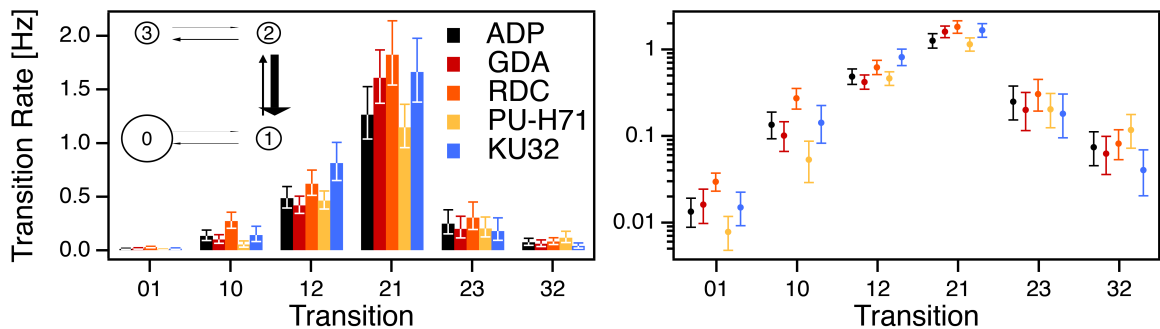


Figure 11.5: Conformational kinetics is weakly affected by inhibitors. Transitions are specified in correspondence with the inset state model (left), where states 0,1 and 2,3 denote low- and high-FRET states, respectively. Small rates are better perceived in logarithmic scale (right). Error bars represent confidence intervals determined by SMACKS.

11.2.1 Discussion

It is commonly believed that conformational changes are limiting for Hsp90's activity [137]. Nevertheless, these results indicate that its large conformational changes are not crucially affected by the inhibitors: neither regarding the population of open and closed conformations, nor with respect to the kinetics in the range of 20 milliseconds to minutes.

To date, a molecular explanation for the effects of Hsp90 inhibitors observed in anti-cancer therapy is still largely unknown. Understanding the consequences of *competitive* inhibition is tightly coupled to the understanding of Hsp90's ATPase function in general. This study did not resolve substantial effects of ATPase inhibition on Hsp90's large conformational changes, thus excluding interference with such dynamics as a possible cause. Instead, it further substantiates the earlier finding that those conformational dynamics do not rely on ATPase function.

Novobiocin derived inhibitors bind to the C-domain, which represents the global hinge of the Hsp90 dimer (see [Section 11.3](#)). Therefore, effects on the large conformational dynamics and associated allosteric regulation were initially expected, but not observed herein. A negative effect of the C-terminal zipper on the binding affinity of KU32 can not be fully excluded. Nevertheless, preliminary ensemble results of unzipped Hsp90 did not reveal allostery either ([Figure A.11](#)). Further discussed mechanisms of Novobiocin derivatives include interference with client [96] and/or cochaperone (e.g. Sba1/p23, Cdc37) interaction [99, 166] as well as dimerization [3], which asks for further analysis.

11.3 INTERFERING WITH HSP90'S HINGE

Post-translational modifications represent a very direct and reversible way of regulation. An S-nitrosylation in Hsp90's C-domain was found to have an inhibitory effect on both, the ATPase function and the stimulation of endothelial nitric oxide synthase by human Hsp90 α [97].

The specific nitro-site, Cys597, is conserved in human Hsp90 α , Hsp90 β and homologues in eukaryotes and bacteria, but not in Grp94, Trap1, yeast Hsp90 or HtpG of *Escherichia coli*. The corresponding residue in yeast Hsp90 is 577A, which is part of a 3-strand β -sheet (see Figure 11.6). In contrast to the inhibitory effect of nitrosylation of this residue, the A577I mutation caused a nearly 4-fold amplification of the ATPase rate [132].

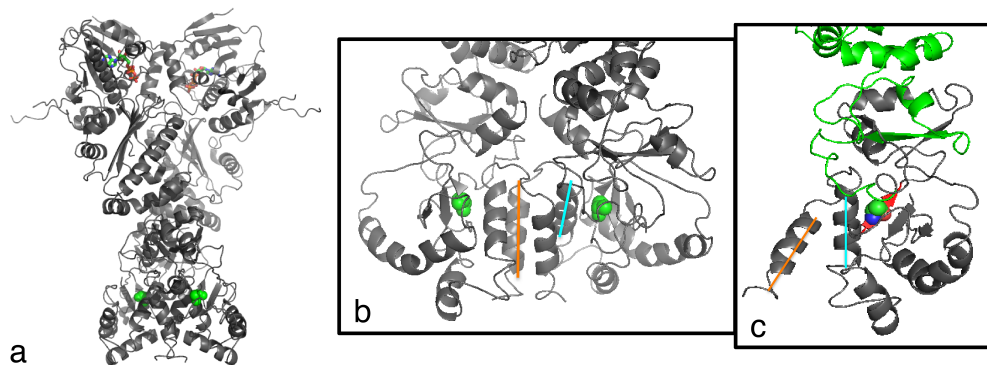


Figure 11.6: The localization of residue 577A (green spheres) in yeast Hsp90 (pdb:2cg9): (a) in view of the full dimer with bound nucleotides (colored sticks); (b) with respect to the dimerized C-domains; (c) regarding the interface of the middle (green) and C-domain (gray) with the associated β -sheet in red. (b,c) Lines in orange (cyan) label the very last (second last) α -helix of the right monomer, respectively.

This is an interesting example of a wide-range communication from the C-domain all the way to the N-terminal ATPase site. As such it can provide valuable, mechanistic insights in Hsp90's intra-molecular correlations and dependencies. Earlier ensemble FRET experiments suggest a slow down of the dimer dissociation rate by the A577I mutation and a larger fraction of closed conformations compared to wild-type yeast Hsp90 [132].

Yet, post-translational modifications occur rarely symmetrically. They rather convey asymmetry to homo-dimeric proteins [100]. Therefore, the dynamics of Hsp90's N-terminal opening and closing was investigated for 577I/wt hetero- and 577I homo-dimers in comparison to wild-type (i.e. 577A), based on the well established FRET construct (cf. Chapter 7).

Figure 11.7 shows indeed a relative stabilization of Hsp90's closed conformations upon A577I mutation. Interestingly, already the hetero-dimer shows a considerably larger population of closed conformations, especially in the presence of ATP. Under ADP conditions the effect is weaker, which is consistent with the transition rates displayed in Figure 11.8.

Nevertheless, under both conditions, the second A577I leads to a further shift towards closed conformations. This is mainly due to the fast rate from

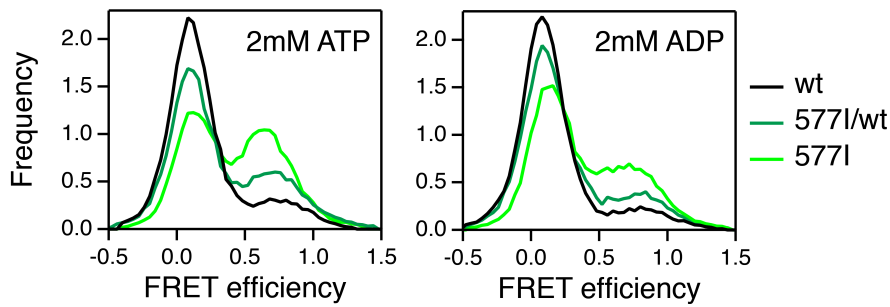


Figure 11.7: C-terminal point mutations modulate Hsp90's conformational steady-state distributions in the presence of ATP and ADP.

open to closed conformations (state 1 to state 2), which is nearly doubled for the 577I homo-dimer under both, ATP as well as ADP conditions. Please note that a smaller kinetic state model with only three links (similar to the inset in Figure 11.8 bottom) is statistically sufficient to describe the observed kinetics of the 577I homo-dimer in the presence of ATP, implying kinetically less heterogeneous fluctuations. Furthermore, very fast transitions at the temporal resolution limit occurred more frequently. Both findings could indicate a stiffened structure of the 577I homo-dimer with a smoothed (less rough) energy surface, leading to relatively streamlined conformational transitions rather than extensive random walks.

Lastly, both FRET peaks of the 577I homo-dimer (Figure 11.7) seem to shift slightly towards medium FRET efficiencies, indicating comparatively less extended open and more extended closed conformations. But these small shifts remain to be confirmed by confocal smFRET and additional reaction coordinates.

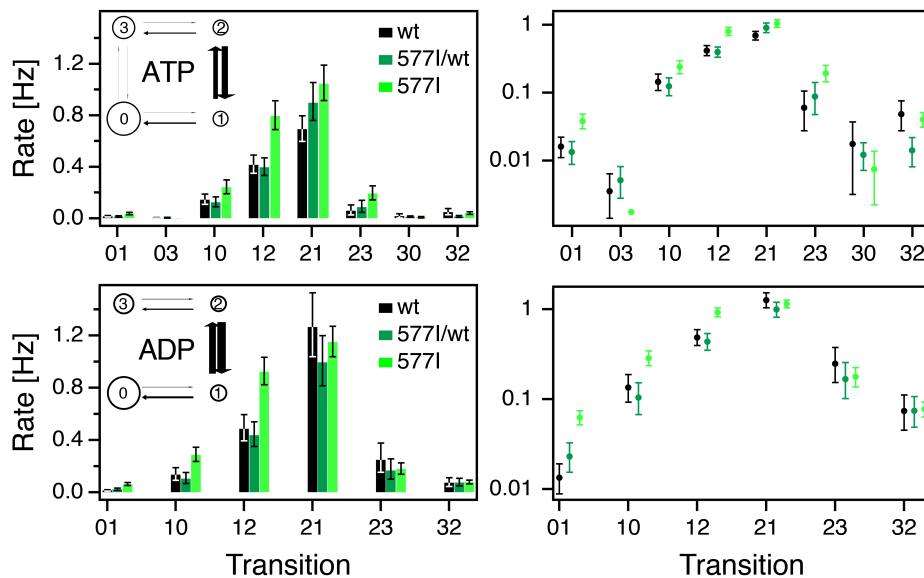


Figure 11.8: The influence of C-terminal point mutations on Hsp90's conformational kinetics in the presence of 2mM ATP (top) or 2mM ADP (bottom). Representative cartoons are provided as insets. On the right, the data is presented in logarithmic scale.

11.3.1 Discussion

The ATPase rate of hetero-dimers is difficult to dissect in a mixture of both variants, 577A and 577I, with varied dimer dissociation constants. Therefore, a direct comparison of *conformational* with *functional* effects is not possible at this time. Specifically, the question whether one A577I mutation is enough for the observed ATPase amplification remains elusive.

In general, the ATPase amplification is not a priori expected, as it results from a hydrophobic to hydrophobic point mutation. Also, the little bulkier isoleucine side chain points outward - at least in the crystalized, closed conformation of yeast Hsp90. Thus interference with the mentioned β -sheet is rather unlikely.

However, the situation might be different in one of the open conformations. The slight but consistent shift of the corresponding low-FRET peaks in [Figure 11.7](#) implies that the farthest opening might be sterically hindered by symmetric A577I mutation. Thus, the observed ATPase amplification could result from a destabilization of extremely open off-states.

11.4 SUMMARY 4

The interaction of Hsp90 with the cochaperone Aha1 leads to a relative stabilization ($0.5kT$) of closed conformations. But despite the strong stimulation of Hsp90's ATPase rate by Aha1, the observed conformational dynamics occur in thermal equilibrium.

Drug candidates targeting either Hsp90's nucleotide binding pocket (radicol, geldanamycin, PU-H71) or C-domain (KU32) had no significant effect on the large conformational changes of Hsp90. This substantiates once more the independence of the observed dynamics from ATPase function. However, the insensitivity of the dynamics towards C-terminal modulation was not expected.

Contrariwise, an A577I point mutation in the C-domain has a large effect on both, Hsp90's conformational dynamics and its ATPase function. The population of closed conformations increases additively from wt/wt to A577I/wt to A577I/A577I dimers in the presence of ADP as well as ATP.

PHYSICAL MANIPULATION OF HSP90

12.1 MACROMOLECULAR CROWDING & VISCOSITY

The inside of a cell is crowded with macromolecules, such as proteins, nucleic acids and sugars as visualized in [Figure 12.1](#). Depending on the cell and the cell state, macromolecules populate 5-40% of the intra-cellular volume with concentrations of up to 400mg/ml [45].

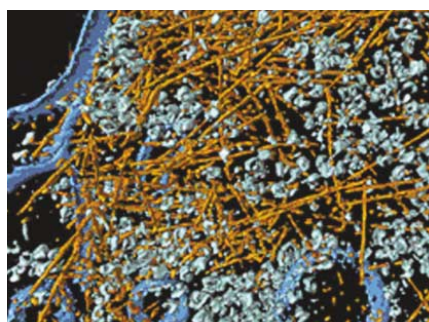


Figure 12.1: The crowded environment in a cell visualized by a rendered and colored cryo-EM tomography [103, 45]: actin filaments, orange; ribosomes and other macromolecular complexes, gray; membranes, blue.

This has far reaching effects on the function of proteins, even if they do not *chemically* interact with these species. Features affected by macro-molecular crowding include, amongst others, protein folding and conformational stability, enzymatic activity, protein-protein interactions, small molecule interaction, aggregation and amyloid formation. In fact, as stated recently [85], it is hard to find a single property of proteins that is *not* affected by high concentrations of macro-molecules.

Many of these diverse symptoms can be explained by the *excluded volume effect*. It arises because in the crowded milieu, space - and the number of ways to populate it - are limited. This leads to an entropy driven increase of the chemical potential of a given solute molecule. As such, the effect is strongly size dependent because the larger the molecule, the larger is the inaccessible, i.e. *excluded*, volume as illustrated in [Figure 12.2](#). Consequently compact structures and also protein association are favored by the excluded volume effect. Besides, changes in solvent properties (e.g. viscosity, osmotic pressure), perturbed diffusion and so-called *soft* interaction between target protein and crowder play important roles, too.

Although the plain macro-molecular crowding aspect of the cellular environment is mimicked quite simply using well-known crowding agents, most *in vitro* studies disregard this aspect completely.

Herein, I investigated the effect of macromolecular crowding on Hsp90's conformational dynamics. In addition, the experiments aimed to dissect the

influence caused by the excluded-volume effect, on the one hand, and increased viscosity, on the other hand.

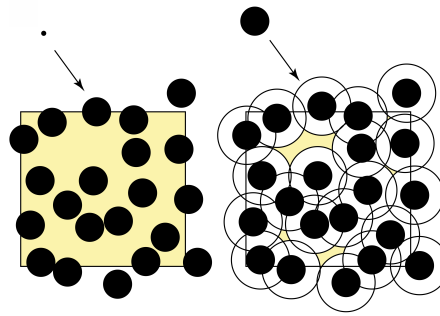


Figure 12.2: Cartoon illustrating the excluded volume effect [44]. The same crowded situation, provides much more accessible volume (yellow) for a small particle (left) as compared to a larger one (right).

12.1.1 Experimental Setup

To this end, experiments were performed in the presence of increasing concentrations of monomeric sucrose or branched, polymeric sucrose, known as Ficoll 400 (Sigma Aldrich) displayed in Figure 12.3a,b. The latter is a common macromolecular crowding agent [23, 44, 84]. Although both substances are constitutionally very similar, a factor of 1000 separates the two in molecular weight (342g/mol or 400±100kg/mol, respectively). Their hydrodynamic radii were specified with 5Å for sucrose [98] and 80Å for Ficoll 400 [23]. Correspondingly, their solutions cause very different viscosities, e.g. at 20wt% $\mu_{\text{rel}}(\text{sucrose}) \approx 2$ [147], $\mu_{\text{rel}}(\text{Ficoll 400}) \approx 20$ ¹. On the other hand, the densities of the same weight percent solutions are very similar. The situation of Hsp90 in the presence of the small viscogen sucrose or

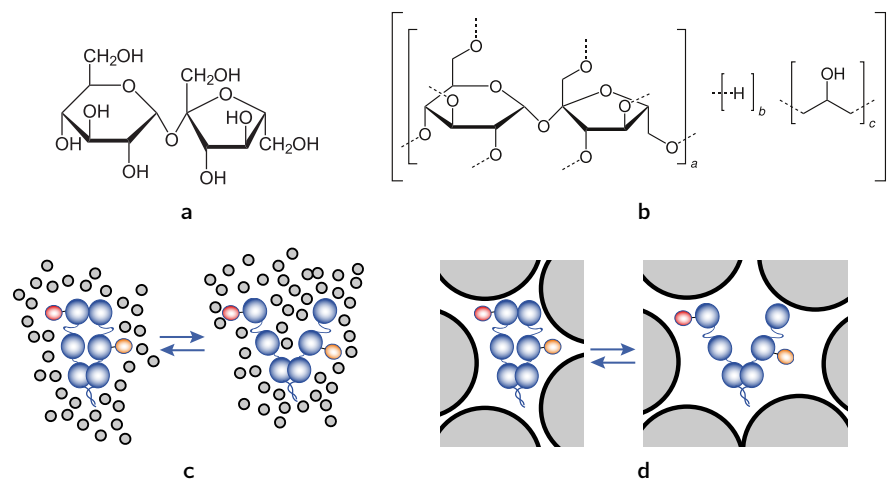


Figure 12.3: Setup of crowding experiments. Structural formula of sucrose (a) and Ficoll 400 (b). Cartoon of open and closed Hsp90 in the presence of sucrose (c) or Ficoll 400 (d).

1 Amersham Biosciences, Data File: Cell Separation, 18-1158-27 AA, 11/2001, p2

the macromolecular crowder Ficoll 400 is illustrated in Figure 12.3c,d. The impact of both substances on Hsp90 is compared below under the same nanoscopic conditions, i.e. equally *densely* crowded environments, rather than equal viscosities.

12.1.2 Size Dependent Stabilization of Closed Conformations

Figure 12.4 shows a substantial, concentration-dependent stabilization of Hsp90's closed conformations in the presence of the macromolecular crowder Ficoll 400. In contrast, the small viscogen sucrose leads to further population of open conformations. The change in the free energy difference between open and closed conformations amounts to less than $1kT$ in both cases.

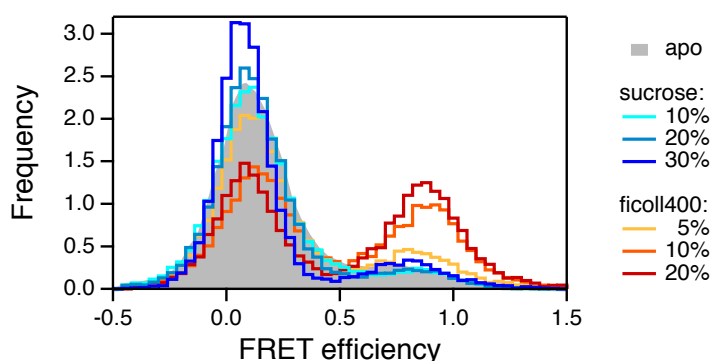


Figure 12.4: The effect of viscosity and macromolecular crowding on Hsp90's conformational equilibrium. Concentrations are specified in weight percent.

12.1.3 Viscosity Slows Down Fast Fluctuations

Changes of the conformational dynamics are visible already from the stationary distributions: as shown in Figure 12.5, the low and high FRET populations get more and more separated at increasing sucrose concentrations. This is indicative of fast fluctuations, at or below the timescale of the sampling rate, that are slowed down at higher viscosity. A similar effect could be the reason for the slight right-shift of the high-FRET peak observed with Ficoll 400 in Figure 12.4.

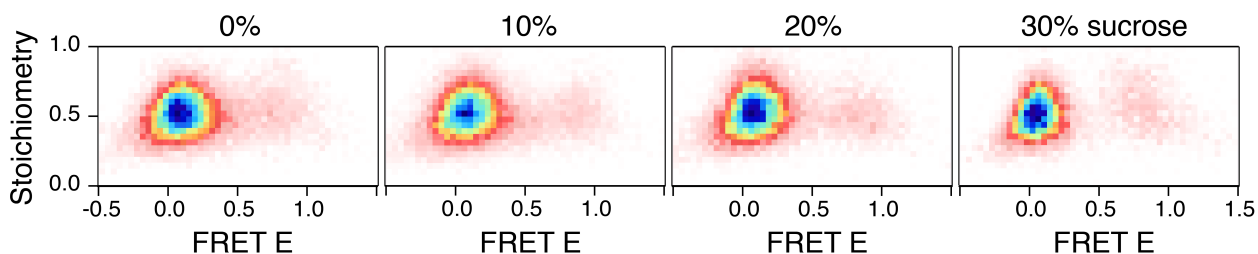


Figure 12.5: Viscosity suppresses fast dynamics ($\leq 100ms$), which causes less overlapping populations in the 2D histogram (zero counts, white; maximal counts, dark blue).

Still, transitions between open and closed conformations are regularly observed in the experiment. In fact, the slower, fully resolved kinetics are only weakly affected by viscosity or macromolecular crowding (see Figure 12.6). The main difference is found for the rates between both long-lived closed states, in agreement with the corresponding stabilization observed with Ficoll 400.

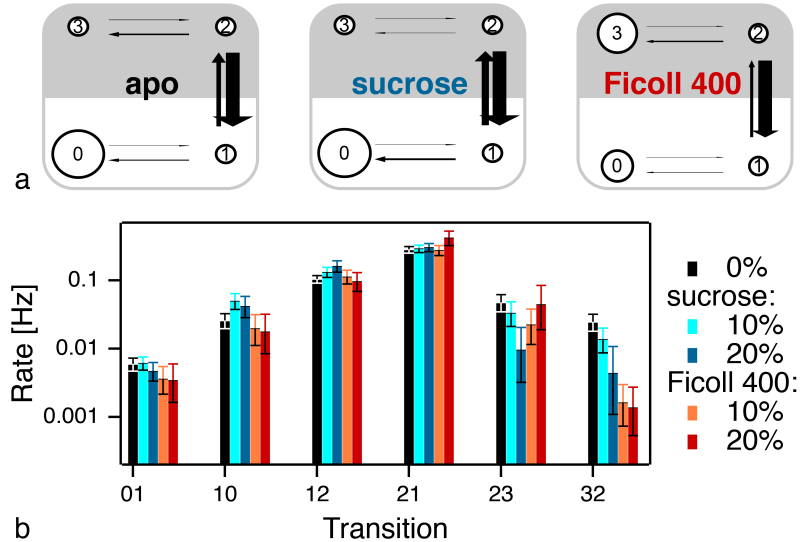


Figure 12.6: The resolved kinetics of Hsp90 are only weakly affected by viscosity and crowding. (a) Kinetic state models: closed states, gray; open states, white; population represented by circle size; transition rate represented by arrow width. (b) Transition rates with confidence intervals in logarithmic scale.

12.1.4 The Crowding Effect on Hsp90's Activity

Hsp90's inherently slow ATPase rate was measured under increased viscosity and macromolecular crowding (see Figure 12.7). Along with the larger population of closed conformations, the ATPase rate increases more than 4-fold in the presence of 15% Ficoll 400. Whereas - consistently with the unchanged conformational populations - at similar weight fractions of the viscogen sucrose, the ATPase function remains unaffected.

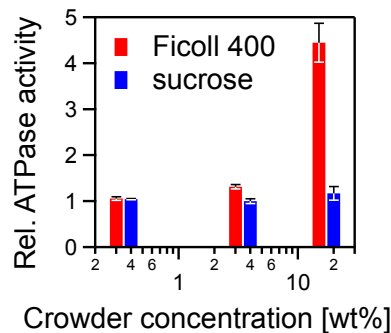


Figure 12.7: The effect of sucrose and Ficoll 400 on Hsp90's ATPase activity. The reference hydrolysis rate of Hsp90 was 0.37 ATP/min/monomer.

12.1.5 Discussion

Sucrose and branched sucrose, alias Ficoll 400, share very similar properties, such as polarity and density. Their major difference is the hydrodynamic radius. This makes them a perfect test system to investigate crowder-size dependent effects. Naturally, in the cell, macromolecular crowding involves a broad distribution of sizes from a few kilodaltons up to megadalton complexes and large cytoskeletal filaments.

Figure 12.8 illustrates the *crowder view* on open and closed conformations of Hsp90. In a sucrose solution, the excluded volumes of both conformations are almost equal to their Van der Waals volumes. Thus, according to the excluded volume effect, the difference between their chemical potentials is unchanged. In contrast, the volume, excluded to the large Ficoll 400 molecules, differs much more in the open and closed state. Accordingly, a concentration dependent stabilization of closed conformations is expected in a crowded environment.

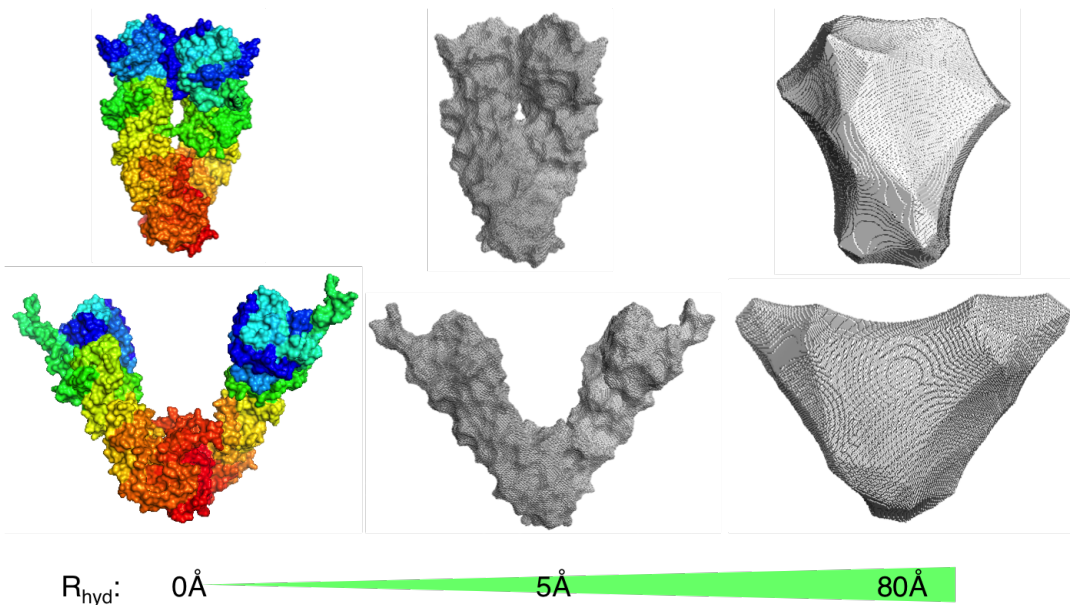


Figure 12.8: A closed (top, pdb: 2cg9 [2]) and an open (bottom, [61]) conformation of Hsp90 as viewed by differently sized crowder molecules (R_{hyd} , hydrodynamic radius). Excluded volumes (gray) were calculated for sucrose and Ficoll 400 using the 3V tool [157]. Van der Waals volumes are shown in colors.

Consistently, macromolecular crowding (by Ficoll 400) at typical intra-cellular concentrations led to a stabilization of closed conformations, while equal densities of sucrose did not. On the other hand, the additional stabilization of open conformations by 30wt% sucrose is rather caused by Brownian bombardment from the *inside* and interference with cross-protomer contacts. Furthermore, the viscous environment dampened fast fluctuations on the sub-100ms timescale, whereas slower transitions were only weakly affected. In this regard, it would be interesting to know which density is required to completely suppress those transitions.

Cause or coincidence? This is the question concerning the observed ATPase rate amplification by macromolecular crowding. It is well known that a closed conformation represents the enzymatically active state of Hsp90. But is a purely physical stabilization of *any* closed conformation enough to amplify Hsp90's notoriously slow ATPase rate?

In fact, causative *chemical* interactions with the crowder are very unlikely, because the effect was not observed under equal densities of sucrose. Moreover, similar findings were recently reported using variably sized PEG, too [58]. Therefore, it appears indeed that a very nonspecific destabilization of the open state is enough to promote the hydrolysis competent state. This is in line with the current notion that conformational changes - and not the hydrolysis itself, nor nucleotide release - are limiting for Hsp90's slow ATPase rate [134]. Nevertheless, such a nonspecific stimulation was not expected for Hsp90.

Obviously, this has far reaching consequences for the interpretation of *in vitro* results with respect to the situation *in vivo*. Specifically, it could explain some of the discrepancies between the effectivity of Hsp90 inhibitors *in vivo* and their affinity measured *in vitro* [25]. Finally, it demonstrates that Hsp90's function is very susceptible to nonspecific manipulation, which supports the notion that merely the cochaperones convey specificity to Hsp90's function *in vivo* [149, 137, 77].

12.2 DEPENDENCE ON MONOVALENT CATIONS

Intramolecular interactions of proteins depend strongly on the ionic strength of their environment. Consequently, a systematic salt screen can provide valuable information on critical interactions and their driving force. To this end, Hsp90's conformational dynamics were analyzed under varied monovalent cation concentrations, including potassium¹ and sodium².

The fraction of Hsp90 in closed conformations was further decreased by increasing salt concentrations (Figure 12.9a). The effect was abolished by ADP binding (Figure 12.9b). Interestingly, the trend towards prevalence of open conformations was less pronounced for equal *sodium* concentrations (Figure 12.9c).

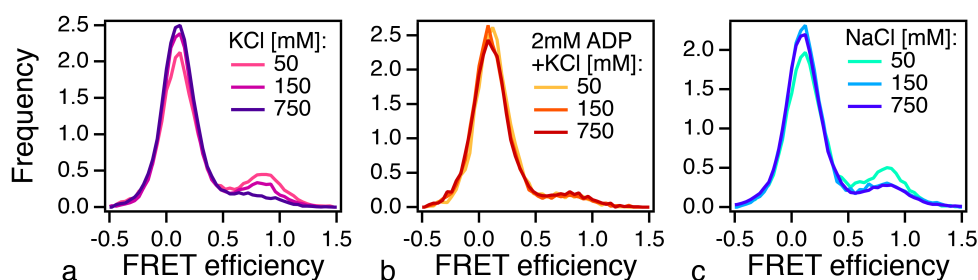


Figure 12.9: Cation dependence of Hsp90's conformations: varied potassium chloride concentrations (a) including ADP (b) or varied sodium chloride concentrations (c) as specified.

The associated transition rates between open and closed conformations were deduced by SMACKS. Figure 12.10a shows that in addition to the observed population shift, also the rates grow gradually with increasing potassium concentrations. Conversely, no significant change is observed under equal sodium concentrations (Figure 12.10b).

Although all shifts are small, they occurred consistently upon buffer change. For example the data at 150mM KCl was measured after that at 750mM KCl. Nevertheless, it agrees well with an earlier data set at corresponding conditions ("prev. 150" in Figure 12.10a).

In summary, the energy barriers between Hsp90's conformations shrink gradually under increasing KCl concentrations. Consistently, the total number of transitions grows for increasing potassium - but not sodium - concentrations (cf. Figure 12.10d).

Interestingly, Hsp90's ATPase activity grows \approx 3-fold with increasing potassium or sodium concentrations between 50mM and 1M (Figure 12.11). Notably, this salt-dependence was consistently found for 3 individual Hsp90 constructs. So, for the first time herein, the accelerated ATPase function does *not* correlate with prevalence of closed conformations.

1 40mM HEPES potassium salt, 10mM MgCl₂, KCl as specified, pH 7.5 by HCl

2 40mM HEPES (anhydrous), 10mM MgCl₂, NaCl as specified, pH 7.5 by NaOH

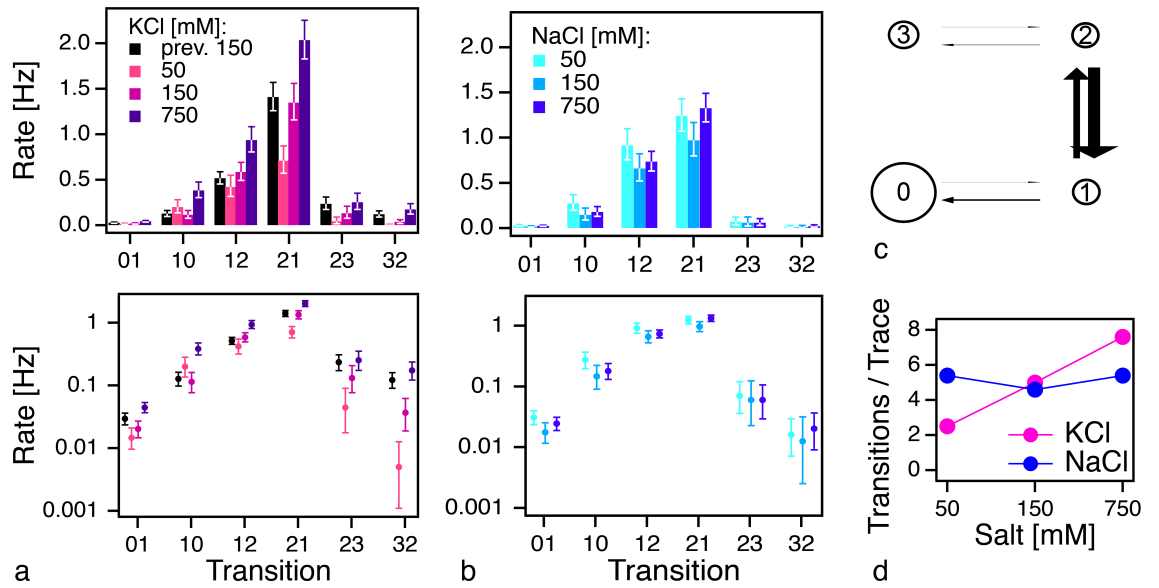


Figure 12.10: Dissimilar cation dependence of Hsp90's kinetics under varied potassium (a) or sodium (b) concentrations. The rates are labeled according to the state model in (c). State 0,1: low FRET; state 2,3: high FRET. (d) The average number of transitions observed per trace for all data sets.

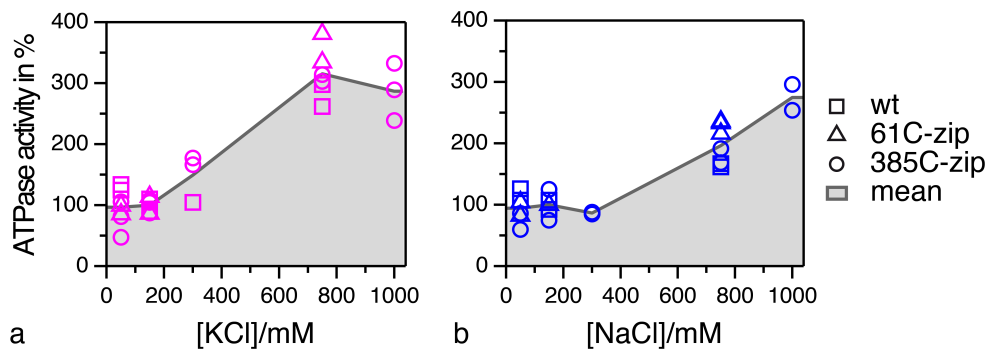


Figure 12.11: Hsp90's ATPase activity under varied cation conditions: (a) KCl, (b) NaCl as specified. All buffers contained 10mM $MgCl_2$. Measurements were performed with 3 different Hsp90 variants: wild-type (wt), 61C with C-terminal zipper (zip) and 385C with C-terminal zipper. Individual rates were normalized to the value obtained using 150mM mono-valent cation. I.e. for KCl: 0.8 / 0.8 / 0.7 ATP/min/monomer; for NaCl: 1.2 / 0.7 / 0.4 ATP/min/monomer (in the above order). The measurement protocol is found in [Section B.2](#).

12.2.1 Discussion

The equilibrium shift towards open conformations under high salt conditions could be caused by screening of polar cross-protomer interactions. In addition, stabilized, hydrophobic intra-protomer interactions could also explain the destabilization of closed conformations.

Interestingly, the more pronounced effect observed for potassium as compared to sodium ions matches the Hofmeister trend, i.e. stronger hydrophobic interaction under the larger - *kosmotropic* - cation [43].

In this context, it is not surprising that Hsp90's ATPase activity is affected by monovalent cations. The observed effect on the ATP hydrolysis rate is in line with earlier results for potassium chloride [134]. But corresponding information on sodium chloride was not previously available.

In particular, it was unclear whether sodium would cause a similar effect, as differing results were reported concerning other GHKL ATPases: maximal ATPase activity was previously found in the presence of sodium for MutL [69], whereas for DNA gyrase, higher activity was found in the presence of potassium [60].

Further differing effects were found regarding Hsp90-client interactions. A concentration dependent increase of the Hsp90-glucocorticoid receptor association was observed in the presence of potassium ions - but not sodium ions [71].

12.3 SUMMARY 5

Hsp90's closed conformations are stabilized by macromolecular crowding, but not by small-molecular viscosogens. Interestingly, this nonspecific effect is accompanied by an increase in ATPase activity. This is similar to previously discussed results (cf. [Section 11.1](#), [Section 11.3](#)), thus assigning an off-state character to the open conformations.

These open conformations were further stabilized by increasing salt concentrations. In agreement with the Hofmeister series, a more pronounced effect was observed for potassium as compared to sodium. Besides, potassium caused generally faster dynamics in the range of 200ms to many seconds, indicating overall lowered energy barriers. As the only recognized exception to the off-state statement above, here, the ATPase activity does *not* correlate with prevalence of closed conformations. Actually, the hydrolysis rate is accelerated by increasing concentrations of both cations.

OUTLOOK: VARIOUS TIMESCALES

Interestingly, Hsp90's N-terminal conformational dynamics occur on a broad range of timescales. Dwells from 20ms to 100s were observed by TIRF. [Figure 13.1](#) shows the dwell time distributions measured using varied sampling rates.

To test for a comprehensive kinetic behavior, the distributions were fit globally. The low-FRET distributions (describing N-terminal closing) were only badly fit by bi-exponential functions (with global time constants 0.2s and 5.2s), with no further improvement using tri-exponentials. A similar fit is achieved using a power law (power = -0.24) with only half of the fit coefficients. For the high-FRET distributions (describing N-terminal opening), a comparatively better fit is found using a tri-exponential function (time constants: 1.4s, 0.4s and 27.0s), whereas the power law fits less well (power

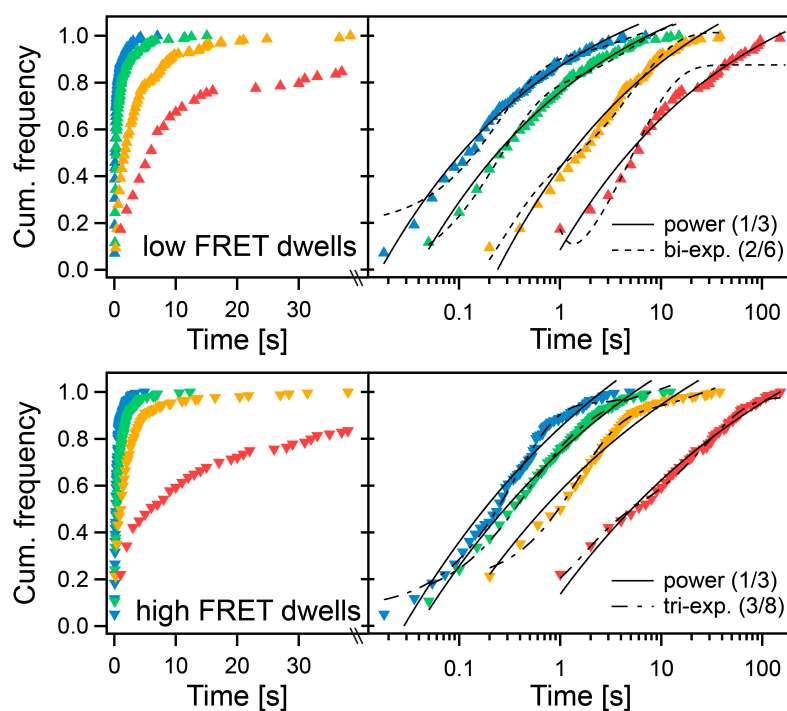


Figure 13.1: Dwell time distributions of Hsp90's large opening and closing transitions in the presence of 2mM ATP, measured at 4 sampling rates: 55Hz, 20Hz, 5Hz, 1Hz in blue, green, yellow, red. The slower 2 measurements were performed in ALEX-mode. The faster 2 were only experimentally feasible under continuous green excitation. Notably, distributions at individual sampling rates are interconvertible by *post-hoc* data down-sampling (see [Section A.7](#)). The full range of the data is better visible in logarithmic scale (right). Global fits are displayed as indicated. The number of parameters are specified as: (linked/total).

-0.17). Qualitatively, all distributions are well fit by *individual* bi-exponential, but not single-exponential functions.

A central assumption in this work was that Hsp90's kinetics can be described by individual states and transitions between discrete, well defined energy minima. Yet, this may be an over-simplified assumption regarding protein kinetics [125, 36]. Instead, power laws have been previously applied to describe diffusive processes on a rough energy landscape [164, 158].

On the other hand, it was extensively discussed herein that the inherently narrow detection bandwidth of the smFRET experiment has a large, artificial impact on plain dwell-time distributions. In fact, an earlier probabilistic weighting ansatz to merge dwell-time distributions obtained with different sampling rates [129] was tested by simulations and found valid for particular parameter sets (sampling, transition and bleach rates), only. Nevertheless, experiments at varied sampling rates clearly provide additional information on the studied system. Therefore, the ultimate goal is to combine the information of experiments covering a wide range of timescales *ex post*, in one comprehensive time trace analysis. But the implementation of such a comprehensive analysis is less clear. Parameter optimization in *continuous* time seems to be necessary but not sufficient for that task.

In the future, alternative experimental approaches may provide a wider detection bandwidth than TIRF in the first place. Especially, techniques that are independent of photo-bleaching, have the potential to overcome this barrier. Electronic detection could become an alternative, e.g. using single molecule field effect transistor (smFET) devices [144, 27, 28, 18]. Currently, however, the plus in detection bandwidth comes still at the cost of reduced specificity. Also the sensitivity due to the r^{-6} -dependence of FRET is hard to beat.

CONCLUSION

smFRET was used herein to reveal conformational changes in real time. Thereby, different conformations are characterized by individual distances between selected (dye) positions in the protein.

The precision and accuracy of FRET efficiency derived distances was assessed in a world-wide blind-study. Specifically, a distance uncertainty of 3\AA - i.e. below 1 basepair - was found for a dsDNA sample and distances near the Förster radius.

Further critical evaluation of the potentials and limits of smFRET and related analysis procedures, led to the development of the single molecule analysis for complex kinetic sequences (SMACKS). It exploits the unique capability of single molecule time traces to track the time evolution of an individual molecule through distinct, conformational states. This allows to quantify energetic aspects that are not accessible by ensemble studies.

SMACKS is a maximum-likelihood approach that infers *one* kinetic state model - including all relevant transition rates - based on a large set of time traces. Thereby, it eliminates previous dwell-time related artifacts, in particular the systematic and non-linear overestimation of transition rates. Effectively, this represents a *post-hoc* enlargement of the inherently narrow detection bandwidth of smFRET, which is caused by photo-bleaching. In addition, SMACKS reveals kinetic heterogeneity, and it includes multiple ways of model evaluation. SMACKS was demonstrated using the example of Hsp90 and its complex conformational dynamics.

Hsp90's N-terminal opening and closing transitions were found to occur throughout the accessible range of timescales from milliseconds to minutes. Importantly, they are largely independent of a chemical energy source, such as ATP. In fact, regardless of the presence or absence of ATP, the observed kinetics are best described by a 4-state model with 2 distinct open and 2 distinct closed states. Even under ATPase stimulation by the cochaperone Aha1, the kinetics remain in thermal equilibrium. Moreover, neither competitive ATPase inhibitors (radicol, geldanamycin, PU-H71), nor an allosteric, C-terminal drug candidate (KU32) had a drastic effect on these conformational dynamics or their steady-state.

Apart from AMP-PNP, which inverts Hsp90's steady-state from mainly open to mainly closed conformations, two more conditions had notable impact on Hsp90's conformational kinetics. Interestingly, one is very site specific - the point mutation of residue 577 - whereas the other one is entirely non-specific - macromolecular crowding. The former suggests C-terminal stiffening with far-reaching effects up to the N-domains. The latter indicates that caution is advised when relating *in vitro* findings to *in vivo* function.

In many cases (e.g. Aha1 stimulation, 577I mutation, macromolecular crowding), increased ATPase activity correlates with an increased population of

closed conformations. Yet, the differing salt dependence of both - ATPase activity and closed population - proves that this is not a general rule. Hsp90 showed increasing ATPase activity under increasing salt concentrations (NaCl, KCl), accompanied by a trend towards more open conformations.

So concerning Hsp90, the emerging picture is that of a very flexible dimer that relies critically on external assistance.

For example, Hsp90's ATPase function requires the concerted action of the N-terminal nucleotide binding pocket with distant elements, such as the catalytic loop of the middle domain and even parts of the opposite N-domain. These elements, however, are very flexible, such as the entire dimer. Consequently, *anything* that constrains this flexibility and confines Hsp90 in a more compact conformation, has the potential to increase the coupled probability for such a concerted action - be it by specific or non-specific interaction.

This notion can be further extended to cochaperone binding and it also implies mutual effects upon client interaction. Therefore, it seems that although Hsp90's flexibility may facilitate its diverse interactions, the flexibility itself has a substantial off-state character regarding ATP hydrolysis.

In conclusion, this work presents multifarious examples of the dynamic structure - function relationship in Hsp90, providing valuable clues to the molecular working principle of this chaperone in particular, and in a broader sense, to proteins in general.

APPENDIX

SUPPORTING INFORMATION

A.1 DERIVATION OF FUNDAMENTAL LIMITS

In realistic TIRF experiments, the following assumptions apply:

- no fluorophore saturation (cf. [Section A.2](#))
- stochastically independent sources of noise
- negligible laser-independent noise

A.1.1 Time Resolution

The hardware limit for maximal time resolution depends on the utilized detector. For EMCCD cameras - currently the most frequent detector for smFluo time traces - the maximal frame rate is less than 60 Hz. Higher sampling rates are achieved by cropped chip exposure or using alternative detectors, such as s-CMOS cameras or even APDs.

On the other - *long* - end of the time window, an extended observation time is desirable for kinetic analysis. This limits the applicable laser powers in the experiments to levels below fluorophore saturation. Consequently, the intensities of excitation and fluorescence scale linearly, and so does the time constant of photo-bleaching (see below).

Thus, within the experimentally relevant regime, the following statements in units of time Δt remain general - independent of the actual sampling rate.

A.1.2 Observation Time

A typical organic fluorophore emits a few million photons before irreversible photo-bleaching [130, 167]. Because these dyes have a high fluorescence quantum yield, also the mean of the exponentially distributed total number of excitation/de-excitation cycles $\hat{N}_{\text{cycles}}^{\text{tot}} \approx 10^6$.

In the absence of fluorophore saturation, the time constant of bleaching in units of time Δt is given by:

$$\tau_{\text{bl}} = \frac{\hat{N}_{\text{cycles}}^{\text{tot}}}{n_{\text{cycles}}} = \frac{\hat{N}_{\text{cycles}}^{\text{tot}}}{\epsilon_{\text{ex}} \cdot n_{\text{ph}}^{\text{ex}}} \quad (\text{A.1})$$

where n_{cycles} is the number of excitation cycles per Δt , which is determined by the excitation quantum yield ϵ_{ex} and the number of excitation photons per Δt , $n_{\text{ph}}^{\text{ex}}$. The latter is linked to P_{Laser} , the incident laser power at the sample, and the photon energy $h\nu$ by:

$$n_{\text{ph}}^{\text{ex}} = P_{\text{Laser}} \cdot \frac{\Delta t}{h\nu}$$

A.1.3 Signal-to-Noise Ratio

The signal-to-noise ratio (SNR) is defined as the mean number of signal photons $n_{\text{ph}}^{\text{sig}}$ per standard deviation of the noise $\sigma_{\text{ph}}^{\text{noise}}$:

$$\text{SNR} = \frac{n_{\text{ph}}^{\text{sig}}}{\sigma_{\text{ph}}^{\text{noise}}} \quad (\text{A.2})$$

In TIRF experiments, the number of signal photons per Δt is defined as the difference between detected photons $n_{\text{ph}}^{\text{det}}$ and background photons $n_{\text{ph}}^{\text{bg}}$. It is further determined by $n_{\text{ph}}^{\text{ex}}$, ϵ_{ex} , the fluorescence quantum yield η_{fl} and the detection sensitivity δ_{sens} . Below, the later constants are summarized in C_{sig} .

$$n_{\text{ph}}^{\text{sig}} = n_{\text{ph}}^{\text{det}} - n_{\text{ph}}^{\text{bg}} = n_{\text{ph}}^{\text{ex}} \cdot \epsilon_{\text{ex}} \cdot \eta_{\text{fl}} \cdot \delta_{\text{sens}} = n_{\text{ph}}^{\text{ex}} \cdot C_{\text{sig}}$$

The dominating noise sources are classified into laser-dependent noise including auto-fluorescence, Raman scattering and shot-noise, on the one hand, and on the other hand, laser-independent noise, such as detection noise originating from read-out, dark-current and the analog-to-digital converter (ADC), or additional noise (e.g. from dust). The total noise level of these stochastically independent noise sources is given by the root sum of the respective variances (in the above order):

$$\sigma_{\text{ph}}^{\text{noise}} = \sqrt{n_{\text{ph}}^{\text{ex}} \cdot c_{\text{autofl}} + n_{\text{ph}}^{\text{ex}} \cdot c_{\text{scat}} + n_{\text{ph}}^{\text{ex}} + \rho_{\text{det}} + \beta}$$

Furthermore, it is known from TIRF experiments that laser-dependent noise is by far dominating leading to the approximation:

$$\sigma_{\text{ph}}^{\text{noise}} \approx \sqrt{n_{\text{ph}}^{\text{ex}} \cdot c_{\text{autofl}} + n_{\text{ph}}^{\text{ex}} \cdot c_{\text{scat}} + n_{\text{ph}}^{\text{ex}}} \approx \sqrt{n_{\text{ph}}^{\text{ex}}} \cdot C_{\text{noise}}$$

And Equation (A.2) becomes:

$$\text{SNR} = \sqrt{n_{\text{ph}}^{\text{ex}}} \cdot \frac{C_{\text{sig}}}{C_{\text{noise}}} \quad (\text{A.3})$$

A.1.4 Consequences

Finally, combining Equations (A.1) & (A.3) results in:

$$\tau_{\text{bl}} = \frac{\hat{N}_{\text{cycles}}^{\text{tot}}}{\epsilon_{\text{ex}} \cdot \text{SNR}^2} \cdot \left(\frac{C_{\text{sig}}}{C_{\text{noise}}} \right)^2 = \frac{\text{const}}{\text{SNR}^2}$$

It is worth noting, that by eliminating $n_{\text{ph}}^{\text{ex}}$, we also got rid of Δt and P_{Laser} . Consequently, the relation between τ_{bl} and SNR depends exclusively on fluorophore-specific constants ($\hat{N}_{\text{cycles}}^{\text{tot}}$, ϵ_{ex} , η_{fl}) and setup-specific constants (δ_{sens} , C_{noise}).

Similar findings were published by Greenfield *et al.* [57], who performed systematic simulations where the accuracy of the resolved rates depended primarily on the number of transitions per trace, which is a function of τ_{bl} . In contrast to the present derivation, that work considers the product of $\text{SNR} \cdot \tau_{\text{bl}}$ to be constant, which would convert to a questionable $\text{SNR} \propto n_{\text{ph}}^{\text{ex}}$ (instead of $\text{SNR} \propto \sqrt{n_{\text{ph}}^{\text{ex}}}$).

A.2 TIRF SETUP CHARACTERIZATION

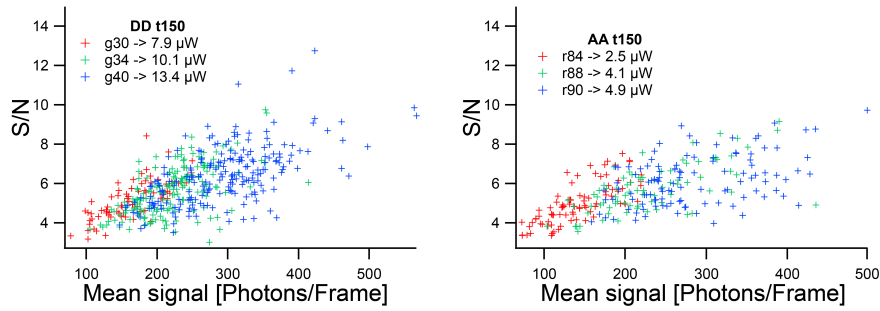


Figure A.1: SNR of individual dsDNA-coupled dyes under 3 distinct excitation powers. DD: Atto550 excited at 532nm (left); AA: Atto647N excited at 635nm (right). Signal in mean photons per frame detected by the EMCCD.

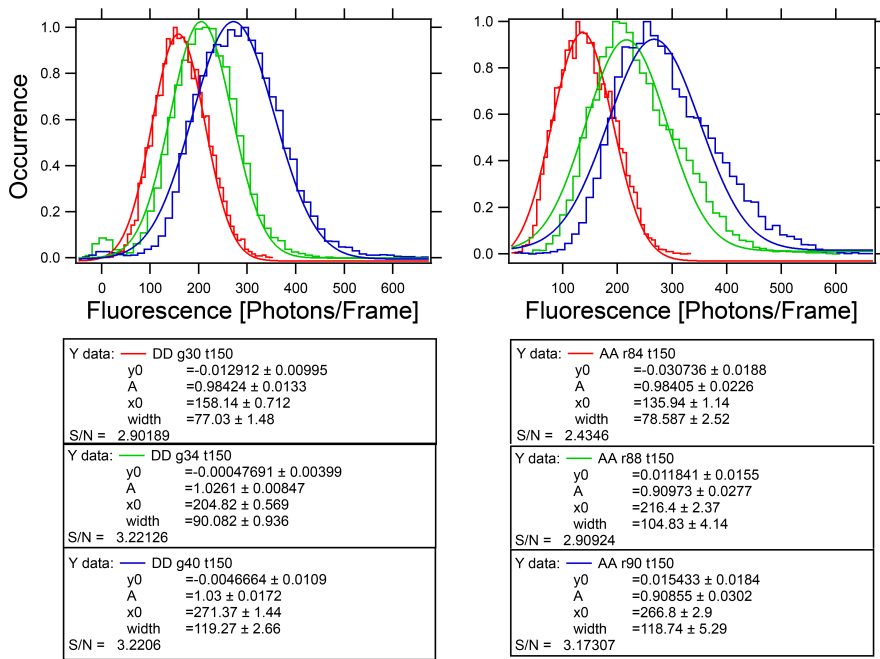


Figure A.2: Distribution of the fluorescence of individual molecules under 3 distinct excitation powers. Coefficients of the Gaussian fits are stated below.

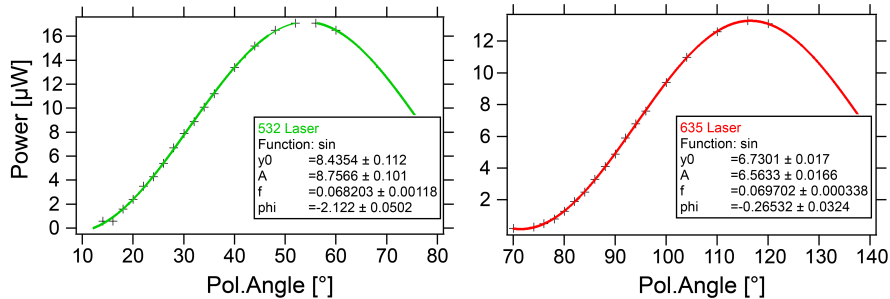


Figure A.3: Calibration curves of the laser power as a function of the angular orientation of the half-wave plate.

A.3 THE EFFECT OF NOISE AND BIAS ON FRET EFFICIENCIES

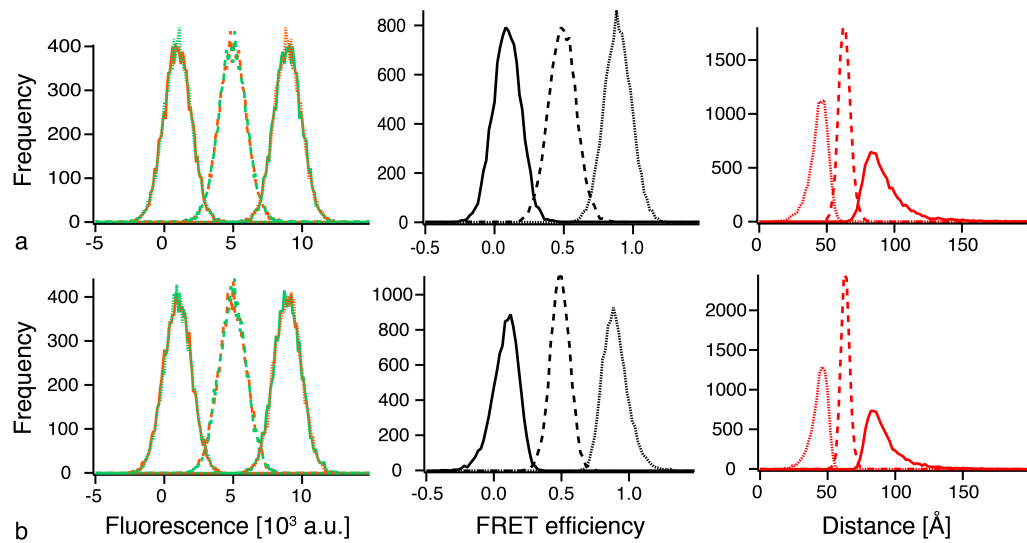


Figure A.4: The effect of fluorescence signals (donor green, acceptor orange) with correlated (a) or uncorrelated (b) fluorescence noise on FRET efficiency and distance distributions. Distributions for $E = 0.1, 0.5, 0.9$ are shown in corresponding line styles. Similar to experiments, the average total fluorescence signal was 10^4 a.u. and $R_0 = 64\text{\AA}$. Gaussian noise was applied to fluorescence signals with $\sigma_{\text{noise}} = 10^3$.

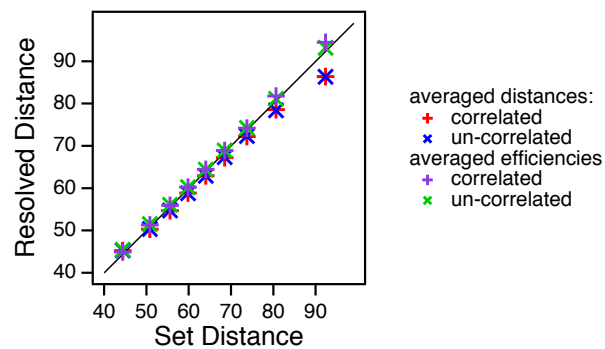


Figure A.5: Distance vs. FRET E averaging under correlated or uncorrelated noise, as indicated. Values represent Gauss positions from fits to FRET E or distance distributions. Distributions as in [Figure A.4](#).

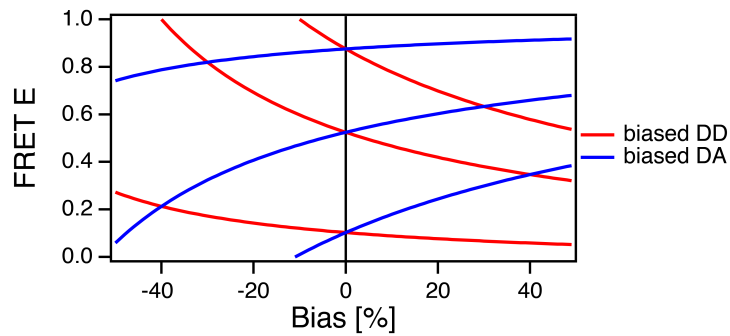


Figure A.6: The effect of biased fluorescence signals on three different FRET efficiencies (unbiased $E = 0.1, 0.52, 0.88$). Simulated positive or negative bias of the donor (or acceptor) signal after donor excitation, DD (or DA), is specified in percent of the total intensity, DD + DA. DD over-estimation may be caused by γ over-estimation. It generates the behavior observed in [Section 8.2.5](#): growing under-estimation with increasing FRET efficiencies.

A.4 SUPPORTING DATA ON SMACKS

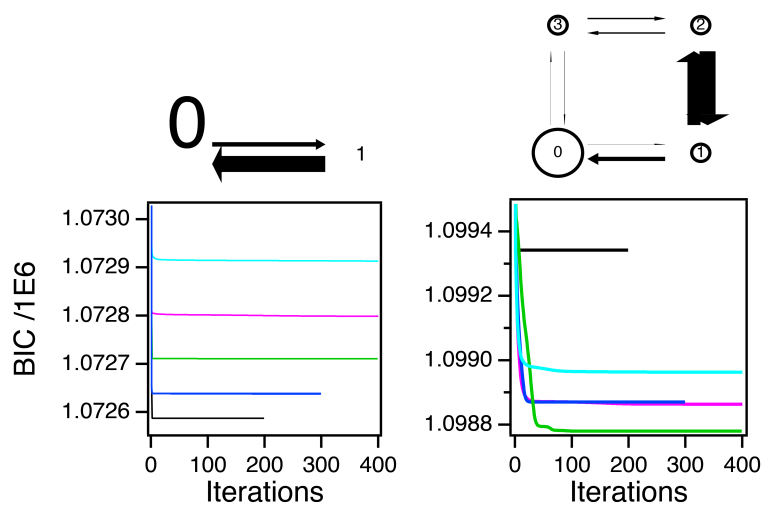


Figure A.7: In the context of SMACKS, BIC detects the correct size of the input model from synthetic smFRET time traces: (left) 2 states, 0: low FRET; 1: high FRET. (right) 4 states with degenerate FRET efficiencies for states 0,1: low FRET; 2,3: high FRET. Color code: 2,3,4,5,6 states in black, blue, green, pink, cyan, respectively. Input and output values are specified in [Table A.1](#).

Table A.1: Comparison of simulation input and SMACKS output of the transition probabilities corresponding to [Figure A.7](#). Left, 2 state model; right, 4 state model.

transition	input	output
10	2.90E-02	3.33E-02
30	3.50E-03	3.64E-03
01	3.20E-03	2.92E-03
01	8.30E-03	8.18E-03
10	2.90E-02	2.88E-02
21	1.39E-01	1.22E-01
12	8.30E-02	1.00E-01
32	1.00E-02	1.18E-02
03	7.00E-04	9.62E-04
23	1.20E-02	1.16E-02

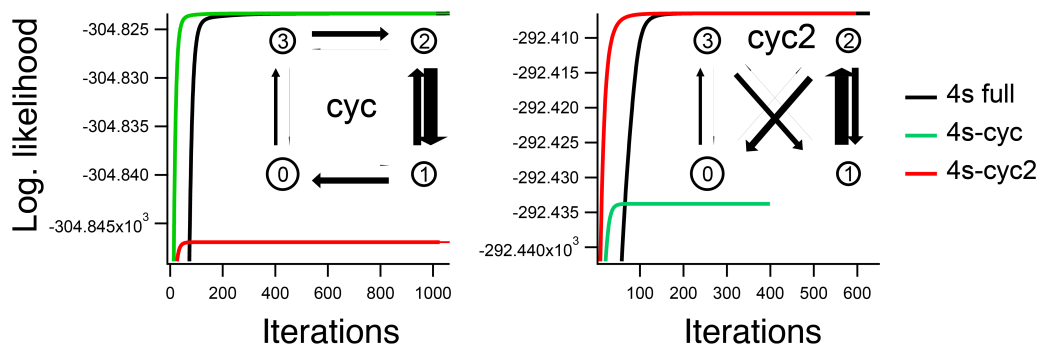


Figure A.8: Correct minimal state models inferred by SMACKS applied to synthetic smFRET time traces. The input models termed *cyc* and *cyc2* are depicted as insets. The 4 states come with degenerate FRET efficiencies: states 0,1: low FRET; states 2,3: high FRET. The corresponding minimal model generates equal likelihood as the complete 4-state model with 12 links (full). Input and output values are specified in [Table A.2](#).

Table A.2: Comparison of simulation input and SMACKS output of the transition probabilities corresponding to [Figure A.8](#). Left, *cyc* model; right, *cyc2* model.

transition	input	output	transition	input	output
10	1.00E-01	8.33E-02	20	1.00E-01	1.02E-01
30	1.00E-06	3.15E-03	30	1.00E-06	1.06E-25
01	2.50E-05	1.70E-35	21	1.00E-01	1.03E-01
21	2.00E-01	1.83E-01	31	8.00E-02	7.96E-02
12	1.00E-01	1.04E-01	02	2.50E-05	1.23E-12
32	8.00E-02	7.58E-02	12	2.00E-01	2.08E-01
03	5.00E-02	4.67E-02	03	5.00E-02	4.98E-02
23	3.00E-06	4.11E-10	13	3.00E-06	5.33E-12

A.5 CONTROL OF HSP90'S DYNAMICS USING ALTERNATE DYE POSITIONS

The general nucleotide-specific effects were reproduced using varied dye positions. Specifically, donor and acceptor dyes were both attached to cysteins at position 452 of opposing monomers¹. The peak positions are of course shifted with respect to those obtained with the dyes attached to positions 61 and 385. In particular, the peaks are less well separated along the new reaction coordinate. Also, a slightly larger high-FRET population is observed in the presence of ATP compared to ADP or *apo*. But consistent with the previous results, Hsp90 populates predominantly the open conformation. Except in the presence of 5'-adenylyl- β - γ -imidodiphosphate (AMP-PNP), where mainly the closed conformation is populated.

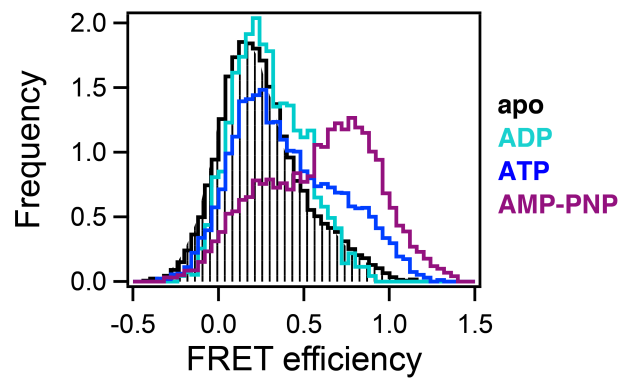


Figure A.9: Similar nucleotide dependence of the conformational population distribution is observed with varied dye positions: 452C, 452C.

¹ The Hsp90-452C mutant was a kind gift of Philipp Wortmann.

A.6 HSP90 INHIBITORS

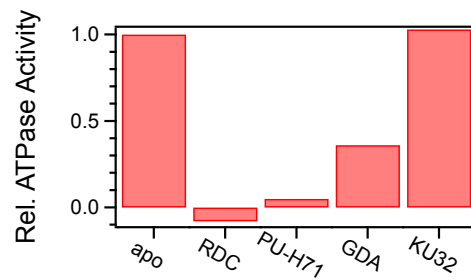


Figure A.10: Inhibition of Hsp90's ATPase activity by 4 compounds representing the main classes of current Hsp90 related anti-cancer drug candidates. See [Section B.2](#) for the ATPase assay protocol. 2 μ M Hsp90-61C (without zipper, reduced by 1mM TCEP) was used for reference (apo). The small background activity observed in the presence of 5 μ M radicicol (RDC) was subtracted from all values. All inhibitors were applied without previous incubation. 80 μ M PU-H71 and 70 μ M geldanamycin (GDA) were used. Measurement of the latter is impaired by the individual absorption of this yellow compound at 340nm. The c-terminal inhibitor KU32 did not show inhibition at 12.5 μ M.

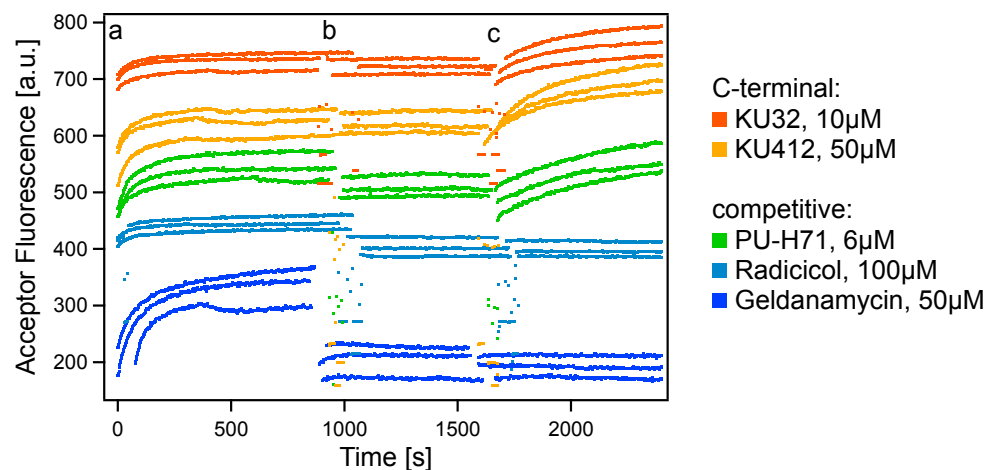


Figure A.11: Ensemble FRET experiment using Hsp90-61C-Atto550 and Hsp90-385C-Atto647N (both without c-terminal zipper). (a) Hetero-dimers form upon mixing, leading to an increase in acceptor intensity. (b) Inhibitor was added as indicated. (c) 2mM AMP-PNP further stabilizes Hsp90's closed conformation in the presence of the C-terminal inhibitors (KU32 and KU412), whereas low concentrations of competitive inhibitors (radicicol, geldanamycin) interfere with AMP-PNP binding. Interestingly, PU-H71 was outcompeted by 300-fold excess of AMP-PNP.

A.7 SELF-CONSISTENCY OF DYNAMICS AT VARIOUS TIMESCALES

To test if the measured distributions are consistent with each other - especially regarding ALEX and non-ALEX experiments in [Chapter 13](#) - the raw data was re-evaluated after *post-hoc* down-sampling from 20Hz to 5Hz. See [Figure A.12](#).

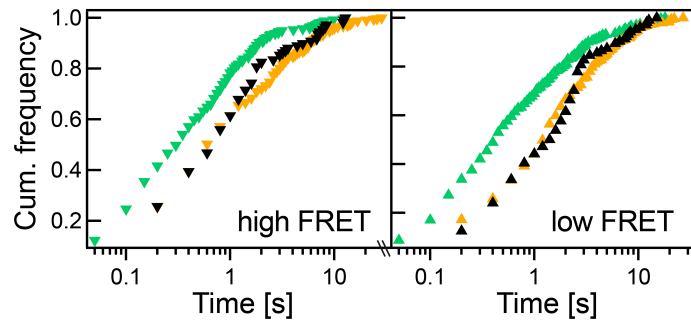


Figure A.12: Post-hoc downsampling of smFRET time traces demonstrates the self-consistency of the dwell-time distributions obtained at different sampling rates: 20Hz, green; 5Hz ALEX, yellow; down sampled from 20 to 5Hz, black.

MATERIALS & METHODS

If not stated differently, all chemicals were purchased from Sigma Aldrich.

B.1 BIOCHEMICAL PREPARATION

B.1.1 *Molecular Biology*

The Hsp90 construct used herein was introduced in [Chapter 7](#). The specific sequence is found in [Figure B.1](#). Previously published cysteine positions [64] allowed for specific labeling with donor (61C) or acceptor (385C) fluorophores (see below). Both constructs were cloned into a pET28b vector (Novagen, Merck Biosciences). They include an N-terminal His-tag followed by a SUMO-domain for later cleavage. The QuickChange Lightning kit (Agilent) was used to insert an Avitag for specific *in vivo* biotinylation at the C-terminus of the acceptor construct. *E.coli* BL21star cells (Invitrogen) were transformed with pET28b by electroporation (Peglab). For *in vivo*-biotinylation, the cells were further transformed with pBirAcm (Avidity) in a second electroporation step.

B.1.2 *Hsp90 Expression, in vivo Biotinylation & Purification*

The donor construct was expressed in *E.coli* BL21(DE3)cod+ (Stratagene) for 3h at 37°C after induction with 1mM IPTG at $OD_{600}=0.7$ in LB_{Kana} .

For *in vivo* biotinylation, 2l expression media (2l TB medium, 2ml 20mg/ml kanamycin only, 40 ml of filter-sterilized 20% glucose solution, (0.5% final conc.)) were inoculated with 50ml overnight culture (50 ml LB medium, 50 μ l kanamycin, 10 μ l chloramphenicol, 37°C and shaking), grown at 37°C while shaking until $OD_{600}=0.7$.

In both cases, a cell disruptor (Constant Systems Ltd.) was used for lysis. Proteins were purified as published [74]. The main chromatography steps were Ni-NTA (hisTrap, GE Healthcare) followed by SUMO cleavage, anion exchange (hiTrap Q, GE) and size exclusion (Superdex 200, GE). 95% purity was confirmed by SDS-PAGE.

B.1.3 *Fluorescent labelling & monomer exchange*

Fluorescent labels (Atto550-, Atto647N-maleimide) were purchased from Atto-tec and coupled to cysteins according to the supplied protocol. Hetero-dimers (acceptor+donor) were obtained by 20min incubation of 1 μ M donor, 0.1 μ M biotinylated acceptor homo-dimers and 2mM ADP in measurement buffer (40mM HEPES, 150mM KCl, 10mM $MgCl_2$) at 47°C. In this way, predominantly biotinylated *hetero*-dimers bind to the neutravidin (Thermo Fisher) coated fluid chamber (see below). (Residual homo-dimers will show a specific smFRET signal and are excluded from analysis.)

```

ATGGGT CATA TGGGTAG CAG CCATCATCA CACCATCAG GTTCTGGT CT GGTTCCT CGT
GGATCAGCAA GCATGAG CGA TAGTGAAGTG AATCAAGAGG CCAAA CCTGA GGT TAAACCG
GAAGT CAAAC CGGAAACCCA CATCAACCTG AAAGTGT CTG ACGGTAGCAG TGAAATCTTC
TTCAAATCA AAAAAACCA CCCGCTGCGT CGTCTGATGG AGGCATTTGC CAAACGTCAA
GGCAAAGAGA TGGATAGCCT GCGTTTTCTG TATGACGGGA TCCGTATTCA GGCAGATCAA
ACGCCCTGAGG ATCTGGATAT GGAGGATAAC GACATCATCG AAGCCCATCG TGAGCAGATT
GGCGTATGG CTAGTGAAC TTTTGAATTT CAAGCTGAAA TTACTCAGTT GATGAGTTTG
ATCATCAA CA CCGTCTATTC TAACAAGGAA ATTTTCTTGA GAGAA CTGAT ATCTAATGCC
TCGGATGCGT TGGATAAAAT TAGATACAAA TCTTTGTCTG ATCAAAGCA ATTGAAAAA
GAACCAGATC TCTTTATTAG AATCACTCCA AAGCCAGAGC AAAAA GTTTT GGAAATCAGA
GATTC TGGA TTGATGAC CAAGCTGAA TTGATTAATA ACTTGGGTAC CATTGCCAA
TCTGGTACCA AAGCCTT CAT GGAAGCTCTA TCTGCTGGTG CCGATGTATC CATGATTTGGT
CAATT CCGTG TTGTTTTT TA CTCTTATTC TTAGTTG CCG ACAGAGTTCA GGT TATTTCA
AAGAGCAA CG ACGACGAA CA ATACATCTGG GAATCCAACG CTGGTGGTTC TTTCACTGTT
ACTCTAGA CG AAGTTAATGA AAGAATTGGT AGGGGTA CCA TCTTGAGGTT ATTCTTGAAA
GATGACCAAT TGGAGTACTT GGAAGAAAAG AGAATAAAG AAGTTATCAA GAGACATCT
GAGTTCGTGG CCTACCCAAT CCAATTAGTC GTCACCAAGG AAGTTGAAA GGAAAGTTCCA
ATTCCAGAAG AAGAAAAGAA AGACGAGGAA AAGAAGGATG AGGAAAAGAA GGATGAAGAC
GA CAAGAAAC CAAAATTGGA AGAAGTCGAT GAAGAAGAGG AAAAGAAC CC AAAGACGAAA
AAAGT TAAAG AAGAAGTTCA AGAGATAGAA GAACTAAACA AGACTAAG CC TTTGTGGACT
AGAAA CCCAT CTGATATCAC TCAAGAAGAA TACAATGCTT TCTATAAGTC TATTTCAAAC
GACTGGGAAG ACCCATTGTA CGTTAAGCAT TTCTCCGTTG AAGGTCAATT GGAATTTAGA
GCTATCTTAT TCATTTCCAAA GAGAGACCA TTCGACTTGT TTGAGAGTAA AAAGAAGAG
AATAATATCA AGTGTACGT TCGTCTGTTT TTCACTCACTG ATGAAGCTGA AGACTTGATT
CCAGAGTGGT TATCTTT CGT CAAGGGTGT TTGACTCTG AGGATTTA CC ATTTGAATTTG
TCCAGAGAAA TGT TACAATTC TAATAAGATC ATGAAGGTTA TTAGAAGAA CATTTGCTAAA
AAGTTGATTG AAGCCTTCAA CGAAATTGCT GAAGACTCTG AA CAATTTGA AAAGTTCTAC
TCGGCTTTCT CCAAAAATAT CAAGTTGGGT GTA CATGAAG ATACCAA AAA CAGGGCTGCT
TTGGCTAAGT TGT TACGTTA CAACTCTACC AAGTCCGTAG ATGAGTTGAC TTCCTTAACT
GATTA CGTTA CCAGAATGCC AGAACACCAA AAGAACATCT ACTACATCAC TGGTGAATCT
CTAAAGGCTG TCGAAAAGTC TCCATTTT TG GATGCTTGA AGGCTAAAAA CTTCGAGGTT
TTGTTCTTGA CCGACCCAAT TGATGAATAC GCCTTCACTC AA TTGAAGGA ATT CGAAGGT
AAAACTTTGG TTGACATTAC TAAAGATTT C GAA TTGGAAG AA ACTGACGA AGAAAAAGCT
GAAAGAGAGA AGGAGATCAA AGAATATGAA CCA TTGA CCA AGGCC TTGAA AGAAATTTG
GGTGA CCAAG TGGAGAAAGT TGTGTTTT CT TACAAATGT TGGATGCC AGCTGCTATC
AGAACTGGTC AATTTGGTTG GTCTGCTAAC ATGGAAAAG TCA TGAAGGC TCAAGCCTTG
AGAGACTCTT CCATGTCCTC CTACATGTCT TCCAAGAAGA CTTTCGAAAT TTCTCCAAA
TCTCCAATTA TCAAGGAATT GAAAAAGAGA GTTGACGAAG GTGGTGTCTA AGACAAGACT
GTCAAGGACT TGACTAAGTT ATTATATGAA ACTGCTTGT TGACTTCCGG CTTCAGTTG
GACGAACCAA CTTCTTTG ATCAAGAAAT AACAGATTGA TCTCTTTGG TTTGAACATT
GATGAGGATG AAGAAACAGA GACTGCTCCA GAAGCATCCA CCGCAGCTCC GGT TGAAGAG
GTTCCAGCTG ACA CCGAAAT GGAAGAGGTA GAT CCCGGG AA CAAAA GC CGAAGAA TGG
AAACGTCGCT ATGAAAAAGA GAAAGAAAAA AACGCGCGCC TGAAAGGCAG AGTGAAAAA
CTGGAAATG AACTGGCGCG TTGGCGCC CCGGAGCCTAG GCGGA GGCCT GAA CGACATC
TTCGAAGCTC AGAAGATTGA ATGGCATGAA TAA

```

Figure B.1: The gene sequence of the Hsp90 construct used herein: 6HisTag, purple; SUMO-domain, blue; start of Hsp90, green; Cys61 and Cys385, orange; end of Hsp90, gray; coiled coil zipper, dark green; AviTag, lime green.

B.2 ATPASE ASSAY

The ATPase activity of Hsp90 was measured in a regenerative assay (0.2mM NADH Di-Na, Roche; 2mM phosphoenol pyruvate K-salt, Bachem; 2 U/ml pyruvate kinase, Roche; 10 U/ml lactate dehydrogenase, Roche) coupled to NADH oxidation, which was followed as a decrease in absorption at 340nm, similar to [150]. Measurements were performed at 37°C in 40mM Hepes, 150mM KCl, 10mM MgCl₂, pH 7.5.

For the measurements under all-sodium or all-potassium conditions, corresponding reagents were used (NADH Di-Na/Di-K, PEP Na/K, ATP Mg-salt) and the above enzymes were dialyzed to the corresponding low salt buffer (40mM Hepes, 10mM MgCl₂, 50mM NaCl/KCl, pH 7.5 by NaOH/KOH). Measurements took place under the same conditions as described, except for varying NaCl/KCl concentrations. Each measurement was followed by radicicol inhibition and addition of excess ADP as a positive control for regeneration.

B.3 FLOW CHAMBER SURFACE PASSIVATION

Coverslips for flow chambers were passivated as follows: 15min sonication in 2% Hellmanex (hellma-analytix), rinse with ultrapure water. Repeat once. Repeat in pure water. 2h incubation in Piranha solution (3 vol. H₂SO₄, 1 vol. H₂O₂) at 60°C, rinse with water. Sonication in 2% Hellmanex as above, rinse with water. 2h incubation in RCA (5 vol. H₂O, 1 vol. H₂O₂, 1 vol. NH₃). Sonication in water as above, rinse with water. 10min incubation in acetone (HPLC grade). 5-10min incubation in 200x Vectabond (Vectorlabs) dilution in acetone. Sway in water for 30s/slide. Application of ca. 40µl of PEG solution (80mg α-methoxy-ω-NHS-ester MW=5000, 3mg Biotin-CONH-PEG-O-C₃H₆-CONHS, MW=3000, both Rapp Polmere, in 600 µl 100mM NaHCO₃), cover with second coverslip. Overnight incubation at a humid & dark place at 8°C. Sway in water for 30s/slide. Blow dry by nitrogen. Store dark & dry.

B.4 HOLLIDAY JUNCTION MEASUREMENTS

DNA-oligos similar to [101] with fluorophores Atto488, Atto550 and Atto647N (Atto-tec) attached were purchased from IBA GmbH. A mixture of 100nM of each DNA-oligo in Tris-buffer (5mM Tris, 5mM NaCl, 20mM MgCl₂, pH 7.5) was heated to 90°C for 10 min and cooled down to 20°C (1°C/min) in a thermocycler (Peqlab). Holliday junctions were measured in Tris-buffer (5mM Tris, 5mM NaCl, 500mM MgCl₂) including 0.1% glucose, 10 U/ml glucose oxidase (*Aspergillus niger*), 100 U/ml catalase (bovine liver, Calbiochem), 2mM Trolox.

B.5 TIRF SETUP COMPONENTS

Table B.1: Components of the smTIRF setup and their manufacturers.

<i>Identifier:</i>	<i>Description:</i>	<i>Specification:</i>	<i>Manufacturer:</i>
532	laser 532 nm	Compass 215M	Coherent
635	laser 635 nm	Lasiris	Stoker Yale
AD	achromatic doublet, f=200	G322-304-000	Qioptic
BI	beam blocker	LB1	Thorlabs
CI	cleanup filter	CL F39-622	ahf Analysentechnik
D1	dichroic mirror		ahf Analysentechnik
D2	dichroic mirror	F53-534	ahf Analysentechnik
D3	dichroic mirror	F33-726	ahf Analysentechnik
D4	dichroic mirror	F33-644	ahf Analysentechnik
EMCCD	electron multiplying charge coupled device	iXonUltra	Andor
F1	notch filter 635	F40-631	ahf Analysentechnik
F2	long pass filter 540	F47-452	ahf Analysentechnik
F3	band pass filter 570	BP F39-572	ahf Analysentechnik
F4	band pass filter 670	BP F37-677	ahf Analysentechnik
Ir	Iris		Thorlabs
L1	plano-convex lens, f=25	LA1951-A	Thorlabs
L2	plano-convex lens, f=1000	LA1779-A	Thorlabs
L3	plano-convex lens, f=500	LA1380-A	Thorlabs
L4	best form silica lens, f=200	G063-005-000	Qioptiq
M	broad band mirror	BB1-E02/BB2-E02	Thorlabs
ND	neutral density filter	NE10A-A	Thorlabs
Obj	objective, NA 1.49, 100x	CFI Apo TIRF 100x	Nikon
PBS	polarizing beam splitter		Thorlabs
Sh	mechanical shutter & controller	SH05, SC10	Thorlabs
SI	optical slit	SP40	Owis
St	translation stage	MT1/M	Thorlabs
$\lambda/2$	half-wave plate	WPMH05M-532, WPMH05M-633	Thorlabs
$\lambda/4$	quarter-wave plate	WPMQ05M-532	Thorlabs

B.6 DESCRIPTION OF SIMULATIONS & THEORETICAL WORK

B.6.1 Kinetic Simulations

Discrete *state sequences* were obtained by a Monte Carlo simulation based on a given transition matrix. Photo-bleaching was included by exponential trace length distributions. For comparison with experimental data, corresponding minimal trace lengths were used (typically 30 data points).

As in the experiment, *synthetic data* contained Gaussian noise ($\sigma = 0.3 \cdot \text{signal}$), random offsets ($\pm 0.2 \cdot \text{signal}$), degenerate FRET efficiencies (two low / two high), a sampling rate of 5Hz and a bleach rate of 0.03Hz. See example data in [Figure 8.13](#).

B.6.2 General Implementation of Semi-Ensemble HMM

In the following, we include all formulae required for the implementation of semi-ensemble HMM as demonstrated herein. For more general introductions to HMM, please refer to the respective literature^{14,15}.

Forward-Backward, Baum-Welch and Viterbi algorithms were implemented for continuous observables and multiple dimensions. Numerical underflow or overflow is prevented by logarithmic renormalization. Recursive calculations are sped up by multi-threading (processing several time-traces in parallel). All software was written in IgorPro v6.3 (Wavemetrics) and calculations were run on an iMac (Apple, 2014, 2.9 GHz Intel i5 processor, 16GB RAM) or a comparable Windows PC. A typical optimization (4 states, >100 traces) took less than an hour.

B.6.3 Expected Value of Observed Energy Coupling

Let $\langle N_{ij}^{\text{obs}} \rangle$ be the expected number of observations for a given transition, in a dataset with N_{tot} data points. If it is smaller than one, the specific transition cannot be resolved. In this case, f_{ij}^{lost} denotes the factor that is actually lost and the expected value of the observed free energy change $\langle \Delta G_{\text{obs}} \rangle$ in units of kT is given by:

$$\langle \Delta G_{\text{obs}} \rangle = - \sum_{\substack{\forall i \neq j \\ (\text{cycl.})}} \ln \left[\frac{a_{ij} / f_{ij}^{\text{lost}}}{a_{ji} / f_{ji}^{\text{lost}}} \right]$$

with:

$$f_{ij}^{\text{lost}} = \begin{cases} \langle N_{ij}^{\text{obs}} \rangle = N_{\text{tot}} \cdot \pi_i \cdot a_{ij} & \forall \langle N_{ij}^{\text{obs}} \rangle < 1 \\ 1 & \forall \langle N_{ij}^{\text{obs}} \rangle \geq 1 \end{cases}$$

B.6.4 Hierarchical Search for Simplified Models

Bruno et al. [19] describe a procedure to deduce the simplest, plausible reaction schemes, from data with multiple open and closed conformations, by comparing models of the canonical "MIR"-form (manifest interconductance rank). We consider a 4-state model with 2 open (o) and 2 closed (c) states ($N_o = N_c = 2$), as previously determined by BIC and the bi-exponential dwell time distributions. First, the interconductance rank (i.e. the number of independent o-c links) is determined. To this end, MIR-form models of rank 1 (linear o-o-c-c) and rank 2

(cyclic -o-o-c-c-) are compared in a likelihood ratio (LR) test (likelihood of rank x model, \mathcal{L}_{R_x}):

$$\text{LR} = 2 \cdot [\ln(\mathcal{L}_{R2}) - \ln(\mathcal{L}_{R1})] \begin{cases} \leq \chi_{0.95,df=2}^2 & \Rightarrow \text{rank 1} \\ > \chi_{0.95,df=2}^2 & \Rightarrow \text{rank 2} \end{cases}$$

The null hypothesis (rank 1 model) is rejected if the likelihood ratio exceeds the 95% confidence interval given by the χ^2 -distribution for 2 degrees of freedom (df). (One missing link equals a difference of two transitions.)

For Hsp90, rank 1 was found under apo, adenosine diphosphate (ADP) and AMP-PNP conditions ($5.99 \gg \text{LR} = 0.07; 0.00; 0.54$; respectively). Whereas in the presence of adenosine triphosphate (ATP) the likelihood ratio indicates rank 2 ($5.99 < \text{LR} = 7.2, 23$ for ATP and ATP+Aha1, respectively).

Second, the number of links N_l within this rank R is determined by comparing different schemes by BIC. The number of mathematically identifiable links is limited:

$$N_l \leq R(N_o + N_c - R)$$

Models with the same rank and the same number of links are mathematically equivalent and cannot be discerned without further experimental data. For Hsp90, we find a cyclic -o-o-c-c- model in the presence of ATP and linear o-o-c-c models for apo, ADP or AMP-PNP conditions. Further information on the interpretation of degenerate state models is given in [19, 48, 4]



α -SYNUCLEIN

Human α -synuclein (gene: SNCA) is a cytosolic, natively unstructured protein of 140 amino acids. In patients with Parkinson's disease, it forms large aggregates of amyloid fibrils. However, these fibrils seem not to be the cause but rather a coincidence of the disease [163]. The current hypothesis is that smaller - less easily visualized - oligomers were rather the toxic form of α -synuclein.

The goal here was to determine oligomer size *distribution* by counting the bleach steps of fluorescently labeled α -synuclein monomers - one oligomer at a time. Such experiments can further recover the oligomerization kinetics (from monomer to oligomer to fibril).

C.1 PREPARATION

α -Synuclein was prepared similar to the protocol of Silvia Campioni of the Riek Lab at ETH Zurich. The pRK172 plasmid was a kind gift of the same lab. It was originally created by M. Goedert from Cambridge UK.

C.1.1 *Material*

- LB_{carb}, IPTG
- resuspension buffer: 50mM Tris, pH 8, 10mM EDTA, 150mM NaCl
- 10% streptomycin sulfate
- glacial acetic acid
- saturated ammonium sulfate: ca. 60g/100ml. (Warm up to dissolve. Cool down again and a precipitate will form.)
- anion exchange (AX) buffer A: 20mM Tris, pH 8
- AX buffer B: 20mM Tris, 1M NaCl, pH 8
- ethanole, pure
- for labeling: PBS, pH 7.5; α Syn is acidic. . .
- standard measurement buffer: 20mM Hepes, 150mM NaCl, pH 7.5

C.1.2 *Expression*

Grow o/n culture of transformed BL21 cells in LB_{carb}. Inoculate 2l of LB_{carb}. At OD₆₀₀ = 0.9-1.0 induce with 1mM IPTG for 4h. Harvest by centrifugation at 4600rpm, 20min (Hettich Rotanta). Resuspend the pellet in resuspension buffer. Disrupt cells with standard French Press protocol.

C.1.3 *Purification*

Place the cell extract on a heat plate at 70°C for 10min. Centrifuge for 30min at 17krpm (Beckmann, JA-17) at 4°C. Collect the supernatant in a clean beaker and add per ml of supernatant: 136 μ l of the streptomycin sulfate solution and 228 μ l of glacial acetic acid. Incubate for 10min in fridge. Mixture turns pink. Centrifuge for 5min at 17krpm, 4°C. Collect the supernatant in a clean beaker and add the same volume of a saturated ammonium sulfate solution kept at 4°C. Incubate for 10min in the fridge. Centrifuge for 20min at 17krpm, 4°C. Discard

the supernatant. Wash the pellet with 10ml/(liter of culture) of a 1:1 mixture (v/v) of saturated ammonium sulfate and water at 4°C. Spin for 15min at 17krpm, 4°C. Resuspend the pellet in 10ml/(liter of culture) of AX buffer A. (Ev. warm up slightly.) Precipitate the protein by adding an equal volume of ethanol at room temperature. Centrifuge for 10min at 17krpm, 4°C. Repeat this step other two times. Resuspend the pellet in 10ml/(liter of culture) of buffer A.

Anion exchange with HiTrapQ XL column (V=5ml): equilibrate with 10 column volumes (CV) of buffer A, 5ml/min; load sample at 2ml/min; wash with 10 CV of buffer A, 5ml/min; elute with gradient (0 – 50% buffer B, 10 CV, 2 ml/min) and collect 2ml fractions. SDS-PAGE showed super clean protein. Reconcentrate, freeze.

For labeling: tau, add reducing agent, purify by Superdex75 equilibrated with PBS, pH 7.5 (1peak), label, remove label & change to std. measurement buffer.

C.2 PROOF OF PRINCIPLE: BLEACH STEP COUNTING WITH DNA-ORIGAMI

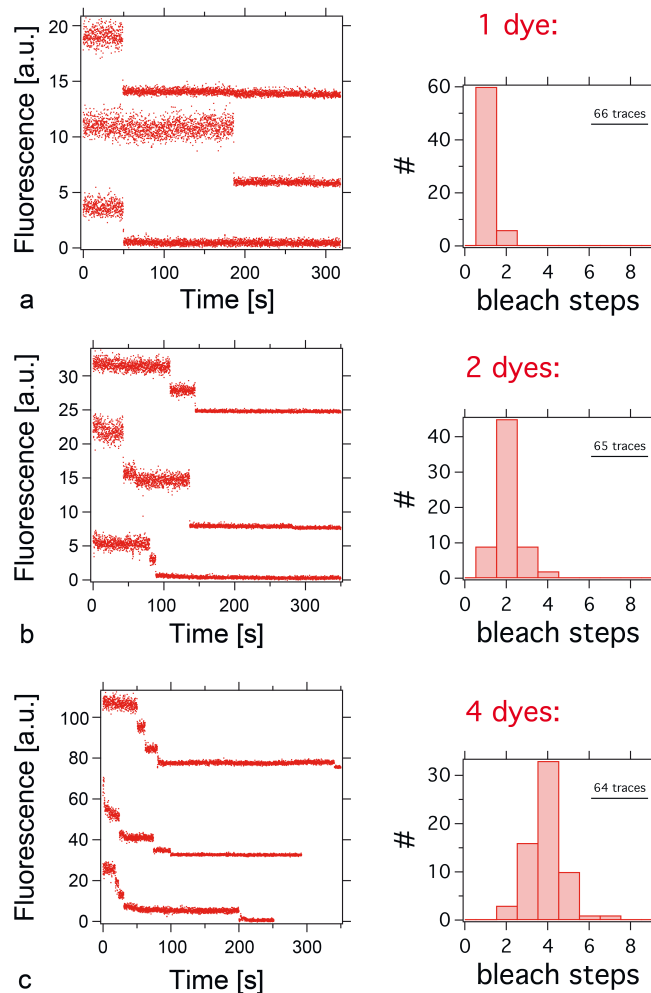


Figure C.1: Proof of principle of bleach step counting using a DNA-origami platform with (a) 1 dye, (b) 2 dyes, (c) 3 dyes. Example traces and bleach step histograms are shown. The DNA-origami construct (termed Fluorogami by Björn Hellenkamp [62]) was a kind gift of the Dietz lab at TUM.

C.3 α -SYNUCLEIN OLIGOMER SIZE

Atto647N labeled α -synuclein was incubated for more than a week in measurement buffer at $30\mu\text{M}$ and 30°C while shaking. It was diluted to sub-nanomolar concentrations and measured by TIRF on a glass surface (cleaned by successive sonication (15min) in 2% Hellmanex as well as ultrapure water followed by flushing with ultrapure water.). Measurements took place at different time points during incubation.

Even after 9 days, monomers were by far the dominating species (Figure C.2a). Neither tetrameric [11], nor other oligomers larger than dimers were significantly observed. These results were reproduced several times and confirmed also by confocal detection (in solution), atomic force microscopy (AFM) and dynamic light scattering (DLS)¹.

Only the interaction with lipid vesicles (1,2-dipalmitoyl-sn-glycero-3-phosphocholine, DPPC) led to multiple bleach events (Figure C.2b). The latter does not necessarily indicate colocalization of individual α -synuclein monomers at the same spot of the vesicle. The protein/lipid concentration ratio was 1/1000 and vesicles were immobilized on a PEG-passivated surface by biotin/neutraavidin binding (cf. Section B.3).

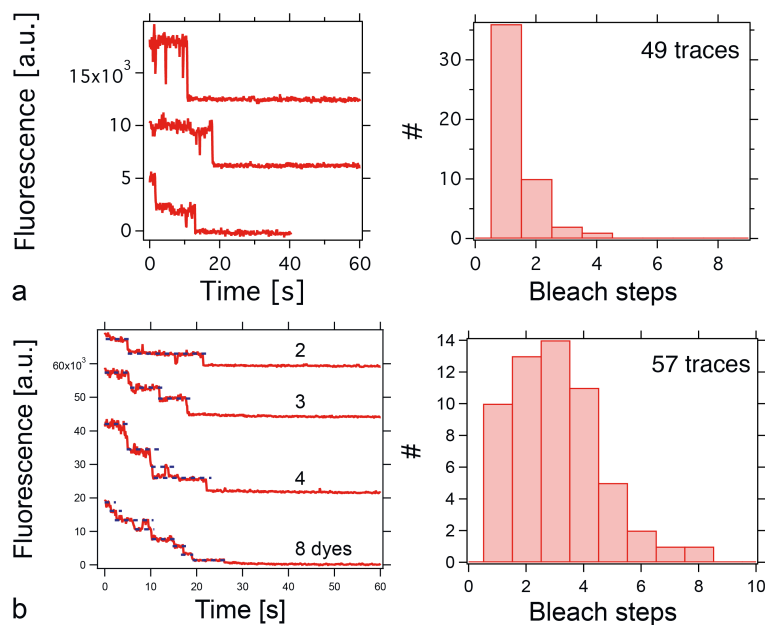


Figure C.2: α -synuclein oligomer size distributions and example traces: (a) after 9 days incubation at $30\mu\text{M}$ and 37°C with agitation, or (b) in the presence of sonicated DPPC vesicles without extra incubation.

¹ These measurements were performed by Björn Hellenkamp, Frank Stetter and Bettina Kracke, respectively.

C.4 α -SYNUCLEIN AS AN HSP90 CLIENT

α -synuclein was further investigated as a putative Hsp90 client, as there were reports of an ATP-independent interaction between the two [35, 46]. Specifically, Hsp90's conformational changes were measured by smFRET (cf. Chapter 10) in the presence and absence of $50\mu\text{M}$ α -synuclein. Despite this high concentration, hardly any effect on Hsp90's conformational kinetics was observed (Figure C.3).

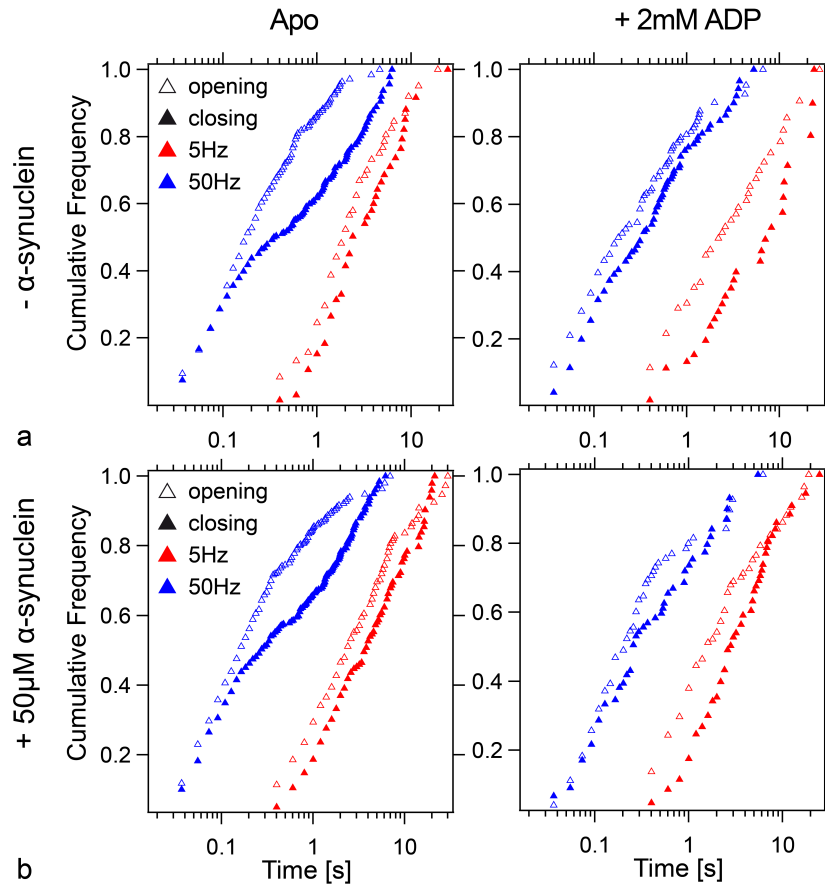


Figure C.3: The effect of $50\mu\text{M}$ α -synuclein on Hsp90's conformational dynamics: dwell time distributions in the absence (a) and presence (b) of $50\mu\text{M}$ α -synuclein, with or without 2mM ADP, as indicated. Blue and red data was recorded at the indicated sampling rate.

SMACKS Manual

Sonja Schmid & Markus Götz

Version 1.3

SMACKS (Single Molecule Analysis of Complex Kinetic Sequences) is a maximum likelihood approach to extract kinetic rate models from noisy single molecule data. While fine-tuned for FRET data, SMACKS is applicable to single molecule time traces of any kind. It optimizes hidden Markov models with a chosen number of states n based on input data of a given dimensionality d . Up to 3 dimensions were tested.

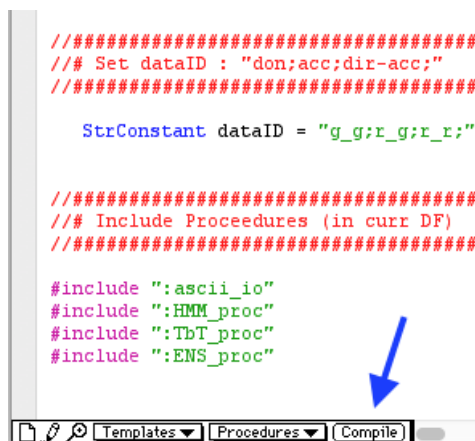
This manual explains the functionalities of the SMACKS software tool. For a complete description of the SMACKS approach please refer to Schmid et al. (2016). This manual follows the terminology of the original publication, which is itself close to Rabiner (1989) & Fink (2014).

Contents

1	Installation	2
2	Data Import	2
3	Step 1: Trace-by-Trace HMM (TbT)	3
4	Step 2: Semi-Ensemble HMM (ENS)	4
5	Export Results	6
6	Miscellaneous	6

1 Installation

SMACKS is implemented in Igor Pro (Wavemetrics). If your institution does not have a license for Igor Pro, you can still test SMACKS on your own data using the free 30 days trial of the full software package available at wavemetrics.com. After downloading SMACKS' source code and example data from singlemolecule.uni-freiburg.de/SMACKS, double click `startSMACKS.ipf` and SMACKS is ready to run. In case the SMACKS menu does not show up automatically, click the tiny compile button indicated in Fig. 1.



```
#####  
## Set dataID : "don;acc;dir-acc;"  
#####  
  
StrConstant dataID = "g_g;r_g;r_r;"  
  
#####  
## Include Procedures (in curr DF)  
#####  
  
#include ":ascii_io"  
#include ":HMM_proc"  
#include ":TbT_proc"  
#include ":ENS_proc"
```

Figure 1: The tiny compile button. It vanishes after compilation.

The `dataID` holds the names of individual dimensions of your input data (e.g. fluorescence channels). They are used by the importer as base names for the supplied input data (see next section). By default the `dataID` is set to `"g_g;r_g;r_r;"`. But you can modify it to fit your own data. For example set it to `"force;"` or `"blue;green;"` or any other semicolon separated input list. Alphabetic characters and `"_"` are allowed.

2 Data Import

For maximum compatibility, SMACKS comes with an ascii importer. For a quick test, we further include experimental example data at `SMACKS_tool/exampleData/`.

To load your data into SMACKS, go to the SMACKS menu → **Import ascii**. Press *shift* and select multiple ascii files (`.dat` or `.txt`) to import the desired dataset into SMACKS. The importer accepts files with one, two or three data columns (tab- or space-separated) representing multiple dimensions of one time trace. File names are arbitrary, as the imported trajectories are renamed as specified by the `dataID` plus suffix. (The original names are stored in Igor's "wavenotes" and recovered during results export. See respective section.)

Input data must not include NaNs or INFs. It should only contain the range that is relevant for analysis (e.g. no after-bleach tail).

All calculations are performed in user-supplied time units. E.g. if your sampling rate is 10 frames per second, all transition probabilities a_{ij} are specified per time interval of 0.1s. They are converted to rate constants in Hertz by $k_{ij} = 10 \cdot a_{ij}$ (neglecting multiple transitions per time interval). Therefore, constant time intervals are required. But specific time information is not needed.

If the optional "FRET constraint" is going to be used, fluorescence data must be corrected for experimental offsets, crosstalk, gamma, as detailed in Lee et al. (2005).

3 Step 1: Trace-by-Trace HMM (TbT)

As a first step, individual HMMs are optimized for each trajectory separately. The TbT workflow can be called from the SMACKS menu → **Init TbT**. The resulting user interface is shown in Figure 2.

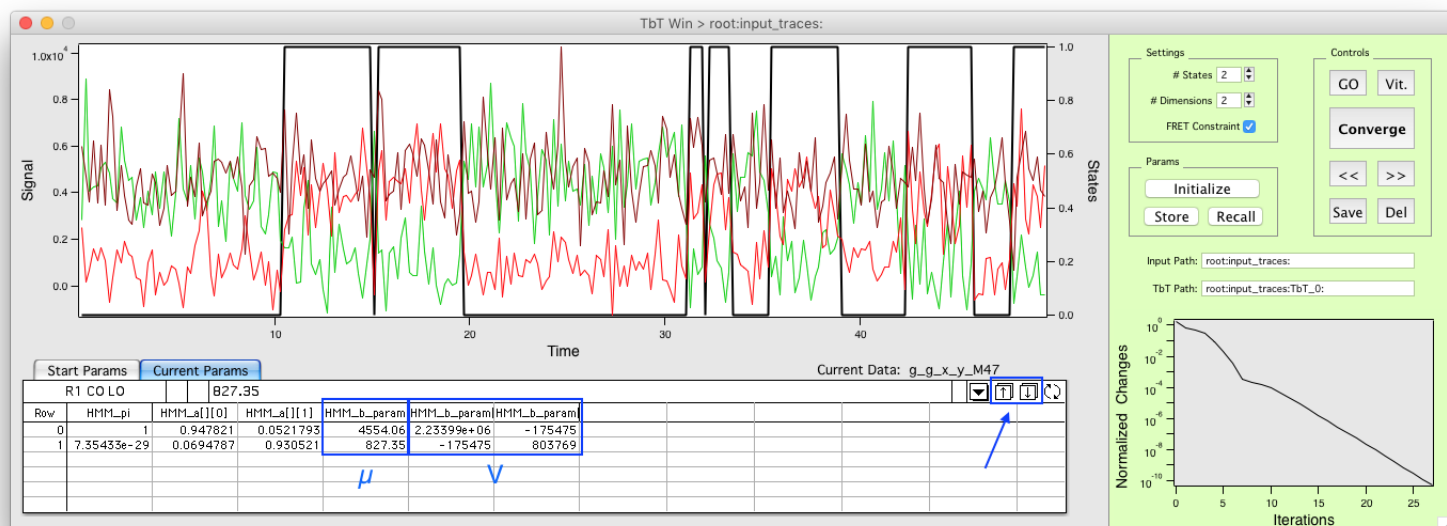


Figure 2: The Trace-by-Trace HMM interface, TbT Win.

The data plot (top left of Fig. 2) shows all dimensions of the current input trace (e.g. FRET donor in green, acceptor in red, directly excited acceptor in dark red). Once determined, the states assigned by the Viterbi algorithm (subsequently referred to as *Viterbi path*) are displayed in black. Time is displayed in the user-supplied units (i.e. time bins of the measurement). The name of the current input trace is shown below the plot on the right.

The parameter tabs (bottom left of Fig. 2) display the **Initial Params** or the **Current Params**. HMM_pi, HMM_a and HMM_b_param denote the π , A and B parameters, respectively. The π vector comprises one start probability per state. The matrix A holds all transition probabilities, i.e. $n \times n$ entries. The rows specify the initial state and the columns the final state. To preclude a certain transition, set the respective matrix element to 0. The Gaussian probability densities (one per state) are parametrized by B , which holds the Gauss positions μ (in d dimensions) in the first column and the co-variance matrix V in the adjacent $d \times d$ dimensions as indicated for two states in Fig. 2. The μ and V of individual states are stored in n individual layers. These are accessible in Igor by the up/down arrows indicated in Fig. 2 (active after clicking the corresponding column).

SMACKS provides typical initial parameters for TIRF experiments. Customized initial B parameters can be obtained from Gaussian fits to your data histogram. For multi-dimensional data, a diagonal co-variance matrix V is usually a good starting point and possible correlations are fit during optimization.

Click the **Initial Params** tab to adjust the default parameters for your needs. Don't forget to confirm modifications by clicking **Initialize**. Existing **Current Params** are overwritten. You can store and recall current parameters with the respective buttons, **Store** or **Recall**.

The control panel at the right lets you proceed through the TbT workflow: Start by telling SMACKS the number of states (**# States**) that you discern in your data by eye, subsequently referred to as *apparent states*. It is no problem if not every trace reaches all of these states (see below). Next set the number of dimensions (**# Dimensions**). For 2D input, there is the **FRET Constraint** option detailed in Schmid et al. (2016).

Now you are ready to run: click **Converge** to optimize an HMM based on the current input. The convergence can be followed by the **Normalized Changes** plot below (see the Miscellaneous section for details). You can always interrupt SMACKS by clicking the red **Stop** button that appears when SMACKS is busy. Alternatively, use **Go** for one iteration at a time and **Vit.** to calculate the most probable state sequence given the current input (data & parameters).

If you are happy with the optimized parameters (i.e. they have converged and yield reasonable state allocation), save them by clicking **Save** or delete them again by **Del.** If the initial parameters are not appropriate for the input data, the Forward Backward algorithm will diverge. SMACKS will let you know by printing a "numerical error" message.

Once appropriate *initial* parameters were found, you can speed up the TbT procedure by calling **TbT Batch Converge** from the SMACKS menu. This will optimize individual parameters for each trace in the dataset. Only the parameters that converged properly will be saved. Next browse through the traces (using <<, >>) and delete parameters that cause inappropriate Viterbi paths. For traces that do not reach all states, no reasonable parameters can be found. Therefore, those parameters should be deleted even if the optimization converged.

To get around this issue, call **TbT Apply Means** once the inappropriate parameters have been deleted. Thereby, the mean of all saved **B** parameters is applied to the remaining trajectories (i.e. those without saved parameters). For simplicity only these "remaining" trajectories will be displayed in the TbT Win. If at this stage, there are many "good quality" traces that are not well fit, you should reconsider your initial definition of the apparent states. Otherwise, sort out unrepresentative traces by deleting their parameters again. These are not considered in the next step: the ENS run.

The current **Input Path** and **TbT Path** are both displayed below the controls. The former denotes Igor's data folder holding the original input data, which is not modified by SMACKS. The latter holds all TbT related data, i.e. parameters, Viterbi paths, auxiliaries.

4 Step 2: Semi-Ensemble HMM (ENS)

The ENS workflow is called from the SMACKS menu → **Init ENS**, which displays the **ENS Win** shown in Figure 3 and closes the **TbT Win**. (Both windows can be recreated by the respective entry of the SMACKS menu.)

Based on the apparent states and the optimized **B** parameters of the TbT workflow, the ENS interface lets you analyze different state models assembled in the setup tabs (**Setup0** etc.).

So tell SMACKS the desired state model configuration, short **State Config**. E.g. "0011" is interpreted as a 4-state model including twice the apparent state0 and twice the apparent state1. Analogously, "0120" denotes twice the apparent state 0 and once the apparent states 1 and 2. If required, adjust the default **Initial Params**. Either way, confirm by clicking **Initialize**.

Further settings are the maximal number of iterations (**Max. Iterations**) per run and the maximal "Normalized Changes" threshold serving as convergence criterion, **Conv. Threshold**. Generally applicable default values are provided. An optional detailed balance constraint, adapted from Greenfeld et al. (2012), conserves the model at thermodynamic equilibrium. This

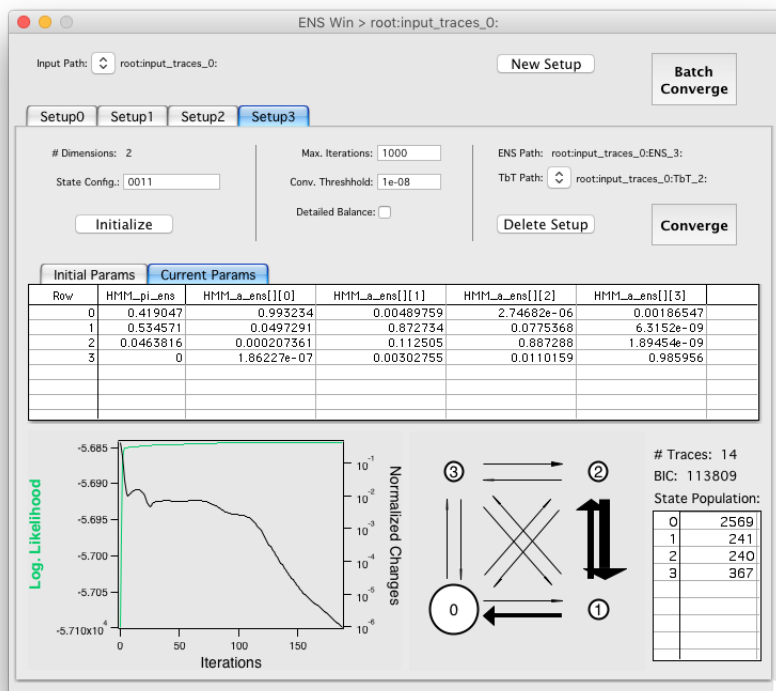


Figure 3: The ensemble HMM interface, ENS Win.

constraint is adequate for experiments without an external energy source (e.g. ATP).

After submitting the desired **Initial Params** by clicking **Initialize** (see Step 1 for parameter details), **Converge** will optimize the model until either the **Conv. Threshold** or **Max. Iterations** are reached. As in TbT mode, a red **Stop** button shows up, which lets you stop the calculations at any time.

The **Log Likelihood** plot provides visual feedback on the state of convergence. A cartoon illustrates the current rate model (center bottom). Additionally, the number of considered traces (**# Traces**), the current value of the Bayesian information criterion (**BIC**) and the relative **State Population** deduced from the Viterbi paths are displayed on the right.

Among several model configurations, the most appropriate model can be identified using parsimony criteria, such as **BIC**. Click **New Setup** to create an additional setup or **Delete Setup** to delete a specific setup. The latter does not affect original input and TbT data. **Batch Converge** (top right) runs over all predefined setups. This is useful to perform calculations overnight. You can stop and resume calculations at will.

The data of each setup is stored in a specific **ENS Path**. Ensemble HMM makes use of the TbT information stored in the displayed **TbT Path**.

5 Export Results

To export the results, call the SMACKS menu → **Export Results**. The ensemble optimized start and transitions probabilities together with additional results will be stored in SMACKS_summary.dat. The individual B parameters and Viterbi paths are reported as separate files specified by the original filenames: "original name"_b_param.dat or "original name"_viterbi.dat , respectively.

6 Miscellaneous

- **Normalized Changes** of the diagonal entries of the transition matrix have proven useful for monitoring convergence of the HMM:

$$\text{Normalized Changes} = \sum_{i=0}^{n-1} \frac{|a_{ii} - a'_{ii}|}{a_{ii}}$$

where a'_{ii} are the diagonal matrix elements of the previous iteration and the sum goes over all states. While the likelihood increases monotonically, the **Normalized Changes** may not.

- The **Viterbi Browser** called from the SMACKS menu lets you review all saved trajectories. Both the **TbT Win** and the **ENS Win** are recreated by the respective entry of the SMACKS menu.
- SMACKS' data hierarchy inside Igor:
Input data is stored at `root:input_traces_0: .`
The TbT step is performed in `root:input_traces_0:TbT_0: .`
The ENS step is performed in `root:input_traces_0:ENS_0: .`
Higher suffix numbers (`_1, _2, ...`) are used for additional folders of the same kind, such as additional ENS setups.
Call the SMACKS menu → **Set Input Path** to change between different input paths. The complete data folder hierarchy is displayed by Igor's Data Browser (Data menu → Data Browser).

References

- S. Schmid, M. Götz, and T. Hugel. Single-molecule analysis beyond dwell times: Demonstration and assessment in and out of equilibrium. *Biophysical Journal*, 111(7):1375 – 1384, OCT 4 2016.
- Lawrence R. Rabiner. A tutorial on hidden markov models and selected applications in speech recognition. *Proceedings of the IEEE*, 77(2):257–286, Feb 1989.
- Gernot A Fink. Markov models for pattern recognition: from theory to applications. *Springer Science & Business Media*, , 2014.
- Nam Ki Lee, Achillefs N. Kapanidis, You Wang, Xavier Michalet, Jayanta Mukhopadhyay, Richard H. Ebright, and Shimon Weiss. Accurate fret measurements within single diffusing biomolecules using alternating-laser excitation. *Biophysical journal*, 88(4):2939–2953, 2005.
- Max Greenfeld, Dmitri S. Pavlichin, Hideo Mabuchi, and Daniel Herschlag. Single molecule analysis research tool (SMART): An integrated approach for analyzing single molecule data. *PLoS ONE*, 7(2):e30024, 2012.

BIBLIOGRAPHY

- [1] Aitken CE, Marshall RA, & Puglisi JD. An Oxygen Scavenging System for Improvement of Dye Stability in Single-Molecule Fluorescence Experiments. *Biophysical Journal* 94, 5 (2008), 1826–1835. [Link](#). (Cit. on p. 42).
- [2] Ali M, Roe S, et al. Crystal structure of an Hsp90-nucleotide-p23/Sba1 closed chaperone complex. English. *Nature* 440, 7087 (2006), 1013–1017 (cit. on pp. 5, 36, 81, 99).
- [3] Allan RK, Mok D, Ward BK, & Ratajczak T. Modulation of Chaperone Function and Co-chaperone Interaction by Novobiocin in the C-terminal Domain of Hsp90. *Journal of Biological Chemistry* 281, 11 (2006), 7161–7171. [Link](#). (Cit. on p. 89).
- [4] Amann CP, Schmiedl T, & Seifert U. Communications: Can one identify nonequilibrium in a three-state system by analyzing two-state trajectories? *The Journal of Chemical Physics* 132, 4, 041102 (2010), 041102. [Link](#). (Cit. on p. 126).
- [5] Andrec M, Levy RM, & Talaga DS. Direct Determination of Kinetic Rates from Single-Molecule Photon Arrival Trajectories Using Hidden Markov Models. *The Journal of Physical Chemistry A* 107, 38 (2003). PMID: 19626138, 7454–7464. [Link](#). (Cit. on p. 21).
- [6] Ansari A, Berendzen J, et al. Protein states and proteinquakes. *Proceedings of the National Academy of Sciences* 82, 15 (1985), 5000–5004. [Link](#). (Cit. on p. 54).
- [7] Anyika M, McMullen M, Forsberg LK, Dobrowsky RT, & Blagg BSJ. Development of Noviomimetics as C-Terminal Hsp90 Inhibitors. *ACS Medicinal Chemistry Letters* 7, 1 (2016), 67–71. [Link](#). (Cit. on pp. 7, 87).
- [8] Bahl L, & Jelinek F. Decoding for channels with insertions, deletions, and substitutions with applications to speech recognition. *IEEE Transactions on Information Theory* 21, 4 (1975), 404–411 (cit. on p. 21).
- [9] Baker J. The DRAGON system—An overview. *IEEE Transactions on Acoustics, Speech, and Signal Processing* 23, 1 (1975), 24–29 (cit. on p. 21).
- [10] Banterle N, & Lemke EA. Nanoscale devices for linkerless long-term single-molecule observation. *Current Opinion in Biotechnology* 39 (2016), 105–112. [Link](#). (Cit. on p. 15).
- [11] Bartels T, Choi JG, & Selkoe DJ. α -Synuclein occurs physiologically as a helically folded tetramer that resists aggregation. *Nature* 477, 7362 (2011), 107–110. [Link](#). (Cit. on p. 129).
- [12] Baum LE, & Sell GR. Growth transformations for functions on manifolds. *Pacific J. Math.* 27, 2 (1968), 211–227. [Link](#). (Cit. on p. 22).
- [13] Beckett D, Kovaleva E, & Schatz PJ. A minimal peptide substrate in biotin holoenzyme synthetase-catalyzed biotinylation. *Protein Science* 8, 4 (1999), 921–929. [Link](#). (Cit. on p. 37).
- [14] Blagg BSJ, & Kerr TD. Hsp90 inhibitors: Small molecules that transform the Hsp90 protein folding machinery into a catalyst for protein degradation. *Medicinal Research Reviews* 26, 3 (2006), 310–338. [Link](#). (Cit. on p. 7).
- [15] Blanco MR, Martin JS, et al. Single Molecule Cluster Analysis dissects splicing pathway conformational dynamics. *Nat Meth* 12, 11 (2015), 1077–1084. [Link](#). (Cit. on p. 64).
- [16] Blatch G, & Edkins A. *The Networking of Chaperones by Co-chaperones: Control of Cellular Protein Homeostasis*. Subcellular Biochemistry. Springer International Publishing, 2014 (cit. on p. 6).
- [17] Borkovich KA, Farrelly FW, Finkelstein DB, Taulien J, & Lindquist S. hsp82 is an essential protein that is required in higher concentrations for growth of cells at higher temperatures. *Molecular and Cellular Biology* 9, 9 (1989), 3919–3930. [Link](#). (Cit. on p. 5).
- [18] Bouilly D, Hon J, et al. Single-Molecule Reaction Chemistry in Patterned Nanowells. *Nano Letters* 16, 7 (2016). PMID: 27270004, 4679–4685. [Link](#). (Cit. on p. 106).
- [19] Bruno WJ, Yang J, & Pearson JE. Using independent open-to-closed transitions to simplify aggregated Markov models of ion channel gating kinetics. *Proceedings of the National Academy of Sciences of the United States of America* 102, 18 (2005), 6326–6331. [Link](#). (Cit. on pp. 76, 125, 126).
- [20] Calderon CP, Harris NC, Kiang CH, & Cox DD. Quantifying Multiscale Noise Sources in Single-Molecule Time Series. *The Journal of Physical Chemistry B* 113, 1 (2009). PMID: 19072043, 138–148. [Link](#). (Cit. on p. 21).
- [21] Chaiet L, & Wolf F. The Properties of Streptavidin, a Biotin-Binding Protein Produced by Streptomycetes. *Arch. Biochem. Biophys.* 106 (1964), 1–5 (cit. on p. 36).
- [22] Chandradoss SD, Haagsma AC, et al. Surface Passivation for Single-molecule Protein Studies. 86 (2014), e50549. [Link](#). (Cit. on p. 15).

- [23] Chen C, Loe F, Blocki A, Peng Y, & Raghunath M. Applying macromolecular crowding to enhance extracellular matrix deposition and its remodeling in vitro for tissue engineering and cell-based therapies. *Advanced Drug Delivery Reviews* 63, 4–5 (2011), 277–290. [Link](#). (Cit. on p. 96).
- [24] Chen Y, Shen K, Shan SO, & Kou SC. Analyzing Single-Molecule Protein Transportation Experiments via Hierarchical Hidden Markov Models. *Journal of the American Statistical Association* ja (2016), 1–49. [Link](#). (Cit. on p. 64).
- [25] Chiosis G, Huezio H, et al. 17AAG: Low Target Binding Affinity and Potent Cell Activity—Finding an Explanation. *Molecular Cancer Therapeutics* 2, 2 (2003), 123–129. [Link](#). (Cit. on p. 100).
- [26] Chiosis G, Timaul MN, et al. A small molecule designed to bind to the adenine nucleotide pocket of Hsp90 causes Her2 degradation and the growth arrest and differentiation of breast cancer cells. *Chemistry & Biology* 8, 3 (2001), 289–299. [Link](#). (Cit. on p. 7).
- [27] Choi Y, Moody IS, et al. Single-Molecule Lysozyme Dynamics Monitored by an Electronic Circuit. *Science* 335, 6066 (2012), 319–324. [Link](#). (Cit. on p. 106).
- [28] Choi Y, Olsen TJ, et al. Dissecting Single-Molecule Signal Transduction in Carbon Nanotube Circuits with Protein Engineering. *Nano Letters* 13, 2 (2013). PMID: 23323846, 625–631. [Link](#). (Cit. on p. 106).
- [29] Chung SH, Moore JB, Xia L, Premkumar LS, & Gage PW. Characterization of Single Channel Currents Using Digital Signal Processing Techniques Based on Hidden Markov Models. *Philosophical Transactions of the Royal Society of London B: Biological Sciences* 329, 1254 (1990), 265–285. [Link](#). (Cit. on p. 21).
- [30] Clegg R. Laboratory Techniques in Biochemistry and Molecular Biology. Ed. by Gadella T. Vol. 33. Academic Press, 2009. Chap. Förster resonance energy transfer—FRET what is it, why do it, and how it's done. 1–57 (cit. on p. 12).
- [31] Cohen AE, & Moerner WE. Suppressing Brownian motion of individual biomolecules in solution. *Proceedings of the National Academy of Sciences of the United States of America* 103, 12 (2006), 4362–4365. [Link](#). (Cit. on p. 15).
- [32] Colombo G, Morra G, Meli M, & Verkhrivker G. Understanding ligand-based modulation of the Hsp90 molecular chaperone dynamics at atomic resolution. *Proceedings of the National Academy of Sciences* 105, 23 (2008), 7976–7981. [Link](#). (Cit. on p. 81).
- [33] Cordes T, Maiser A, Steinhauer C, Schermelleh L, & Tinnefeld P. Mechanisms and advancement of antifading agents for fluorescence microscopy and single-molecule spectroscopy. *Phys. Chem. Chem. Phys.* 13 (14 2011), 6699–6709. [Link](#). (Cit. on p. 42).
- [34] Cunningham CN, Southworth DR, Krukenberg KA, & Agard DA. The conserved arginine 380 of Hsp90 is not a catalytic residue, but stabilizes the closed conformation required for ATP hydrolysis. *Protein Science* 21, 8 (2012), 1162–1171. [Link](#). (Cit. on p. 6).
- [35] Daturpalli S, Waudby CA, Meehan S, & Jackson SE. Hsp90 Inhibits α -Synuclein Aggregation by Interacting with Soluble Oligomers. *Journal of Molecular Biology* 425, 22 (2013), 4614–4628. [Link](#). (Cit. on p. 130).
- [36] Debnath P, Min W, Xie XS, & Cherayil BJ. Multiple time scale dynamics of distance fluctuations in a semiflexible polymer: A one-dimensional generalized Langevin equation treatment. *The Journal of Chemical Physics* 123, 20 (2005), [Link](#). (Cit. on pp. 65, 106).
- [37] DeBoer C, Meulman P, Wnuk R, & Peterson D. Geldanamycin, a new antibiotic. *The Journal of antibiotics* 23, 9 (1970), 442–447 (cit. on p. 7).
- [38] Delmotte P, & Delmotte-Plaquee J. A New Antifungal Substance of Fungal Origin. *Nature* 171, 4347 (1953), 344–344. [Link](#). (Cit. on p. 7).
- [39] Demtröder W. *Experimentalphysik 3: Atome, Moleküle und Festkörper*. Springer, 2005 (cit. on pp. 9, 11, 17, 18).
- [40] Demtröder W. *Experimentalphysik 2: Elektrizität und Optik*. 6th ed. Springer, 2014 (cit. on p. 16).
- [41] Diez M, Zimmermann B, et al. Proton-powered subunit rotation in single membrane-bound F0F1-ATP synthase. *Nat Struct Mol Biol* 11, 2 (2004), 135–141. [Link](#). (Cit. on p. 3).
- [42] Dijk M van, & Bonvin AMJJ. 3D-DART: a DNA structure modelling server. *Nucl. Acids Res.* 37, W235–W239 (2009) (cit. on pp. 44, 45, 51).
- [43] Dill K, & Bromberg S. *Molecular driving forces: statistical thermodynamics in biology, chemistry, physics, and nanoscience*. Garland Science, 2010 (cit. on p. 102).
- [44] Ellis RJ. Macromolecular crowding: obvious but underappreciated. *Trends in Biochemical Sciences* 26, 10 (2001), 597–604. [Link](#). (Cit. on p. 96).
- [45] Ellis RJ, & Minton AP. Cell biology: Join the crowd. *Nature* 425, 6953 (2003), 27–28. [Link](#). (Cit. on p. 95).
- [46] Falsone SF, Kungl AJ, Rek A, Cappai R, & Zangger K. The Molecular Chaperone Hsp90 Modulates Intermediate Steps of Amyloid Assembly of the Parkinson-related Protein α -Synuclein. *Journal of Biological Chemistry* 284, 45 (2009), 31190–31199. [Link](#). (Cit. on p. 130).
- [47] Fink G. Mustererkennung mit Markov-Modellen: Theorie - Praxis - Anwendungsgebiete. *Vieweg + Teubner Stuttgart*. Leitfäden der Informatik (2013). [Link](#). (Cit. on p. 22).

- [48] Flomenbom O, Klafter J, & Szabo A. What Can One Learn from Two-State Single-Molecule Trajectories? *Biophysical Journal* 88, 6 (2005), 3780–3783. [Link](#). (Cit. on p. 126).
- [49] Förster T. Zwischenmolekulare Energiewanderung und Fluoreszenz. *Annalen der Physik* 437, 1-2 (1948), 55–75. [Link](#). (Cit. on p. 12).
- [50] Frauenfelder H, Sligar S, & Wolynes P. The energy landscapes and motions of proteins. *Science* 254, 5038 (1991), 1598–1603. [Link](#). (Cit. on p. 65).
- [51] Gabriel O. *Franck-Condon-Prinzip*. 2007. url: <https://commons.wikimedia.org/wiki/File:Franck-Condon-Prinzip.svg> (Last accessed: 11/14/2016) (cit. on p. 11).
- [52] Garg G, Khandelwal A, & Blagg BS. Chapter Three - Anticancer Inhibitors of Hsp90 Function: Beyond the Usual Suspects. *Hsp90 in Cancer: Beyond the Usual Suspects*. Ed. by Isaacs J, & Whitesell L. Vol. 129. Advances in Cancer Research. Academic Press, 2016, 51–88. [Link](#). (Cit. on p. 7).
- [53] Garnier C, Lafitte D, et al. Binding of ATP to Heat Shock Protein 90: EVIDENCE FOR AN ATP-BINDING SITE IN THE C-TERMINAL DOMAIN. *Journal of Biological Chemistry* 277, 14 (2002), 12208–12214. [Link](#). (Cit. on p. 80).
- [54] Gebhardt JCM, Clemen AEM, Jaud J, & Rief M. Myosin-V is a mechanical ratchet. *Proceedings of the National Academy of Sciences* 103, 23 (2006), 8680–8685. [Link](#). (Cit. on p. 3).
- [55] Giudici P, Rydén T, & Vandekerckhove P. Likelihood-Ratio Tests for Hidden Markov Models. English. *Biometrics* 56, 3 (2000), 742–747. [Link](#). (Cit. on p. 68).
- [56] Glynn SE, Nager AR, Baker TA, & Sauer RT. Dynamic and static components power unfolding in topologically closed rings of a AAA+ proteolytic machine. *Nat Struct Mol Biol* 19, 6 (2012), 616–622. [Link](#). (Cit. on p. 3).
- [57] Greenfield M, Pavlichin DS, Mabuchi H, & Herschlag D. Single Molecule Analysis Research Tool (SMART): An Integrated Approach for Analyzing Single Molecule Data. *PLoS ONE* 7, 2 (2012), e30024. [Link](#). (Cit. on pp. 64, 65, 68, 112).
- [58] Halpin JC, Huang B, Sun M, & Street TO. Crowding Activates Heat Shock Protein 90. *Journal of Biological Chemistry* (2016). [Link](#). (Cit. on p. 100).
- [59] He H, Zatorska D, et al. Identification of potent water soluble purine-scaffold inhibitors of the heat shock protein 90. *Journal of medicinal chemistry* 49, 1 (2006), 381–390 (cit. on p. 87).
- [60] Hearnshaw SJ, Chung TTH, Stevenson CEM, Maxwell A, & Lawson DM. The role of monovalent cations in the ATPase reaction of DNA gyrase. *Acta Crystallographica Section D* 71, 4 (2015), 996–1005. [Link](#). (Cit. on p. 103).
- [61] Hellenkamp B, Wortmann P, Kandzia F, Zacharias M, & Hugel T. Multi-domain structure and correlated dynamics determined by self-consistent FRET networks. *in press* (2016) (cit. on pp. 5, 50, 80, 99).
- [62] Hellenkamp B. DYNAMIC STRUCTURE OF A MULTI-DOMAIN PROTEIN. PhD thesis. TUM, 2016 (cit. on pp. 44–46, 50, 128).
- [63] Henzler-Wildman K, & Kern D. Dynamic personalities of proteins. *Nature* 450, 7172 (2007), 964–972. [Link](#). (Cit. on p. 65).
- [64] Hessling M, Richter K, & Buchner J. Dissection of the ATP-induced conformational cycle of the molecular chaperone Hsp90. English. *Nat. Struct. Mol. Biol.* 16, 3 (2009), 287–293 (cit. on pp. 86, 121).
- [65] Hill T. Free energy transduction and biochemical cycle kinetics. *Springer* 1st edition (1989). [Link](#). (Cit. on p. 70).
- [66] Holliday R. A mechanism for gene conversion in fungi. *Genetics Research* 89 (Special Issue 5-6 2007), 285–307. [Link](#). (Cit. on p. 52).
- [67] Horn R, & Lange K. Estimating kinetic constants from single channel data. *Biophysical Journal* 43, 2 (1983), 207–223. [Link](#). (Cit. on p. 55).
- [68] Howard J. Mechanics of Motor Proteins and the Cytoskeleton. *Sinauer Associates* 1st edition (2001). [Link](#). (Cit. on p. 70).
- [69] Hu X, Machius M, & Yang W. Monovalent cation dependence and preference of GHKL ATPases and kinases. *FEBS Letters* 544, 1–3 (2003), 268–273. [Link](#). (Cit. on p. 103).
- [70] Hughes L, Rawle R, & Boxer S. Choose Your Label Wisely: Water-Soluble Fluorophores Often Interact with Lipid Bilayers. *PLoS ONE* 9, 2 (2014), e87649 (cit. on p. 36).
- [71] Hutchison KA, Czar MJ, Scherrer LC, & Pratt WB. Monovalent cation selectivity for ATP-dependent association of the glucocorticoid receptor with hsp70 and hsp90. *Journal of Biological Chemistry* 267, 20 (1992), 14047–14053. [Link](#). (Cit. on p. 103).
- [72] Immormino RM, Kang Y, Chiosis G, & Gewirth DT. Structural and Quantum Chemical Studies of 8-Arylsulfanyl Adenine Class Hsp90 Inhibitors. *Journal of Medicinal Chemistry* 49, 16 (2006). PMID: 16884307, 4953–4960. [Link](#). (Cit. on pp. 7, 87).
- [73] Inaglory B. *Green sea turtle, Chelonia mydas and his total internal reflection*. 2008. url: https://commons.wikimedia.org/wiki/File:Total_internal_reflection_of_Chelonia_mydas.jpg (Last accessed: 11/14/2016) (cit. on p. 16).

- [74] Jahn M, Rehn A, et al. The charged linker of the molecular chaperone Hsp90 modulates domain contacts and biological function. *Proc. Natl. Acad. Sci. USA* 111, 50 (2014), 17881–17886. [Link](#). (Cit. on pp. 6, 121).
- [75] Jakob U, Scheibel T, Bose S, Reinstein J, & Buchner J. Assessment of the ATP Binding Properties of Hsp90. *Journal of Biological Chemistry* 271, 17 (1996), 10035–10041. [Link](#). (Cit. on p. 80).
- [76] Kalinin S, Peulen T, et al. A toolkit and benchmark study for FRET-restrained high-precision structural modeling. *Nat Meth* 9, 12 (2012), 1218–1225. [Link](#). (Cit. on pp. 44, 45, 51).
- [77] Karagöz GE, Duarte AM, et al. Hsp90-Tau complex reveals molecular basis for specificity in chaperone action. *Cell* 156, 5 (2014), 963–974 (cit. on p. 100).
- [78] Keller BG, Kobitski A, Jäschke A, Nienhaus GU, & Noé F. Complex RNA Folding Kinetics Revealed by Single-Molecule FRET and Hidden Markov Models. *Journal of the American Chemical Society* 136, 12 (2014). PMID: 24568646, 4534–4543. [Link](#). (Cit. on p. 64).
- [79] Kelly D, Dillingham M, Hudson A, & Wiesner K. A New Method for Inferring Hidden Markov Models from Noisy Time Sequences. *PLoS ONE* 7, 1 (2012), e29703. [Link](#). (Cit. on p. 65).
- [80] Kemmerich FE, Swoboda M, et al. Simultaneous Single-Molecule Force and Fluorescence Sampling of DNA Nanostructure Conformations Using Magnetic Tweezers. *Nano Letters* 16, 1 (2016). PMID: 26632021, 381–386. [Link](#). (Cit. on p. 15).
- [81] Kendall JM, & Badminton MN. *Aequorea victoria* bioluminescence moves into an exciting new era. *Trends in Biotechnology* 16, 5 (1998), 216–224. [Link](#). (Cit. on p. 12).
- [82] Khandelwal A, Crowley VM, & Blagg BSJ. Natural Product Inspired N-Terminal Hsp90 Inhibitors: From Bench to Bedside? *Medicinal Research Reviews* 36, 1 (2016), 92–118. [Link](#). (Cit. on pp. 3, 6, 7).
- [83] Kruithof M, & Noort J van. Hidden Markov Analysis of Nucleosome Unwrapping Under Force. *Biophysical Journal* 96, 9 (2009), 3708–3715. [Link](#). (Cit. on p. 21).
- [84] Kuznetsova IM, Turoverov KK, & Uversky VN. What Macromolecular Crowding Can Do to a Protein. *International Journal of Molecular Sciences* 15, 12 (2014), 23090. [Link](#). (Cit. on p. 96).
- [85] Kuznetsova IM, Zaslavsky BY, Breydo L, Turoverov KK, & Uversky VN. Beyond the Excluded Volume Effects: Mechanistic Complexity of the Crowded Milieu. *Molecules* 20, 1 (2015), 1377. [Link](#). (Cit. on p. 95).
- [86] Lakowicz J. *Principles of Fluorescence Spectroscopy*. Springer US, 2007 (cit. on pp. 10, 13, 19).
- [87] Lane DP. p53, guardian of the genome. *Nature* 358, 6381 (1992), 15–16. [Link](#). (Cit. on p. 6).
- [88] Lang MJ, Fordyce PM, Engh AM, Neuman KC, & Block SM. Simultaneous, coincident optical trapping and single-molecule fluorescence. *Nat Meth* 1, 2 (2004), 133–139. [Link](#). (Cit. on p. 15).
- [89] Lee NK, Kapanidis AN, et al. Accurate FRET Measurements within Single Diffusing Biomolecules Using Alternating-Laser Excitation. *Biophysical journal* 88, 4 (2005), 2939–2953. [Link](#). (Cit. on p. 32).
- [90] Li J, Richter K, & Buchner J. Mixed Hsp90–cochaperone complexes are important for the progression of the reaction cycle. *Nat Struct Mol Biol* 18, 1 (2011), 61–66. [Link](#). (Cit. on p. 6).
- [91] Li J, Richter K, Reinstein J, & Buchner J. Integration of the accelerator Aha1 in the Hsp90 co-chaperone cycle. *Nat Struct Mol Biol* 20, 3 (2013), 326–331. [Link](#). (Cit. on pp. 6, 85, 86).
- [92] Liu Y, Park J, Dahmen KA, Chemla YR, & Ha T. A Comparative Study of Multivariate and Univariate Hidden Markov Modelings in Time-Binned Single-Molecule FRET Data Analysis. *J. Phys. Chem. B* 114, 16 (2010). PMID: 20361785, 5386–5403. [Link](#). (Cit. on pp. 61, 65).
- [93] Lu X, & Olson WK. 3DNA: a software package for the analysis, rebuilding and visualization of three-dimensional nucleic acid structures. *Nucleic Acids Research* 31, 17 (2003), 5108–5121. [Link](#). (Cit. on p. 51).
- [94] Lu Y, Ansar S, Michaelis ML, & Blagg BS. Neuroprotective activity and evaluation of Hsp90 inhibitors in an immortalized neuronal cell line. *Bioorganic & Medicinal Chemistry* 17, 4 (2009), 1709–1715. [Link](#). (Cit. on p. 87).
- [95] Marcu MG, Chadli A, Bouhouche I, Catelli M, & Neckers LM. The Heat Shock Protein 90 Antagonist Novobiocin Interacts with a Previously Unrecognized ATP-binding Domain in the Carboxyl Terminus of the Chaperone. *Journal of Biological Chemistry* 275, 47 (2000), 37181–37186. [Link](#). (Cit. on p. 7).
- [96] Marcu MG, Schulte TW, & Neckers L. Novobiocin and Related Coumarins and Depletion of Heat Shock Protein 90-Dependent Signaling Proteins. *Journal of the National Cancer Institute* 92, 3 (2000), 242–248. [Link](#). (Cit. on p. 89).
- [97] Martinez-Ruiz A, Villanueva L, et al. S-nitrosylation of Hsp90 promotes the inhibition of its ATPase and endothelial nitric oxide synthase regulatory activities. *Proceedings of the National Academy of Sciences of the United States of America* 102, 24 (2005), 8525–8530. [Link](#). (Cit. on pp. 6, 90).
- [98] Mathlouthi M, & Reiser P. *Sucrose: Properties and Applications*. Springer US, 1995 (cit. on p. 96).

- [99] Matts RL, Dixit A, et al. Elucidation of the Hsp90 C-Terminal Inhibitor Binding Site. *ACS Chemical Biology* (2011). [Link](#). (Cit. on pp. 7, 89).
- [100] Mayer MP, & Breton LL. Hsp90: Breaking the Symmetry. *Molecular Cell* 58, 1 (2015), 8–20. [Link](#). (Cit. on p. 90).
- [101] McKinney SA, Declais AC, Lilley DMJ, & Ha T. Structural dynamics of individual Holliday junctions. *Nat Struct Mol Biol* 10, 2 (2003), 93–97. [Link](#). (Cit. on pp. 52, 123).
- [102] McKinney SA, Joo C, & Ha T. Analysis of Single-Molecule FRET Trajectories Using Hidden Markov Modeling. *Biophysical Journal* 91, 5 (2006), 1941–1951. [Link](#). (Cit. on pp. 21, 65).
- [103] Medalia O, Weber I, et al. Macromolecular Architecture in Eukaryotic Cells Visualized by Cryo-electron Tomography. *Science* 298, 5596 (2002), 1209–1213. [Link](#). (Cit. on p. 95).
- [104] Medeiros Gd, Norlin N, et al. Confocal multiview light-sheet microscopy. *Nature Communications* 6 (2015), [Link](#). (Cit. on p. 15).
- [105] Meent JW van de, Bronson JE, Wiggins CH, & Gonzalez Jr. RL. Empirical Bayes Methods Enable Advanced Population-Level Analyses of Single-Molecule FRET Experiments. *Biophysical Journal* 106, 6 (2014), 1327–1337. [Link](#). (Cit. on p. 64).
- [106] Meyer P, Prodromou C, et al. Structural and Functional Analysis of the Middle Segment of Hsp90: Implications for ATP Hydrolysis and Client Protein and Cochaperone Interactions. *Molecular Cell* 11, 3 (2003), 647–658. [Link](#). (Cit. on p. 6).
- [107] Meyer P, Prodromou C, et al. Structural basis for recruitment of the ATPase activator Aha1 to the Hsp90 chaperone machinery. *The EMBO Journal* 23, 3 (2004), 511–519. [Link](#). (Cit. on p. 86).
- [108] Michaelis J. personal communication. 2014 (cit. on p. 45).
- [109] Mickler M, Hessling M, Ratzke C, Buchner J, & Hugel T. The large conformational changes of Hsp90 are only weakly coupled to ATP hydrolysis. *Nat Struct Mol Biol* 16, 3 (2009), 281–286. [Link](#). (Cit. on pp. 37, 75, 79, 80).
- [110] Mollapour M, Tsutsumi S, et al. Threonine 22 phosphorylation attenuates Hsp90 interaction with co-chaperones and affects its chaperone activity. *Molecular Cell* (2011) (cit. on p. 6).
- [111] Morin JG, & Hastings JW. Energy transfer in a bioluminescent system. *Journal of Cellular Physiology* 77, 3 (1971), 313–318. [Link](#). (Cit. on p. 12).
- [112] Myung IJ. Tutorial on maximum likelihood estimation. *Journal of mathematical Psychology* 47, 1 (2003), 90–100 (cit. on p. 68).
- [113] Neher E. Nobel lecture. Ion channels for communication between and within cells. *The EMBO Journal* 11, 5 (1992), 1672–1679. [Link](#). (Cit. on p. 21).
- [114] Olsen TJ, Choi Y, et al. Electronic Measurements of Single-Molecule Processing by DNA Polymerase I (Klenow Fragment). *Journal of the American Chemical Society* 135, 21 (2013). PMID: 23631761, 7855–7860. [Link](#). (Cit. on p. 3).
- [115] Panaretou B, Siligardi G, et al. Activation of the ATPase Activity of Hsp90 by the Stress-Regulated Cochaperone Aha1. *Molecular Cell* 10, 6 (2002), 1307–1318. [Link](#). (Cit. on pp. 85, 86).
- [116] Pearl LH. Review: The HSP90 molecular chaperone—an enigmatic ATPase. *Biopolymers* 105, 8 (2016), 594–607. [Link](#). (Cit. on pp. 7, 80).
- [117] Pearl LH, & Prodromou C. Structure and mechanism of the Hsp90 molecular chaperone machinery. English. *Annual Review of Biochemistry* 75 (2006), 271–294 (cit. on p. 6).
- [118] Perillo EP, Liu YL, et al. Deep and high-resolution three-dimensional tracking of single particles using nonlinear and multiplexed illumination. *Nature Communications* 6 (2015), 7874. [Link](#). (Cit. on p. 15).
- [119] Phillips RC, George P, & Rutman RJ. Thermodynamic Data for the Hydrolysis of Adenosine Triphosphate as a Function of pH, Mg²⁺ Ion Concentration, and Ionic Strength. *Journal of Biological Chemistry* 244, 12 (1969), 3330–3342. [Link](#). (Cit. on p. 70).
- [120] Plotkin SS. Determination of Barrier Heights and Prefactors from Protein Folding Rate Data. *Biophysical Journal* 88, 6 (2005), 3762–3769. [Link](#). (Cit. on p. 79).
- [121] Popa I, Fernández JM, & Garcia-Manyes S. Direct Quantification of the Attempt Frequency Determining the Mechanical Unfolding of Ubiquitin Protein. *Journal of Biological Chemistry* 286, 36 (2011), 31072–31079. [Link](#). (Cit. on p. 79).
- [122] Prodromou C. The 'active life' of Hsp90 complexes. *Biochimica et Biophysica Acta (BBA) - Molecular Cell Research* 1823, 3 (2012). Heat Shock Protein 90 (Hsp90), 614–623. [Link](#). (Cit. on pp. 6, 81, 86).
- [123] Prodromou C. Mechanisms of Hsp90 regulation. *Biochemical Journal* 473, 16 (2016), 2439–2452. [Link](#). (Cit. on pp. 6, 7, 81, 82).
- [124] Prodromou C, Roe SM, et al. Identification and Structural Characterization of the ATP/ADP-Binding Site in the Hsp90 Molecular Chaperone. *Cell* 90, 1 (1997), 65–75. [Link](#). (Cit. on pp. 5, 80).
- [125] Qian H. From discrete protein kinetics to continuous Brownian dynamics: A new perspective. *Protein science* 11, 1 (2002), 1–5 (cit. on p. 106).

Bibliography

- [126] Rabiner LR. A tutorial on hidden Markov models and selected applications in speech recognition. *Proceedings of the IEEE* 77, 2 (1989), 257–286 (cit. on p. 22).
- [127] Rasnik I, McKinney SA, & Ha T. Nonblinking and long-lasting single-molecule fluorescence imaging. *Nat Meth* 3, 11 (2006), 891–893. [Link](#). (Cit. on p. 42).
- [128] Ratzke C. SINGLE MOLECULE SPECTROSCOPY ON HSP90. PhD thesis. TUM, 2013 (cit. on p. 37).
- [129] Ratzke C, Berkemeier F, & Hugel T. Heat shock protein 90's mechanochemical cycle is dominated by thermal fluctuations. *Proceedings of the National Academy of Sciences* 109, 1 (2012), 161–166. [Link](#). (Cit. on p. 106).
- [130] Renn A, Seelig J, & Sandoghdar V. Oxygen-dependent photochemistry of fluorescent dyes studied at the single molecule level. *Molecular Physics* 104, 3 (2006), 409–414. [Link](#). (Cit. on pp. 41, 111).
- [131] Retzlaff M, Hagn F, et al. Asymmetric Activation of the Hsp90 Dimer by Its Cochaperone Aha1. *Molecular cell* 37, 3 (2010), 344–354. [Link](#). (Cit. on p. 86).
- [132] Retzlaff M, Stahl M, et al. Hsp90 is regulated by a switch point in the C-terminal domain. *EMBO Reports* 10, 10 (2009), 1147–1153 (cit. on pp. 6, 90).
- [133] Richter K, Reinstein J, & Buchner J. N-terminal Residues Regulate the Catalytic Efficiency of the Hsp90 ATPase Cycle. *Journal of Biological Chemistry* 277, 47 (2002), 44905–44910. [Link](#). (Cit. on p. 80).
- [134] Richter K, Soroka J, et al. Conserved Conformational Changes in the ATPase Cycle of Human Hsp90. *Journal of Biological Chemistry* 283, 26 (2008), 17757–17765. [Link](#). (Cit. on pp. 100, 103).
- [135] Rodina A, Vilenchik M, et al. Selective compounds define Hsp90 as a major inhibitor of apoptosis in small-cell lung cancer. *Nat Chem Biol* 3, 8 (2007), 498–507. [Link](#). (Cit. on p. 87).
- [136] Roe SM, Prodromou C, et al. Structural Basis for Inhibition of the Hsp90 Molecular Chaperone by the Antitumor Antibiotics Radicicol and Geldanamycin. *Journal of Medicinal Chemistry* 42, 2 (1999), 260–266. [Link](#). (Cit. on p. 87).
- [137] Roehl A, Rohrberg J, & Buchner J. The chaperone Hsp90: changing partners for demanding clients. *Trends in biochemical sciences* 38, 5 (2013), 253–262 (cit. on pp. 89, 100).
- [138] Roy R, Hohng S, & Ha T. A practical guide to single-molecule FRET. *Nat Meth* 5, 6 (2008), 507–516. [Link](#). (Cit. on pp. 15, 19).
- [139] Sabanayagam CR, Eid JS, & Meller A. Using fluorescence resonance energy transfer to measure distances along individual DNA molecules: Corrections due to nonideal transfer. *The Journal of Chemical Physics* 122, 6, 061103 (2005). [Link](#). (Cit. on pp. 34, 45).
- [140] Schulze A, Beliu G, et al. Cooperation of local motions in the Hsp90 molecular chaperone ATPase mechanism. *Nat Chem Biol* advance online publication (2016). [Link](#). (Cit. on pp. 6, 81, 86).
- [141] Schwarz G. Estimating the Dimension of a Model. *Ann. Statist.* 6, 2 (1978), 461–464. [Link](#). (Cit. on p. 65).
- [142] Shimomura O. Discovery of Green Fluorescent Protein, GFP. *Nobel Lecture* (2008) (cit. on p. 9).
- [143] Smith DA, Steffen W, Simmons RM, & Sleep J. Hidden-Markov Methods for the Analysis of Single-Molecule Actomyosin Displacement Data: The Variance-Hidden-Markov Method. *Biophysical Journal* 81, 5 (2001), 2795–2816. [Link](#). (Cit. on p. 21).
- [144] Sorgenfrei S, Chiu Cy, et al. Label-free single-molecule detection of DNA-hybridization kinetics with a carbon nanotube field-effect transistor. *Nat Nano* 6, 2 (2011), 126–132. [Link](#). (Cit. on p. 106).
- [145] Stigler J, & Rief M. Hidden Markov Analysis of Trajectories in Single-Molecule Experiments and the Effects of Missed Events. *ChemPhysChem* 13, 4 (2012), 1079–1086. [Link](#). (Cit. on p. 64).
- [146] Suzuki T, Tanaka K, Wakabayashi C, Saita Ei, & Yoshida M. Chemomechanical coupling of human mitochondrial F1-ATPase motor. *Nat Chem Biol* 10, 11 (2014), 930–936. [Link](#). (Cit. on p. 70).
- [147] Swindells JF, Snyder CF, Hardy RC, & Golden PE. *Viscosities of sucrose solutions at various temperatures: tables of recalculated values*. Circular 440. U.S. G.P.O.: Washington, DC: National Bureau of Standards, 1958, 4 (cit. on p. 96).
- [148] Taipale M, Jarosz DF, & Lindquist S. HSP90 at the hub of protein homeostasis: emerging mechanistic insights. *Nat Rev Mol Cell Biol* 11, 7 (2010), 515–528. [Link](#). (Cit. on pp. 3, 5).
- [149] Taipale M, Krykbaeva I, et al. Quantitative Analysis of Hsp90-Client Interactions Reveals Principles of Substrate Recognition. *Cell* 150, 5 (2012), 987–1001. [Link](#). (Cit. on p. 100).
- [150] Tamura JK, & Gellert M. Characterization of the ATP binding site on Escherichia coli DNA gyrase. Affinity labeling of Lys-103 and Lys-110 of the B subunit by pyridoxal 5'-diphospho-5'-adenosine. *Journal of Biological Chemistry* 265, 34 (1990), 21342–9. [Link](#). (Cit. on p. 123).
- [151] Tdunning. *Hidden Markov Model with Output*. 2012. url: <https://commons.wikimedia.org/wiki/File:HiddenMarkovModel.svg> (Last accessed: 11/14/2016) (cit. on p. 21).

- [152] Toba S, Watanabe TM, Yamaguchi-Okimoto L, Toyoshima YY, & Higuchi H. Overlapping hand-over-hand mechanism of single molecular motility of cytoplasmic dynein. *Proceedings of the National Academy of Sciences* 103, 15 (2006), 5741–5745. [Link](#). (Cit. on p. 3).
- [153] Tyagi S, & Lemke EA. Chapter 9 - Genetically Encoded Click Chemistry for Single-Molecule FRET of Proteins. *Laboratory Methods in Cell Biology/Imaging*. Ed. by Conn PM. Vol. 113. *Methods in Cell Biology*. Academic Press, 2013, 169–187. [Link](#). (Cit. on p. 35).
- [154] Verba KA, Wang RYR, et al. Atomic structure of Hsp90-Cdc37-Cdk4 reveals that Hsp90 traps and stabilizes an unfolded kinase. *Science* 352, 6293 (2016), 1542–1547. [Link](#). (Cit. on p. 6).
- [155] Visnapuu ML, & Greene EC. Single-molecule imaging of DNA curtains reveals intrinsic energy landscapes for nucleosome deposition. *Nat Struct Mol Biol* 16, 10 (2009), 1056–1062. [Link](#). (Cit. on p. 15).
- [156] Vogelsang J, Kasper R, et al. A Reducing and Oxidizing System Minimizes Photobleaching and Blinking of Fluorescent Dyes. *Angewandte Chemie International Edition* 47, 29 (2008), 5465–5469. [Link](#). (Cit. on p. 42).
- [157] Voss NR, & Gerstein M. 3V: cavity, channel and cleft volume calculator and extractor. *Nucleic Acids Research* (2010). [Link](#). (Cit. on p. 99).
- [158] Wang J, Xu L, Xue K, & Wang E. Exploring the origin of power law distribution in single-molecule conformation dynamics: Energy landscape perspectives. *Chemical Physics Letters* 463, 4–6 (2008), 405–409. [Link](#). (Cit. on p. 106).
- [159] Wang K, Sachdeva A, et al. Optimized orthogonal translation of unnatural amino acids enables spontaneous protein double-labelling and FRET. *Nat Chem* 6, 5 (2014), 393–403. [Link](#). (Cit. on p. 35).
- [160] Wang Q, & Moerner WE. Single-molecule motions enable direct visualization of biomolecular interactions in solution. *Nat Meth* 11, 5 (2014), 555–558. [Link](#). (Cit. on p. 15).
- [161] Wayne N, & Bolon DN. Dimerization of Hsp90 Is Required for in Vivo Function. *Journal of Biological Chemistry* 282, 48 (2007), 35386–35395. [Link](#). (Cit. on p. 37).
- [162] Wen JD, Lancaster L, et al. Following translation by single ribosomes one codon at a time. *Nature* 452, 7187 (2008), 598–603. [Link](#). (Cit. on p. 3).
- [163] Winner B, Jappelli R, et al. In vivo demonstration that α -synuclein oligomers are toxic. *Proceedings of the National Academy of Sciences* 108, 10 (2011), 4194–4199. [Link](#). (Cit. on p. 127).
- [164] Xie SX. Single-molecule approach to dispersed kinetics and dynamic disorder: Probing conformational fluctuation and enzymatic dynamics. *The Journal of Chemical Physics* 117, 24 (2002), 11024–11032. [Link](#). (Cit. on pp. 65, 106).
- [165] Yildiz A, Tomishige M, Vale RD, & Selvin PR. Kinesin Walks Hand-Over-Hand. *Science* 303, 5658 (2004), 676–678. [Link](#). (Cit. on p. 3).
- [166] Yun BG, Huang W, Leach N, Hartson SD, & Matts RL. Novobiocin Induces a Distinct Conformation of Hsp90 and Alters Hsp90-Cochaperone-Client Interactions. *Biochemistry* 43, 25 (2004). PMID: 15209518, 8217–8229. [Link](#). (Cit. on p. 89).
- [167] Zhao Q, Young IT, & Jong JGS de. Photon budget analysis for fluorescence lifetime imaging microscopy. *Journal of Biomedical Optics* 16, 8 (2011), [Link](#). (Cit. on pp. 41, 111).
- [168] Zierer BK, Rubbelke M, et al. Importance of cycle timing for the function of the molecular chaperone Hsp90. *Nat Struct Mol Biol* 23, 11 (2016), 1020–1028. [Link](#). (Cit. on pp. 7, 80).

LIST OF FIGURES

2.1	The structure of Hsp90.	5
3.1	The jellyfish <i>Aequorea victoria</i> and its fluorescent ring.	9
3.2	Jablonski diagram.	10
3.3	The Franck-Condon principle.	11
3.4	The dependences of FRET.	12
4.1	The 2 primary strategies to resolve single fluorophores.	15
4.2	TIR of a sea turtle at the sea/air interface.	16
4.3	Refraction at a glass/buffer interface.	16
4.4	The Heaviside step potential.	17
4.5	Two construction schemes for TIR microscopy.	19
5.1	The relation between observed signals, hidden states and HMM parameters.	21
5.2	The algorithm architecture frequently used in HMM analysis.	23
6.1	Design of the TIRF microscope.	27
6.2	Correct lens positioning for off-center rays.	28
6.3	The flow chamber and a zoom view of an immobilized biomolecule.	29
6.4	Auto-fluorescence background of glass and silica coverslips.	30
6.5	The beam shift by silica coverslips.	30
6.6	From raw data to results.	31
6.7	SE plots of stepwise smFRET correction.	33
7.1	Hsp90 construct for smTIRF measurements.	35
7.2	Hsp90 with highlighted lysins.	36
8.1	The triangle of fundamental limits.	41
8.2	The fundamental relation of observation time and SNR.	42
8.3	Representative time traces of dsDNA samples.	43
8.4	FRET E and distance distribution of dsDNA samples.	44
8.5	Distributions of local γ -values.	46
8.6	Results of a world-wide blind study on smFRET derived distances.	47
8.7	FRET efficiencies derived by intensity-based smFRET.	48
8.8	Total distance uncertainty of smFRET for Atto550/Atto647N.	49
8.9	Universal distance uncertainty of smFRET.	50
8.10	Kinetic smFRET data of a Holliday junction.	52
8.11	Accuracy of dwell-time analysis tested by simulations.	53
8.12	Conformational dynamics of Hsp90 resolved by smFRET.	54
8.13	Evaluating kinetic analysis of more realistic state models.	55
9.1	smFRET data as input for HMM.	60
9.2	The superior robustness of 2D HMM.	61
9.3	Illustration of semi-ensemble HMM.	62
9.4	The accuracy of semi-ensemble HMM.	63
9.5	Model selection using BIC.	65
9.6	Model refinement.	66
9.7	Three ways to evaluate the inferred model.	68
9.8	Quantifying energy coupling.	71
9.9	Flowchart summary of SMACKS.	74
10.1	Nucleotide dependent population of Hsp90's conformations.	75
10.2	Hsp90's conformational kinetics are best described by 4 states.	76
10.3	Minimal kinetic state models describing Hsp90.	77
10.4	Kinetic results of Hsp90 under varied nucleotide conditions.	77
10.5	Conformational transition rates deduced for Hps90.	78
10.6	Energy landscape of Hsp90's conformations.	79
10.7	Proposed connection between ATPase function and conformational dynamics of Hsp90.	81
11.1	Effects of Aha1 on the conformational dynamics of Hsp90.	85
11.2	Hsp90's transition rates in the presence of Aha1.	86
11.3	Hsp90's conformational equilibrium is not significantly affected by inhibitors.	87
11.4	Dwell time distributions measured at 2 sampling rates.	88
11.5	Conformational kinetics is weakly affected by inhibitors.	88
11.6	The localization of residue 577A in yeast Hsp90.	90
11.7	C-terminal point mutations modulate Hsp90's conformational steady-state.	91
11.8	The influence of C-terminal point mutations on Hsp90's conformational kinetics.	91
12.1	The crowded cellular environment.	95
12.2	The excluded-volume effect.	96
12.3	Setup of crowding experiments.	96
12.4	The effect of viscosity and macromolecular crowding on Hsp90's conformations.	97
12.5	Viscosity suppresses fast dynamics.	97

12.6	The resolved kinetics of Hsp90 are only weakly affected by viscosity and crowding.	98
12.7	The effect of sucrose and Ficoll 400 on Hsp90's ATPase activity.	98
12.8	The crowder view on Hsp90.	99
12.9	Cation dependence of Hsp90's conformations.	101
12.10	Cation dependence of Hsp90's kinetics.	102
12.11	Hsp90's ATPase activity under varied cation conditions.	102
13.1	Hsp90's conformational kinetics measured at 4 sampling rates.	105
A.1	SNR of individual dsDNA-coupled dyes.	113
A.2	Distribution of the fluorescence of individual molecules.	113
A.3	Calibration curves of the laser power.	113
A.4	FRET E from fluorescence with (un-)correlated noise.	114
A.5	Distance vs. FRET E averaging under (un-)correlated noise.	114
A.6	The effect of biased fluorescence on FRET E.	115
A.7	BIC detects the size of the input model.	116
A.8	Correct minimal state models inferred by SMACKS.	117
A.9	Nucleotide dependence using varied dye positions.	118
A.10	Inhibition of Hsp90's ATPase activity by 4 inhibitors.	119
A.11	Ensemble FRET competition assay with inhibitors.	119
A.12	Post-hoc downsampling.	120
B.1	The gene sequence of the Hsp90 construct used herein.	122
C.1	Proof of principle of bleach step counting using DNA-origami.	128
C.2	α -synuclein oligomer size distributions.	129
C.3	The effect of α -synuclein on Hsp90's conformational dynamics.	130

LIST OF TABLES

8.1	smFRET results for 6 dsDNA samples.	45
8.2	FRET efficiency results of the world-wide comparison on intensity-based sm-FRET.	48
8.3	smFRET derived distances and standard deviations.	49
9.1	SMACKS accurately detects kinetic heterogeneity.	67
A.1	Comparison of simulated input and output by SMACKS in Table A.1 .	116
A.2	Comparison of simulated input and SMACKS output in Figure A.8 .	117
B.1	Components of the smTIRF setup and their manufacturers.	124